# Università degli Studi di Padova


Department of Physics and Astronomy "Galileo Galilei"


*Master Thesis in Physics*

# Gravitational waves search for generic transient of intermediate duration in future interferometes network using coherentWave Burst algorithm


*Supervisor*
Prof. Giacomo Ciani
Università degli Studi di Padova

*Co-supervisor*
Dr. Claudia Lazzaro
Università degli Studi di Padova

*Master Candidate*
Lorenzo Mobilia

*Student ID*
1211961


*Academic Year*
2021 - 2022

"Il tempo è ciò in cui si svolgono gli eventi"
— Aristotele

# Abstract

Searches for generic transient Gravitational Waves (GW) target the widest possible range of different astrophysical sources, using no or minimal assumption on the morphology of the signal; in particular different astrophysical phenomena are foreseen to emit GW signals with long duration (by few sec. to hundreds of sec.), among those: fallback, newborn neutron , accretion disk instabilities, non axisymmetric deformation in magnetars. Coherent Wave Burst (cWB) is the flagship algorithm, in the LIGO- Virgo collaboration, used for the generic transient analysis without assumption morphology or arrival direction of GW signal. This project contributes to improve and optimize cWB algorithm for long duration generic gravitational waves search in the LHV (LIGO-Virgo) interferometers network.

In particular the project aims to test possible algorithm configurations for next data taking of LHV (O4 is foreseen to start by the beginning of the next year), through a reanalysis and simulations campaign of public data of last data taking (O3b - November 2019 to March 2020). Specifically the project reanalyses the O3b data giving attention to the efficiency of the algorithm in reconstructing the signals. The first purpose of the project was developing codes and analysis to characterize the parameters of the signals like frequency, length etc. Also the capability of the algorithm in reassembling correctly the injected signal, considering the number of segments in which is divided the trigger obtained by the pipeline have been held specially into account, since this parameter qualifies the effectiveness of the algorithm in regaining the signal through clustering process. Statistical studies of this characteristic have been taken into attention, studying the segmentation process among different morphologies of gravitiational waves signal expected for astrophysical processes. The waveforms have been chosen in order to cover a wide spectrum of morphologies, duration and frequency.

Furthermore, the network with expected sensitivity for post-O4 data taking has been studied, considering a scaled strain sensitivity curve of the detectors obtained from the O3b data, and performing injection of the same Gravitational Wave signals used in O3b analysis. In particular efficiency and background analysis have been taken into account, especially in LHV network configuration due to the additional noisy behavior of the Virgo interferometer. Two different configurations of the algorithm have been studied in order to classify properly the case of non coaligned three interferometer detector networks, as LHV.

Finally in this project the test of the machine learning algorithm already introduced in other cWB searches will be performed for the long search. This algorithm is supposed to help us in noise-signal discharge analysis, distinguishing the Gravitational Waves signals from the noise background and it has already been used for other research. In particular different astrophysical phenomena are foreseen to emit GW signals with long duration (by few sec. to hundreds of sec.)

The Gravitational Waves are the outstanding prediction of the General Relativity (Chapter 1). In order to detect those signal, the need of Earth interferometers have been necessary, their characteristics will be discussed in this work (Chapter 2). Then the developing of a pipeline to test the response of the detectors and the capability in detecting the Gravitational Waves signals have been developed, this tool is coherent WaveBurst (cWB) and it will be described in its features (Chapter 3). With the use of this powerful tool detection efficiency and performances of the IFOs network will be reported (Chapter 4); considering various data acquisition campaign as O3b and simulated O4 with varying parameters. Finally there will be tested the capability of a Machine Learning algorithm in reconstructing signals, using some test waveform models in which the algorithm have been trained and some others not (Chapter 5). Conclusions and possible other works will be exposed at the end of the project (Chapter 6).

# Contents

# Listing of figures

# Listing of tables

# 1

# Gravitational Waves As Solution of the Linearized Einstein Equations and Physical Effects

## 1.1 Preamble

One of the most overwhelming discoveries of the last century was the space-time concept. Developed by Einstein in the early years of 1900, special relativity solved the problem of the light travelling in the vacuum at speed c after the Michaelson and Morley experiment. From this starting point, the concepts of special relativity theory led huge amount of knowledge to the mankind. From the famous equation $E = mc^2$ to the most deep concepts of electrodynamics. Then using the mathematical framework given by Levi-Civita and developing the correct structure to describe the curved space-time, the General Relativity (GR) was born. And this is the first problem we will deal with: the Gravitational Waves equation from Einstein's equations.

## 1.2 The Einstein's Equation

Not just one book would be enough in order to obtain the point we are starting from: the Einstein's Equation, so we just introduce them, and then explain what they stand for [2], [17].

$$R_{\mu\nu} - \frac{1}{2} g_{\mu\nu} R = \frac{8\pi G}{c^4} T_{\mu\nu} \tag{1.1}$$

As mentioned above, the proof in order to obtain these equations exiles from this thesis, but it's primary toward obtaining the Gravitational Waves equation. These equations relate the space-time curvature to the source of that curvature, which can be equivalently energy or mass, as we learn from special relativity. So the elements inside these equations are the Ricci Tensor $R_{\mu\nu}$ which describes the curvature of the space time, the metric tensor $g_{\mu\nu}$, which as the name suggest is related to the metric of the space time and the Ricci scalar R, which is obtained from the contraction of $R_{\mu\nu}$ and $g_{\mu\nu}$. On the other side of the equal, apart from the well known constant as G (the universal Gravitation constant) and c (the speed of light), $T_{\mu\nu}$ represents the stress-energy tensor, that describes the source of the curvature of the space-time as the flux and density of energy through the space-time [17]. In order to obtain the Gravitational Waves Equation from Einstein's Equation, we will use a framework known as Linearized Theory, which will allow us to obtain the Linearized Einstein equations.

## 1.3 Linearizing the Einstein equations

The GR theory asserts that does exist a frame where equation as (1.2) hold [2]: what we do is applying is a perturbation theory on a flat background represented by $g_{\mu\nu}$:

$$g_{\mu\nu} = \eta_{\mu\nu} + h_{\mu\nu} \tag{1.2}$$

$h_{\mu\nu}$ satisfy $|h_{\mu\nu}| \ll 1$. This means that we are considering $h_{\mu\nu}$ such as a perturbative term which tells us the order of expansion of the perturbation. A basic tool needed in the GR framework is the concept of Gauge. Gauge invariance means that a theory is invariant under a transformation of coordinates [17]. So the next question is, what are the allowed gauges by this approximation? Basically we are dealing with two gauges: the Lorenz gauge and the infinitesimal gauge.

Let's start defining the tensor $\Lambda^{\mu}_{\rho}$ such as

$$\Lambda^{\mu}_{\rho} = \frac{dx^{\mu}}{dx'^{\rho}} \tag{1.3}$$

Where the apex $'$ identifies the new coordinates set. So the metric tensor in the new coordinates can be written as

$$g'_{\mu\nu} = \Lambda^{\rho}_{\mu}\Lambda^{\sigma}_{\nu}g_{\rho\sigma} \tag{1.4}$$

Clearly we use Einstein's notation for the sum. So using (1.2) in (1.4) we get

$$g'_{\mu\nu} = \Lambda^{\rho}_{\mu}\Lambda^{\sigma}_{\nu}(\eta_{\rho\sigma} + h_{\rho\sigma}) = \Lambda^{\rho}_{\mu}\Lambda^{\sigma}_{\nu}\eta_{\rho\sigma} + \Lambda^{\rho}_{\mu}\Lambda^{\sigma}_{\nu}h_{\rho\sigma} \tag{1.5}$$

So we easily obtain

$$h'_{\mu\nu} = \Lambda^{\rho}_{\mu}\Lambda^{\sigma}_{\nu}h_{\rho\sigma} \tag{1.6}$$

Now we can introduce the infinitesimal transformation. This transformation starts from defining a parameter $\xi$ which satisfy the following condition

$$\partial_{\mu}\xi \sim o(h_{\mu\nu}) \tag{1.7}$$

So we can consider the following infinitesimal transformation

$$x^{\mu} \to x'^{\mu} = x^{\mu} + \xi^{\mu}(x) \tag{1.8}$$

It is easy to show that

$$g'_{\mu\nu}(x') = \frac{\partial x^{\rho}}{\partial x'^{\mu}}\frac{\partial x^{\sigma}}{x'^{\nu}}g_{\rho\sigma}(x) \simeq (\delta^{\rho}_{\mu} - \partial_{\mu}\xi^{\rho})(\delta^{\sigma}_{\nu} - \partial_{\nu}\xi^{\sigma})(\eta_{\rho\sigma} + h_{\rho\sigma}(x)) \simeq \tag{1.9}$$

$$\simeq \eta_{\mu\nu} + h_{\mu\nu}(x) - \partial_{\nu}\xi^{\sigma}\eta_{\mu\sigma} - \partial_{\mu}\xi^{\rho}\eta_{\rho\nu} = \tag{1.10}$$

$$= \eta_{\mu\nu} + h_{\mu\nu}(x) - \partial_{\nu}\xi_{\mu} - \partial_{\mu}\xi_{\nu} = \eta_{\mu\nu} + h'_{\mu\nu}(x') \tag{1.11}$$

So we finally get [2]

$$h'_{\mu\nu} = h_{\mu\nu} - \partial_{\nu}\xi_{\mu} - \partial_{\mu}\xi_{\nu} \tag{1.12}$$

Now we have all the tools we need to obtain the Linearized Einstein Equations. We can obtain the linearized Riemann tensor from the Christoffel's symbol expanded at the first order in h. The Christoffel's symbols are a mathematical object used in order to define the covariant derivative $\nabla_{\mu}$, which allows us to perform a derivative in a curved space-time [17]. The

Christoffel's symbols are defined as

$$\Gamma^{\mu}_{\nu\rho} = \frac{1}{2} g^{\mu\delta}(\partial_\nu g_{\delta\rho} + \partial_\rho g_{\nu\delta} - \partial_\delta g_{\nu\rho}) \tag{1.13}$$

Performing the expansion in h we get

$$\Gamma^{\sigma}_{\mu\nu} \simeq \frac{1}{2}(\partial_\mu h^{\sigma}_{\nu} + \partial_\nu h^{\sigma}_{\mu} - \partial^{\sigma} h_{\mu\nu}) \tag{1.14}$$

After some calculations we obtain the Riemann Tensor linearized

$$R^{\sigma}_{\mu\nu\rho} = \frac{1}{2}(\partial_\nu \partial_\mu h^{\sigma}_{\rho} + \partial_\rho \partial^{\sigma} h_{\mu\nu} - \partial_\nu \partial^{\sigma} h_{\mu\rho} - \partial_\rho \partial_\mu h^{\sigma}_{\nu}) \tag{1.15}$$

From this we get the Ricci tensor and Ricci scalar

$$R_{\mu\nu} = R^{\sigma}_{\mu\nu\sigma} \tag{1.16}$$

$$R = \eta^{\mu\nu} R_{\mu\nu} = \Box h - \partial_\nu \partial_\sigma h^{\sigma\nu} \tag{1.17}$$

At the end we obtain the Linearized Einstein equations, which look formally as the unlinearized, but we have to take into account the expression (2.16) and (2.17). The $\Box$ is the d'Alembertian operator $\Box = \left(\frac{1}{c^2}\frac{\partial^2}{\partial x_0^2} - \Delta\right)$

$$R_{\mu\nu} - \frac{1}{2} g_{\mu\nu} R = \frac{8\pi G}{c^4} T_{\mu\nu} \tag{1.18}$$

The next step is to find a useful representation that will help us to visualize the Linearized Einstein Equations as a wave-like equation, so we introduce the Transverse Gauge representation.

## 1.4 Transverse Traceless Gauge and Wave Equation

It is useful to define

$$\bar{h}_{\mu\nu} = h_{\mu\nu} - \frac{1}{2}\eta_{\mu\nu} \tag{1.19}$$

So using this we can write

$$\Box \bar{h}_{\mu\nu} + \eta_{\mu\nu}\partial_\rho \partial_\sigma \bar{h}^{\rho\sigma} - \partial_\nu \partial_\rho \bar{h}^{\rho}_{\mu} - \partial_\mu \partial_\rho \bar{h}^{\rho}_{\nu} = -\frac{16\pi G}{c^4} T_{\mu\nu} \tag{1.20}$$

At this point we can use the infinitesimal transformation for h (1.12), and it's easy to show that

$$\bar{h}^{\prime\mu\rho} = \bar{h}^{\mu\rho} - \partial^{\mu}\xi^{\rho} - \partial^{\rho}\xi^{\mu} + \eta^{\mu\rho}\partial_{\sigma}\xi^{\sigma} \tag{1.21}$$

Now applying the $\partial_{\rho}$ operator we end up with

$$\partial_{\rho}\bar{h}^{\prime\mu\rho} = \partial_{\rho}\bar{h}^{\mu\rho} - \Box\xi^{\mu} \tag{1.22}$$

Now we have to use a smart gauge choice, the best one is the one for which it holds: $\partial_{\rho}\bar{h}^{\prime}_{\mu\nu} = 0$, so

$$\Box\xi_{\mu} = \partial_{\rho}\bar{h}_{\mu\nu} \tag{1.23}$$

So the linearized Einstein's Equations are

$$\Box\bar{h}_{\mu\nu} = -\frac{16\pi G}{c^4}T_{\mu\nu} \tag{1.24}$$

This equation is the wave equation. Firstly we see that $h_{\mu\nu}$ is not explicitly a tensorial field related to the geometry of space-time, instead it is a generic field. Moreover equation (1.24) obeys the superposition principle. Let us start supposing that the source $T_{\mu\nu}$ is far away, so it is reasonable to impose $T_{\mu\nu} = 0$. We recall that $T_{\mu\nu}$ is the stress energy tensor, we have seen it in Einstein's Equation (1.1). This is relevant since in the Einstein's Equation this term relates the curvature of space-time and the mass, or energy, of an object. In this context instead this relates the perturbation of a flat metric with a mass-energy term. So it follows

$$\Box\bar{h}_{\mu\nu} = 0 \tag{1.25}$$

This means that the solution can be wave-type, like

$$\bar{h}_{\mu\nu} = A_{\mu\nu}e^{ik_{\lambda}\omega^{\lambda}} \tag{1.26}$$

Where $A_{\mu\nu}$ is a 4x4 matrix. We can write immediately that

$$\Box\bar{h}_{\mu\nu} = 0 \rightarrow k_{\lambda}k^{\lambda} = 0, k_{\mu} \in \mathbb{R} \tag{1.27}$$

$$\partial_{\rho}\bar{h}_{\mu\nu} = 0 \rightarrow A_{\mu\nu}k^{\mu} = 0, A_{\mu\nu} \in \mathbb{C}, A_{\mu\nu} = A_{\nu\mu} \tag{1.28}$$

Let's now move to the TT Gauge. This Gauge can be obtained considering a further transformation on the Lorenz Gauge,

starting from $x^\mu \to x'^\mu = x^\mu + \xi^\mu$, and considering $\Box\xi^\mu = 0$ this drag us to the Transverse Traceless Gauge. In fact, such expression of the GW have been obtained considering $\partial_\rho \bar{h}_{\mu\nu} = 0$, which means that $\partial_\rho h_{\mu\nu} = \Box\xi_\mu$. This result is equivalent to ask that $\Box\xi_\mu = 0$. So we can impose four conditions to $h_{\mu\nu}$ using the $\xi$. We can write $\bar{h}^{TT}_{\mu\nu}$ in a simple way, using both Lorenz Gauge and the $A_{\mu\nu}$ relations.

$$\bar{h}^{TT}_{\mu\nu} = \begin{pmatrix} 0 & 0 & 0 & 0 \\ 0 & h_+ & h_x & 0 \\ 0 & h_x & -h_+ & 0 \\ 0 & 0 & 0 & 0 \end{pmatrix} e^{ik_\mu k^\mu} \tag{1.29}$$

So $\bar{h}^{TT}_{\mu\nu}$ has just two degrees of freedom that corresponds to the polarization of the gravitational wave [17]. If we now consider a ring of test masses, the passage of the Gravitational Wave through this ring will produce an effect similar to the one represented in image (1.1).

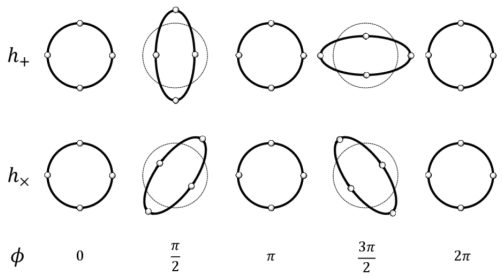


**Figure 1.1:** The effect of the passage of the linearly polarised gravitational wave through the ring of particles in the direction orthogonal to the plane is depicted in this figure. The circle shrinks in one direction and expands in the orthogonal direction during the crest and vice versa during the trough. This effect occurs along the directions oriented 45° with respect to one another for plus and cross polarizations denoted by $h_+$ and $h_x$, respectively. for reference [1]

## 1.5 Physical Effects of the Gravitational Waves

Since in the TT gauge the coordinates themselves are stretched, so there are no visible effects[2]. We need to consider the proper detector frame, or the free falling system. Basically we consider not the geodesic equation of a particle, instead the proper distance $ds^2$. We recall the proper distance is defined as $ds^2 = g_{\mu\nu}dx^\mu dx^\nu$. It is easy tho show that in the free falling frame, given the position $x_1$ and $x_2$ for two different particles, if a GW is flowing through $\hat{z}$ axis there is

$$ds^2 \simeq (x_2 - x_1)\left(1 + \frac{1}{2}h_+ \cos(\omega t)\right) \tag{1.30}$$

So we can see the oscillatory effect of a gravitational wave through the proper distance. This means that the oscillatory phenomena of the Gravitational Waves on the Earth are observable through a Rigid Ruler. What we see is an expansion of the metric $g_{\mu\nu}$ in $O\left(\frac{r^2}{L_B^2}\right)$, where r is the distance between the test masses and $L_B$ is the variation of the Gravitational Field due to the Gravitational Waves, or more formally the scale variation of the Riemann Tensor $R_{0ijk}$. So expanding $g_{\mu\nu}$ at this order means basically

$$g_{\mu\nu}(x) \simeq g_{\mu\nu}(0) + [\partial_i g_{\mu\nu}(x)]_{x=0} x^i + \frac{1}{2}[\partial_i \partial_j g_{\mu\nu}(x)]_{x=0} x^i x^j \tag{1.31}$$

We said that the correction are of the order $O\left(\frac{r^2}{L_B^2}\right)$, which are related to equation (1.33) in the following way, $r^2 = x^2 x^j$ is the distance from the origin, while $L_B$ is the typical spatial scale of the variations of the metric $R_{0ijk} = \left(\frac{1}{L_B^2}\right)$. So we get for $ds^2$

$$ds^2 \simeq -c^2 dt^2 (1 + R_{0i0j} x^i x^j) - 2cdt dx^i \left(\frac{2}{3} R_{0ijk} x^j x^k\right) + dx^i dx^j \left(\delta_{ij} - \frac{1}{3} R_{ikjl} x^k x^l\right) \tag{1.32}$$

If we consider now just the spatial element of the geodesic deviation [2] we get that

$$0 = \frac{d^2 \xi^i}{d\tau} + 2\Gamma^i_{\nu\rho} \frac{dx^\nu}{d\tau} \frac{d\xi^\rho}{d\tau} + \xi^\sigma (\partial_\sigma \Gamma^i_{\nu\rho}) \frac{dx^\nu}{d\tau} \frac{dx^\rho}{d\tau} \tag{1.33}$$

Performing some maths and remembering that only the double derivatives with respect to spatial index are nonzero we get that

$$0 = \frac{d^2 \xi^i}{d\tau^2} + R^i_{0j0} \xi^j \left(\frac{dx^0}{d\tau}\right) = \ddot{\xi}^i + c^2 R^i_{0j0} \xi^j \tag{1.34}$$

The Riemann tensor is invariant with respect to the gauge, so in the TT gauge is

$$R^i_{0j0} = R_{i0j0} = -\frac{1}{2c^2} \ddot{h}^{TT}_{ij} \tag{1.35}$$

So it is easy to show that the geodesic deviation in the proper detector frame ends up in the following expression

$$\ddot{\xi}^i = \frac{1}{2} \ddot{h}^{TT}_{ij} \xi^j \tag{1.36}$$

Where $\xi$ is the distance between two test masses. This equation is noticeable because resemble us the equation of a particle accelerated under a Newtonian force [2] such as

$$F_i = \frac{m}{2} \ddot{h}^{TT}_{ij} \xi^j \tag{1.37}$$

## 1.6 Source of a Gravitational Wave

In order to deal with this problem, some assumptions must have to be considered. Firstly we approached the Gravitational Wave Equation starting from a flat space-time (linearized theory), so the gravitational field generated by the source is sufficiently weak to justify a perturbation around a flat space-time. For systems held together just by gravitational force this implies also that the typical velocity inside the source is small [2]. Since we are in these conditions, we can consider small velocities $v << c$, which means non relativistic systems. Also we do assume the conservation of energy-momentum $\partial^{\mu}T_{\mu} = 0$. In order to solve equation (1.24) we need to use the Green function [17]. We highlight the use of the tensor $\Lambda$ which is useful to project the result in the TT gauge. Let's start defining the Projector $P_{ij}(\hat{n})$ as

$$P_{ij}(\hat{n}) = \delta_{ij} - n_i n_j \tag{1.38}$$

From this we can define the $\Lambda$ tensor

$$\Lambda_{ij,kl}(\hat{n}) = P_{ik}P_{jl} - \frac{1}{2}P_{ij}Pkl \tag{1.39}$$

Which is also a transverse projector. So we need to apply the Green Function method at the following equation:

$$\Box\bar{h}_{\mu\nu} = -\frac{16\pi G}{c^4}T_{\mu\nu} \tag{1.40}$$

The Green Function for the x axis must satisfy

$$\Box_x G(\vec{x} - \vec{y}) = \delta^4(\vec{x} - \vec{y}) \tag{1.41}$$

Where $\vec{x}$ is the free variable while $\vec{y}$ is the coordinate of the source. So we must find a solution for

$$-2K\int d^4y\Box_x G(\vec{x} - \vec{y})T_{\mu\nu}(\vec{y}) = -2K\int d^4y\delta^4(\vec{x} - \vec{y})T_{\mu\nu}(\vec{y}) \tag{1.42}$$

Solving this integral we find out the Green Function, so performing some calculus we get (for the complete procedure see [2])

$$G(x^{\sigma}) = f(r)\delta(ct - r)\theta_H(ct) \tag{1.43}$$

where the $\sigma$ index identifies the 4-dimensions of the variable, while the $\theta_H(ct)$ function is needed for the causality. Per-

forming some calculus we get

$$\bar{h}_{\mu\nu}(t,\vec{x}) = \frac{4G}{c^4}\int d^3\vec{y}\frac{T_{\mu\nu}(ct-|\vec{x}-\vec{y}|,\vec{y})}{|\vec{x}-\vec{y}}} \tag{1.44}$$

Now just applying the $\Lambda$ tensor

$$h_{ij}^{TT}(ct,\vec{x}) = \frac{4G}{c^4}\Lambda_{ij,kl}(\hat{n})\int d^3\vec{y}\frac{T_{\mu\nu}(ct-|\vec{x}-\vec{y}|,\vec{y})}{|\vec{x}-\vec{y}|} \tag{1.45}$$

At this point using the far field regime we can perform the first expansion: we assume that the source is far from the detector, so defining as r the distance from the source and assuming that r is much bigger than the spatial extension d of the source we get

$$|\vec{x}-\vec{y}| \sim r\Big(1-\frac{\vec{y}\cdot\hat{n}}{r}+o\Big(\frac{d^2}{r^2}\Big)\Big) \tag{1.46}$$

So stopping at the first order in $|\vec{x}-\vec{y}|$ we find

$$h_{ij}^{TT}(ct,\vec{x}) \simeq \frac{1}{r}\frac{4G}{c^4}\Lambda_{ij,kl}\int d^3\vec{y}T_{kl}(t-\frac{r}{c}+\frac{\vec{y}\cdot\hat{n}}{c},\vec{y}) \tag{1.47}$$

Now it is time for the multipole expansion, assuming that the source is emitting at $\omega_s$ frequency, we can say that in the non relativistic limit the following relations hold, that the energy-momentum tensor can be written as

$$T_{kl} \sim \frac{1}{\omega_s} \sim \frac{1}{v} \tag{1.48}$$

And this term can be considered as

$$\frac{d}{c} << \frac{d}{v} \rightarrow \xi = \frac{\vec{y^i}\cdot n^i}{c} \sim \frac{d}{c} \tag{1.49}$$

So $\xi$ can be the parameter used for the expansion

$$T_{kl}\Big(t-\frac{r}{c}+\frac{\vec{y}\hat{n}}{c},\vec{y}\Big) = T_{kl}\Big(t-\frac{r}{c}+\xi,\vec{y}\Big) = \Big[T_{kl}\Big]_{\xi=0} + \Big[\frac{\partial T_{kl}}{\partial\xi}\Big]_{\xi=0}\xi + \dots \tag{1.50}$$

We can stop at the first order and write

$$h_{ij}^{TT}(t,\vec{x}) \sim \frac{1}{r}\frac{4G}{c^4}\Lambda_{ij,kl}\Big(S^{kl}+\frac{1}{c}\dot{S}^{kl,m}\Big)_{\text{retarded}} \tag{1.51}$$

Where $S^{ij,[klm\dots]}(t) = \int d^3x T^{ij}(t,x)[x^k x^l x^m \dots]$. So we can now define the energy density momenta M

$$M = \frac{1}{c^2}\int d^3x T^{00}(t,x) \tag{1.52}$$

$$M^i = \frac{1}{c^2}\int d^3x T^{00}(t,x)x^i \tag{1.53}$$

$$\vdots \tag{1.54}$$

And the linear-momentum density momenta P

$$P^i = \frac{1}{c^2}\int d^3x T^{0i}(t,x) \tag{1.55}$$

$$P^{i,j} = \frac{1}{c^2}\int d^3x T^{0,i}(t,x)x^j \tag{1.56}$$

$$\vdots \tag{1.57}$$

Now using expressions that relate the M and P terms such as $\ddot{M}^{ij} = \dot{P}^{ij} + \dot{P}^{ji} = S^{ij} + S^{ji} = 2S^{ij}$ we can write for the h the following equation

$$h_{ij}^{TT}(t,\vec{x}) \simeq \frac{1}{r}\frac{2G}{c^4}\Lambda_{ij,kl}\ddot{M}^{kl} \tag{1.58}$$

Where $\ddot{M}$ is the second derivative of M with respect to time. The most important element of the above equation is the dependance of h from the distance of the source r. It is convenient to write this equation in terms of quadrupole moments. Defining

$$Q^{kl} = \left(M^{kl}\frac{1}{3}\delta^{kl}M_{ii}\right) = \int d^3x \rho(t,x)(x^i x^j - \frac{1}{3}r^2\delta^{ij}) \tag{1.59}$$

We obtain, since M and Q are interchangeable

$$h_{ij}^{TT}(t,\vec{x}) = \frac{1}{r}\frac{2G}{c^4}\ddot{Q}^{T}T_{ij}\left(t - \frac{r}{c}\right) \tag{1.60}$$

We highlight that it is important how big is Q and how fast it changes in time. Considering the usual $\hat{z}$ axis for the propagation, we have

$$\hat{n} = (0, 0, 1)$$

$$P_{ij} = \text{diag}(1, 1, 0)$$

Performing the calculations we obtain for the polarization the following expressions

$$h_+ = \frac{1}{r}\frac{G}{c^4}(\ddot{M}_{11} - \ddot{M}_{22}) \tag{1.61}$$

$$h_x = \frac{2}{r}\frac{G}{c^4}\ddot{M}_{12} \tag{1.62}$$

We highlight that in order to have Gravitational Wave a second order time derivative for the quadrupole moment it is required, so this can be seen as an asymmetry on a gravitating system (like a mountain in a neutron star), or by a binary system.

## 1.7 Energy of a Gravitational Wave

One of the most problematic points about the Gravitational Wave equation obtained within a perturbative method, which means in a linearized framework, is that they cannot transport energy by construction [2]. This happens because in the expansion we stopped at the first order in h, while the energetic terms came up at the second order. More explicitly we considered the Gravitational Waves as perturbation of a flat space time, instead we should focus our problem in a different way. In order to assert that Gravitational Waves can curve the space-time we must consider it as curved, so the metric tensor $g_{\mu\nu}$ must be expressed in the following way

$$g_{\mu\nu} = \bar{g}_{\mu\nu} + h_{\mu\nu} \tag{1.63}$$

Where we are considering both terms: background term $\bar{g}_{\mu\nu}$, which identifies the unperturbed curved space-time, and perturbation term $h_{\mu\nu}$. In this way we are considering the gravitational waves as perturbation on a curved space-time, in fact we talk about tidal effects. So the point now is to distinguish $\bar{g}_{\mu\nu}$ from $h_{\mu\nu}$. This can be viewed in frequency terms. We can associate to the background the frequency $f_B$ and to the perturbation term the frequency f, corresponding to a wavelength for the background $L_B$ and $\alpha$ for the gravitational wave. In order to achieve this point we need to use the short-wave approximation. Basically we cannot divide these two components one from the other, but we can consider their effect on the metric quite different. In other terms $h_{\mu\nu}$ acts in space and frequencies distinct from the background. So if we think that

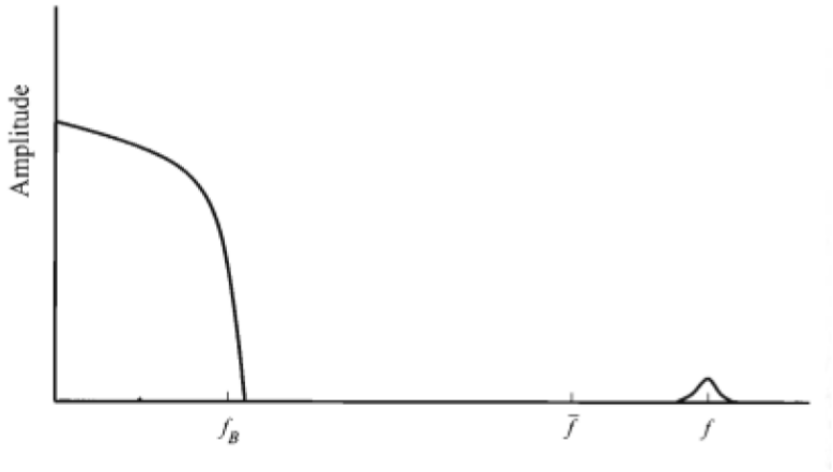


**Figure 1.2:** A situation that allow us to separate the metric into low-frequency background and and small high-frequency perturbation. The background is defined as the part with frequencies $f_B << \bar{f}$ and the GW as the part with $f >> \bar{f}$. For reference [2]

$$h \sim e^{ikx} \rightarrow \frac{d}{dx}e^{ikx} = ke^{ikx} \sim \frac{2\pi}{\lambda}e^{ikx}$$

Also it is true that

$$\bar{g}_{\mu\nu} \sim \left(L_B\right)$$

So defining

$$\alpha = \frac{\lambda}{2\pi}$$

Then the effect is distinguishable if

$$\alpha << L_B \tag{1.64}$$

Or equivalently we ask that the $L_B$ is slow in time with respect to the $\alpha$. So what we do is to perform an expansion on $R_{\mu\nu}$. We get then

$$R_{\mu\nu} = \bar{R}_{\mu\nu} + R^{(1)}_{\mu\nu} + R^{(2)}_{\mu\nu} = \left(\frac{1}{2}g_{\mu\nu}T + T_{\mu\nu}\right) \tag{1.65}$$

Where $\bar{R}_{\mu\nu}$ is related to the background, $R^{(1)}_{\mu\nu}$ is the first order in h (high frequencies), while $R^{(2)}_{\mu\nu}$ is the second order in h (both high and low frequencies)

So we can write the following equation in terms of high and low frequencies

$$\bar{R}_{\mu\nu} = \left[T_{\mu\nu} - \frac{1}{2}g_{\mu\nu}\right]^{\text{low}} - \left[\bar{R}^{(2)}_{\mu\nu}\right]^{\text{low}} \tag{1.66}$$

$$R^{(1)}_{\mu\nu} = \left[T_{\mu\nu} - \frac{1}{2}g_{\mu\nu}T\right]^{\text{high}} - \left[R^{(2)}_{\mu\nu}\right]^{\text{high}} \tag{1.67}$$

So we split the equation into high and low frequency components. Knowing now that the parameters of the expansion are $g_{\mu\nu}$ and h, we also know their behaviour, $o(g_{\mu\nu}) \sim \frac{1}{L_B}$ and $o(h_{\mu\nu}) \sim \frac{h}{\bar{\lambda}}$. This means that for the low frequency components equation (1.66) can be written as

$$\left(\frac{1}{L_B}\right)^2 \sim \left(\frac{h}{\bar{\lambda}}\right)^2 + o(T_{\mu\nu}) \tag{1.68}$$

So if $T_{\mu\nu} = 0$ then

$$\frac{1}{L_B} \sim \frac{h}{\bar{\lambda}} \rightarrow h \sim \frac{\lambda}{L_B} \tag{1.69}$$

We can now use a quite common procedure widespread in quantum field theory and statistical mechanics: the renormalization group transformation. The basic idea is starting from the fundamental equations of a theory and then "integrate out" the fluctuations that take places in a length scale smaller than l, in order to obtain an effective theory that describes the physics at length scale l [2], so we consider a length $\bar{l}$ such that

$$a << \bar{l} << L_B \tag{1.70}$$

Then we perform an average in this parameter. What happens is that

- The metric of the background is not affected by the average
- The high frequency phenomena are averaged away
- only the terms $\sim h^2$ remain which are related to the energy.

Defining with $\langle\rangle$ the average performed over $\bar{l}$ what we get is

$$\bar{R}_{\mu\nu} - \frac{1}{2}\bar{g}_{\mu\nu}\bar{R} = \frac{8\pi G}{c^4}\left(\bar{T}_{\mu\nu} - t_{\mu\nu}\right) \tag{1.71}$$

In this case the upper "$^-$" is related to the smoothed out tensors obtained from the average on $\bar{l}$. We get $t_{\mu\nu}$ which is the term related to the energy since $t_{\mu\nu} \sim o(h^2)$.

$$t_{\mu\nu} = -\frac{c^4}{8\pi G}\left\langle R^{(2)}_{\mu\nu} - \frac{1}{2}\bar{g}_{\mu\nu}R^{(2)}\right\rangle \tag{1.72}$$

It is interesting to notice that using the correct gauge combination we can get a relatively simple expression of $t^{\mu\nu}$ such that

$$t^{\mu\nu} = \frac{c^4}{32\pi G}\langle \partial_\mu h_{\alpha\beta}\partial_\nu h^{\alpha\beta}\rangle \rightarrow t^{00} = \frac{c^2}{16\pi G}\langle \dot{h}_+^2 - \dot{h}_x^2\rangle \tag{1.73}$$

Where in the last passage we are considering the TT gauge. In particular the term $t^{00}$ is the energy density of the gravitational wave, which can be used to obtain the energy flux of a gravitational wave. Also this term allow us to assert that there is an exchange in energy between the gravitational waves and the matter source [2] through the equation

$$\bar{D}^\mu(\bar{T}_{\mu,\nu} + t_{\mu\nu}) = 0 \tag{1.74}$$

Where $\bar{D}^\mu$ identifies the covariant derivative.

# 2

# Detection of Gravitational waves, Interferometers and noise resources

During the Gravitational waves exploration the use of the interferometers showed up to be necessary, mostly due to their capacity to observe a wide band of frequency. Those instruments are most advanced and useful technology to measure the GW; but let us start with an overview of fundamental tools needed to define and characterize the measurement of a Gravitational Wave such as the Power Spectral Density and the Transfer Function.

## 2.1 Some basic tools

In order to understand properly what are the physical quantities that we need when we work with Gravitational Waves detectors, it is useful to introduce a couple of useful concepts: the transfer function and the Power Spectral Density.

### 2.1.1 Power Spectral Density

Given a signal $x(t)$ where its statistical properties are well defined, we define PSD of this signal as the fourier transform of the autocorrelation function. More formally we assume that the signal is

- Stationary: The statistical properties are time independent
- Gaussian: $x(t)$ is normally distributed for fixed $t$
- Ergodic: time and ensemble statistical property coincide
- If the signal is just noise, being stochastic is required: The autocorrelation function decrease quickly in time

So we define the autocorrelation function as

$$R(t, t') = \langle x(t)x(t') \rangle = R(\tau = t - t') \tag{2.1}$$

Where the notation $\langle\rangle$ identify the mean over a weight function $f(x)$. Formally

$$\langle y(t) \rangle = \int_{-\infty}^{\infty} dxyf(x) \tag{2.2}$$

So the Power Spectral Density of a signal $x$ is finally defined as $S_x(\omega)$

$$S_x(\omega) = \int_{-\infty}^{\infty} d\tau R(\tau) e^{i\omega\tau} \tag{2.3}$$

We can associate to the PSD the meaning of power density in frequency space.

### 2.1.2 Transfer Function

A generic input can be build as infinite sum of $\delta$ signal

$$i(t) = \int_{-\infty}^{\infty} dt' i(t')\delta(t - t') \tag{2.4}$$

So the output will be

$$o(t) = F\Big[ \int_{-\infty}^{\infty} dt' i(t')\delta(t - t') \Big] \tag{2.5}$$

Where F identifies the Fourier Transform. So

$$o(t) = \int_{-\infty}^{\infty} dt' i(t') F(\delta(t - t')) \tag{2.6}$$

The $F(\delta(t-t'))$ is the impulse response, so

$$o(t) = \int_{-\infty}^{\infty} dt' i(t') F(\delta(t-t')) = \int_{-\infty}^{\infty} dt' i(t') h(t,t') = \int_{-\infty}^{\infty} dt' i(t') h(t-t') \tag{2.7}$$

Applying now the convolution theorem we get

$$o(t) = i(\omega) h(\omega) \tag{2.8}$$

Where finally $h(\omega)$ is the transfer function. So the PSD can be defined as

$$S_o(\omega) = |h(\omega)|^2 S_i(\omega) \tag{2.9}$$

This relation is quite useful since it relates the PSD of the output directly to the PSD of the input through the transfer function.

## 2.2 Interferometers and Gravitational Waves

We can start from a schematization of a Michelson-Morley interferometer, which is useful to introduce even if in real life we use Interferometers with Fabry-Perot cavity.

In the Michelson and Morley interferometer we work in the free falling frame [2]. The basic idea is to build an instrument capable of measuring the interferometric phenomena of light due to the passage of a Gravitational Waves. Considering two orthogonal arms, where at the end of each there is a mirror, a LASER, generated by a source at the beginning of one arm, runs along the length of the arm, until it reaches the beam splitter. Here a fraction of it passes the beam splitter and the remaining fraction is deviated to the other arm. Those two laser beams then hit the mirrors at the end of the arms and are reflected back to the beam splitter. Here the two beams recombines and, if there is a difference in length due to the passage of a Gravitational Wave, they will generate interference phenomena, due to the changes in the length of arms which is reflected in the time of fly of the photons of the LASER beam, at this point the recombined beams hit the detector and what we measure is the intensity of the beam. Given L the distance between the beam splitter and the mirror as the Figure 2.1 describes, we can build up the equation for measuring the input of the detector, which is an intensity. Using a laser provided by the source, we have $\frac{\omega_l}{c} = \lambda_l$, where $\omega_l$ is the laser frequency, while $\lambda_l$ is the laser wavelength. Clearly $\lambda_l = \frac{2\pi}{k_l}$. Clearlt $k_l$ is the wave length of the LASER beam The electro-magnetic wave emitted from the source has this expression

$$E_{in} = e^{-i(\omega_l t - \vec{k_l}\cdot\vec{x})} \tag{2.10}$$

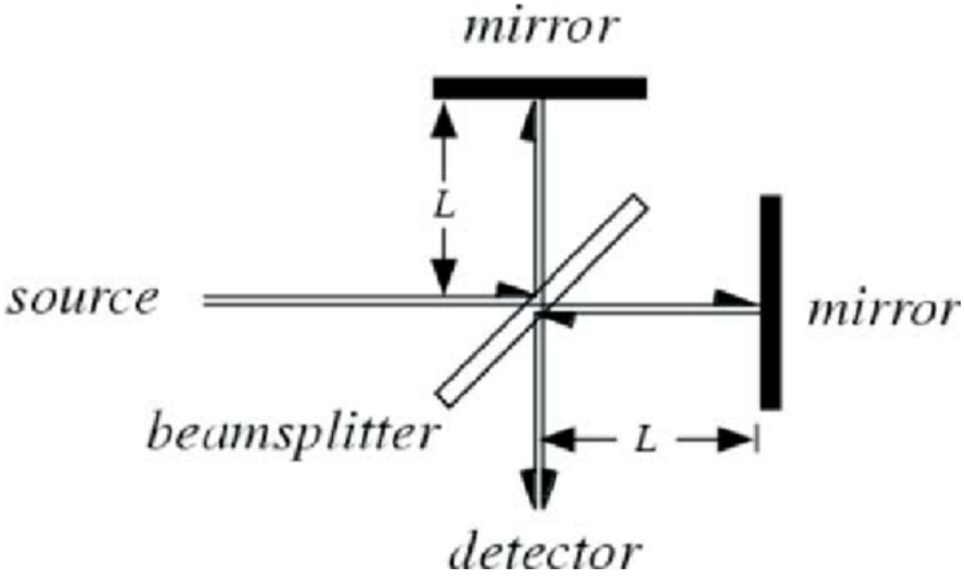


**Figure 2.1:** A schematic view of Michelson Morley interferometer. For reference see [3]

As convention we consider an extra phase $\pi$ every time the laser beam is reflected, but just when the LASER goes through a material of refraction index $n_2 > n_1$, coming from $n_1$ and going to $n_2$. So out of the beam splitter we get

$$E_x = \frac{E_{in}}{2} e^{i(kx-\omega_1 t+\varphi_x)} \tag{2.11}$$

$$E_y = \frac{E_{in}}{2} e^{i(kx-\omega_1 t+\varphi_y)} \tag{2.12}$$

Clearly $E_{out} = E_x + E_y$ and $I_{out} = |E_{out}|^2$ so

$$I_{out} = \frac{E_0}{2}(1 + \cos(k(x-y) + (\varphi_x - \varphi_y)) \tag{2.13}$$

As we see from figure (2.1) there are two outputs, one arriving to the detector, $I_{out1}$, and the other one hitting the LASER source $I_{out2}$, formally

$$I_{out1} = E_0^2 \sin^2\left(\frac{k(x-y)}{2}\right) \tag{2.14}$$

$$I_{out2} = E_0^2 \sin^2\left(\frac{k(x-y)}{2} + \frac{\pi}{2}\right) \tag{2.15}$$

### 2.2.1 IFO - GW interaction in the detector frame

We can describe the GW interaction as a Newtonian force acting on the mirrors, here the coordinates are marked by a rigid ruler [2]. This means that, as we have seen before

$$F_x \simeq \frac{m}{2} x_0 \ddot{h}_{xx}^{TT} \tag{2.16}$$

This is due to the fact that the perturbation is small compared to L, so $x \sim x_0$, where $x_0$ is the coordinate of the test mass at reast then

$$\ddot{x} = \frac{1}{2} x_0 \ddot{h}_{xx}^{TT} \tag{2.17}$$

We must stress that those expressions are valid in the following conditions, that $x << \lambda_{GW}$, which means that $f_{GW} << \frac{c}{L} \sim 100\text{kHz}\left(\frac{L}{3\text{km}}\right)$, also we are dealing with a background - spacetime variation well separated by those introduced by the gravitational waves. If we assume a plus polarized wave travelling along the $\hat{z}$ axis hitting the interferometers of which arms are along $\hat{x}$, $\hat{y}$ and the beam splitter as the origin we get for the Test Mass (TM) (i.e. the mirrors) at the $\hat{x}$ axis

$$x_{XTM}(t) = L_x + \frac{h_0 L_x}{2}\cos(\omega_{GW} t) \tag{2.18}$$

$$y_{XTM}(t) = \dot{y}_{XTM}(t) = 0 \tag{2.19}$$

While for the $\hat{y}$ axis

$$x_{YTM}(t) = \dot{x}_{XTM}(t) = 0 \tag{2.20}$$

$$y_{YTM}(t) = L_y - \frac{h_0 L_y}{2}\cos(\omega_{GW} t) \tag{2.21}$$

Clearly $x_{XTM}, y_{XTM}$ are the x and y coordinates for the T.M. in the $\hat{x}$ arm, while $x_{YTM}, y_{YTM}$ are the x and y coordinates for

the T.M. in the $\hat{y}$ arm. So if we insert these expressions in (2.15) and performing some calculations we get

$$I_{out} = E_0^2 \sin^2\Big(k(L_x - L_y + h_0 L\cos(\omega_{GW} t))\Big) \tag{2.22}$$

What we do measure basically is the time of flight of the photon in the Interferometer, so even if the GW stretches the light, we can see its effect. But for a more complete description let's move to the TT Gauge.

### 2.2.2 IFO - GW INTERACTION IN THE TT GAUGE

In this representation the mirrors do not move since they are free falling. Instead the the light propagation is affected through a stretched space-time [2], so the proper distance $ds^2$ is

$$ds^2 = -cdt^2 + (1 + h_+(t))dx^2 + (1 - h_-(t))dy^2 + dz^2 = 0 \tag{2.23}$$

The last relation holds for the photons. So for the x arm is easy to obtain

$$dx = \sqrt{\frac{c^2 dt^2}{1 + h_+(t)}} \sim \pm c dt\Big(1 - \frac{1}{2}h_+(t)\Big) \tag{2.24}$$

If we define as $t_0$ the time when the photon leaves the beam splitter and as $t_2$ the time when the photons hits back the Beam splitter, integrating the previous expression defining $\tau = \frac{2L_x}{c} + t_0$ it is easy to obtain [2]

$$t_2 - t_0 = \frac{2L_x}{c} + \frac{1}{2}\int_{t_0}^{\tau} dt h_0 \cos(\omega_{GW} t) = \frac{2L_x}{c} + \frac{L_x}{c} h_+\Big(t_0 + \frac{L_x}{c}\Big) \frac{\sin\Big(\frac{\omega_{GW} L_x}{c}\Big)}{\frac{\omega_{GW} L_x}{c}} \tag{2.25}$$

We can define the $\frac{\sin\Big(\frac{\omega_{GW} L_x}{c}\Big)}{\frac{\omega_{GW} L_x}{c}}$ as the $\mathrm{Sinc}(\frac{\omega_{GW} L_x}{c})$ function.

There are two limit cases we need to consider, the first is when $\frac{L_x}{c} << T_{GW} = \frac{2\pi}{\omega_{GW}}$, which means that the perturbation is static during the light's travel time. Instead for the case $\frac{L_x}{c} >> T_{GW}$ during the light's time travel the term $h_+$ keeps oscillating, cancelling out its effect at a very full period. So now defining $t = t_2$ the time when the photon get back to the beam splitter: $t_0 \sim t - \frac{2L}{c}$ in h, then

$$t_0^x = t - \frac{2L_x}{c} - \frac{L_x}{c} h_+\Big(t - \frac{L_x}{c}\Big) \mathrm{sinc}(\frac{\omega_{GW} L_x}{c}) \tag{2.26}$$

$$t_0^y = t - \frac{2L_y}{c} + \frac{L_y}{c} h_+\Big(t - \frac{L_y}{c}\Big) \mathrm{sinc}(\frac{\omega_{GW} L_y}{c}) \tag{2.27}$$

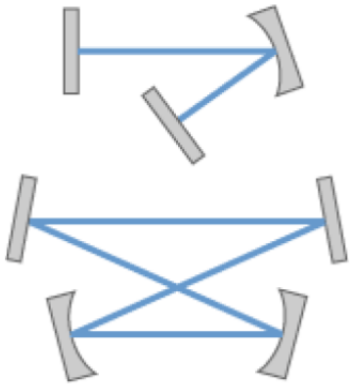

**Figure 2.2:** A simple linear optical cavity with a curved folding mirror (top) and a four-mirror bow-tie ring cavity (bottom), for reference [4]

So the phase difference at the recombination is $\Delta\varphi = \omega_l(t_0^x - t_0^y)$ and performing the math we can obtain

$$\Delta\varphi \simeq \omega_l\left(2 - \frac{L_x - L_y}{c} + \frac{2L}{c}\mathrm{sinc}(\frac{\omega_{GW}L_y}{c})h_0\cos(\omega_{GW}t + \alpha)\right) = \Delta\varphi_0 + \Delta\varphi_{GW} \tag{2.28}$$

It is clear that the first term $\Delta\varphi_0$ can be controlled by the experimentalists, while the $\Delta\varphi_{GW}$ is the phase effect induced by the gravitational wave. Another interest point is that in order to optimize the phase response to the gravitational wave our optical cavity $L = L_{opt}$ should be of the magnitude $L_{opt} \sim 750\mathrm{km}\left(\frac{100\mathrm{Hz}}{f_{gw}}\right)$ [2]. The last statement is equivalent to asking that the time of flight of the photon is the cavity lasts $t_{cav} = \frac{1}{4f_{GW}}$. This will lead us to a more sophisticated Optical Interferometer: the Frabry-Perot interferometers.

### 2.2.3 Fabry-Perot IFO

As we mentioned before the basic idea is to build an instrument where the phase shift due to the passage of the Gravitational Wave is maximised, which means to gain the time of flight of the photons. This can be done by building up an optical resonant cavity. Let us start by defining this object.

#### Optical Cavity

We define an optical cavity as an arrangement of mirrors that allows a closed path for the light.

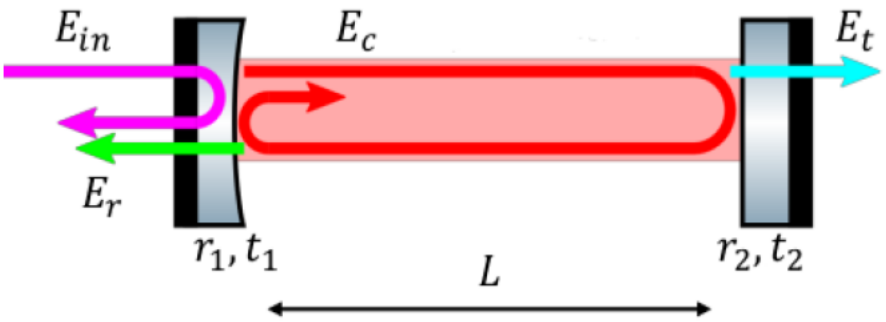


**Figure 2.3:** Fields inside the cavity. Entering electric field $E_{in}$, reflected $E_r$, circulating $E_c$ and transmitted $E_t$. L is the length of the cavity. Transmission coefficients $t_1$, $t_2$ and reflective coefficients $r_1$, $r_2$. Image taken from the Gravitational Physics course held by Prof. Ciani - 2021

We can define the following electric fields. Given an entering electric field $E_{in}$ the reflected $E_r$ and the transmitted $E_t$ fields are related by the coefficients r and t in such way

$$E_r = rE_{in} \tag{2.29}$$

$$E_t = tE_{in} \tag{2.30}$$

With $t, r \in R$. Also this relation holds

$$r^2 + t^2 = 1 \tag{2.31}$$

The fields circulating in the cavity can be schematized as in Figure 2.3.

Following this scheme we see that the circulating field $E_c$, the transmitted $E_t$ and the reflected $E_r$ fields are

$$E_c = E_{in}\frac{t_1}{1 - r_1 r_2 e^{-2ikL}} \tag{2.32}$$

$$E_t = E_{in}\frac{t_1 t_2}{1 - r_1 r_2 e^{-2ikL}} \tag{2.33}$$

$$E_r = -E_{in}\frac{r_1 - r_2 e^{-2iKL}}{1 - r_1 r_2 e^{-2ikL}} \tag{2.34}$$

What we are interested in is the set that satisfies the resonance conditions. From the fields expressed in the previous equations we can obtain the circulating intensity $I_c$ as

$$I_c = |E_c|^2 = E_{in}^2 \left| \frac{t_1}{1 - r_1 r_2 e^{2ikL}} \right|^2 \tag{2.35}$$

This expression is maximized if the phase element $e^{2ikL} = 1$, so there will be constraints to L such as $L = n\frac{\pi}{k} = n\frac{c}{2f}$. Clearly at the resonance the $I_c$ will be

$$I_c = I_{in} \left| \frac{t_1}{1 - r_1 r_2} \right|^2 \tag{2.36}$$

Then we can define two important quantities related to the resonance, the Free Spectral Range (FSR) and the Finesse (F).

$$FSR = \frac{c}{2L} \tag{2.37}$$

$$Finesse = \frac{\pi\sqrt{r_1 r_2}}{1 - r_1 r_2} \tag{2.38}$$

The Finesse can be also defined as $Finesse \sim \frac{FSR}{FWHM} \sim \frac{2\pi}{losses}$. The FWHM is the Full Width Half Maximum. Graphically we can identify the FSR as the distances between the peaks of the intensity, while the Finesse as how wide are them.

Now it is meaningful to insert the storage time as the time spent by the photon inside the cavity [2]. It is easy to show that this can be obtained considering the probability for a photon to perform n bounces forth and back. The result is

$$\tau_s \simeq \frac{L}{c}\frac{F}{\pi} \tag{2.39}$$

So for example if we insert as values $r_1^2 = 0.99$, $r_2 = 1$, $L = 3km$, $F = 625$ then $\tau_s = 2ms$.

### 2.2.4 Response of Fabry-Perot arm cavity

In order to obtain the transfer function we need to understand how the phase changes as a function of the cavity. It can be shown that a coupling factor $\sigma$ can be defined. Given an effective power loss p such as $1 - p_i = r_i^2 - t_i^2$, then

$$1 - p = (1 - p_1)r_2^2 \tag{2.40}$$

So the coupling factor can be defined as

$$\sigma = \frac{pF}{\pi}, 0 < \sigma < 2 \tag{2.41}$$

We can identify three range for this factor [2]

- for $0 < \sigma < 1$ the cavity is overcoupled
- for $\sigma = 1$ the cavity is impedance matched
- fot $1 < \sigma < 2$ the cavity is undercoupled

Now let us suppose there is a small phase displacement $\varepsilon = 2k_l\delta l$ from resonance. Then the phase reflected field can be written as

$$\varphi = \pi + \arctan\left(\frac{F\varepsilon}{\pi}\frac{1}{1-\sigma}\right) + \arctan\left(\frac{F\varepsilon}{\pi}\right) \tag{2.42}$$

Also here we can have three ranges, for $\sigma > 1$ there is partial cancellation of light, for $\sigma = 1$ no light at all and for $\sigma < 1$ more light but less phase sensitivity. As first approach just imposing $r_2 = 1$, $r_1 = 1$ and $p_1 = 0$ we ge

$$p = 1 - r_2^2 = 0 \rightarrow \sigma = 0 \rightarrow \frac{\partial\varphi}{\partial\varepsilon} = \frac{2F}{\pi} \tag{2.43}$$

If we now consider a IFO with Fabry-Perot cavities invested by a Gravitational Wave plus polarized perpendicular to the plane of the IFO, in the detector frame, the total phase shift will be a combination of the shift in $\hat{x}$ and $\hat{y}$, so

$$\Delta\varphi_{FP} = \Delta\varphi_x - \Delta\varphi_y 4k_l\frac{1}{2}Lh_0\cos(\omega_{GW}t)\frac{2F}{\pi} \tag{2.44}$$

The magnitude of this phase shift will be

$$|\Delta\varphi_{FP}| = \frac{4F}{\pi}k_lLh_0 \tag{2.45}$$

From this equation, moving to the TT gauge, it is possible to obtain the Transfer function from h to $\Delta\varphi$ as

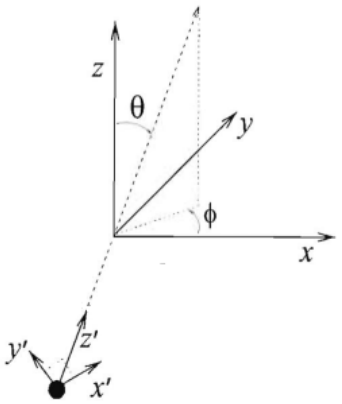


**Figure 2.4:** The geometry used in the computation of the antenna pattern function, the ' coordinates are the coordinates of source while the arms of the interferometer are along x and y. For reference see [2]

[2]

$$T_{FP}(f_{gw}) = \frac{8FL}{\lambda_l} \frac{1}{\sqrt{1 + \frac{f_{GW}}{f_p}}} \tag{2.46}$$

Where $f_p = \frac{1}{4\pi\tau_s}$

### 2.2.5 Antenna Pattern

The antenna pattern is needed in order to formalize the response of an interferometer, or a network of interferometers to a generic polarized gravitational wave. This is encoded in the pattern functions $F_+(\theta, \varphi)$ and $F_x(\theta, \varphi)$ [2]. So we can define now a detector tensor $D_{i,j}$, which transforms the GW input tensor into a scalar input for the detector [2]: $h(t) = D_{i,j}h_{i,j}(t)$. Where h is defined by $F_+(\theta, \varphi)$ and $F_x(\theta, \varphi)$ in the following way [2]

$$h(t) = h_+ F_+(\theta, \varphi) + h_x F_x(\theta, \varphi) \tag{2.47}$$

Since the detector has arm along $\hat{x}$ and $\hat{y}$ directions, the tensor results in

$$D_{i,j} = \frac{1}{2}(\hat{x}_i\hat{x}_j - \hat{y}_i\hat{y}_j) \tag{2.48}$$

As the Figure 2.4 suggests, the directions of the reference frame $(\hat{x}, \hat{y}, \hat{z})$ are such that there the interferometer is along the

$\hat{x}$ and $\hat{y}$ axes, while the reference $(\hat{x}', \hat{y}', \hat{z}')$ identify the source, with direction of propagation parallel to $\hat{z}'$. In the $(\hat{x}, \hat{y}, \hat{z})$ frame the $\hat{z}'$ axis form two polar angles $\theta$ and $\varphi$. So the polarization $h_x$ and $h_+$ are defined with the respect to the$(\hat{x}', \hat{y}')$ axes, so in the $(\hat{x}', \hat{y}', \hat{z}')$ frame [2] the GW has the form

$$h'_{i,j} = \begin{pmatrix} h_+ & h_x & 0 \\ h_x & -h_+ & 0 \\ 0 & 0 & 0 \end{pmatrix}_{i,j} \tag{2.49}$$

So now we can apply the rotation matrix R which is

$$R = \begin{pmatrix} \cos(\varphi) & \sin(\varphi) & 0 \\ -\sin(\varphi) & \cos(\varphi) & 0 \\ 0 & 0 & 1 \end{pmatrix} \begin{pmatrix} \cos(\theta) & 0 & \sin(\theta) \\ 0 & 1 & 0 \\ -\sin(\theta) & 0 & \cos(\theta) \end{pmatrix} \tag{2.50}$$

Applying this and using the fact that $h_{i,j} = R_{i,k} R_{j,l} h'_{k.l}$ we can obtain [2]

$$F_+(\theta, \varphi) = \frac{1}{2}(1 + \cos^2(\theta)\cos(2\varphi)$$
$$F_x(\theta, \varphi) = \cos(\theta)\sin(2\varphi)$$

We notice that the interferometer is not sensitive to all the source sky position [2].

### 2.2.6 Toward a realistic IFO

In this short section we just want to show in a general perspective which are the most important features of a modern IFO used for GW detecting. Firstly we saw that Fabry-Perot cavities are needed in order to set the interferometer on a human-Earth acceptable scale. So the first point is that the LASER used inside the IFO must maintain its profile. That's why we use a Gaussian beam [2]. In this way the LASER can be tuned to the geometric characteristics of the IFO and hold up his operativity. Other features we must hint are the input mode cleaner, power recycling, controls and locking. In Figure 2.5 we can see a scheme of how a realistic IFO looks like.

Synthetically the power recycling is a method which, as the name suggests, helps us in recycling the power which comes back toward the LASER. We achieve that by placing a mirror between the LASER and the beam splitter [2]. This creates a new Fabry-Perot cavity which is resonant, enhancing the power circulating. For Virgo we talk about $\sim$ 15kW. The input and output mode cleaner also helps us in cleaning up the beam profile, allowing us to reach an almost monochromatic beam.

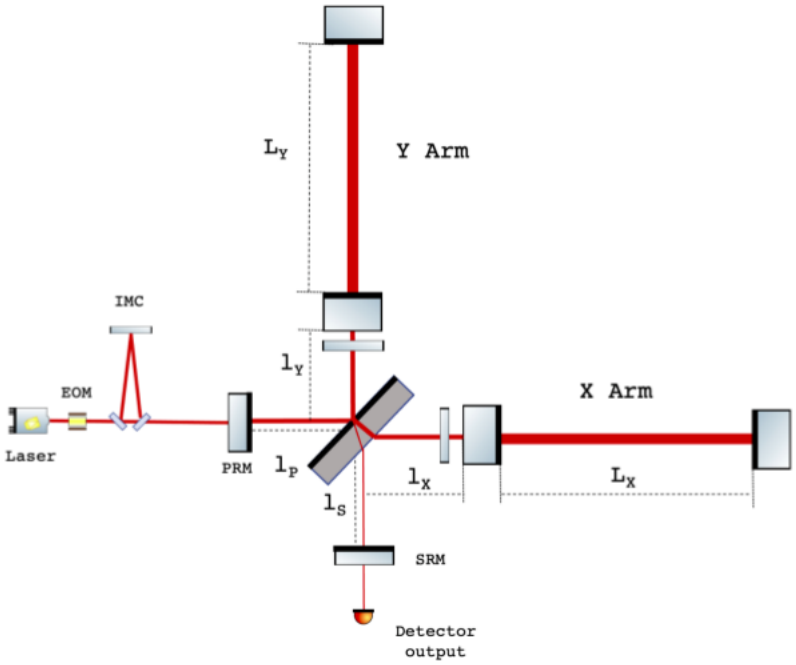


**Figure 2.5:** Double Recycled Fabry–Perot Michelson interferometer configuration: PRM indicates the power recycling mirror, SRM the signal recycling mirror and input mirror and end mirror form the Fabry–Perot optical cavities in each arm. The thickness of the red lines indicating the beam path, is proportional to the amount of power circulating into the detector. For reference see [5]

### 2.2.7 IFO Noise Sources

Let us focus for a moment to the order of magnitude we are willing to measure. Let us suppose there is a phenomena which causes the production of Gravitational Waves, in the Virgo cluster of galaxies, releasing an energy of $\sim 10^{-2}$ solar masses. This results in a Gravitational Wave on Earth of $h_0 \sim 10^{-21}$. If we assume a length of the arm of the IFO of $\sim$ 4km we have a displacement of the mirror of $\Delta L = \left(\frac{1}{2}\right) h_0 L \sim 2x10^{-18}$m [2], which means $h_0 \sim 10^{-21}$. In terms of phase shift we have the following order of magnitude $\Delta\varphi_{FP} \sim 10^{-8}$rad. Supposing a LASER wavelength $\lambda_L = 1\mu$m and a Finesse $F = 200$. So it is vital to understand deeply the noise sources and their magnitude in order to reduce them and allowing the access to a physical meaningful measure. We know that the input $s(t)$ of the detector will be a time series given by the sum of the signal $\xi(t)$ and the noise $n(t)$: $s(t) = \xi(t) + n(t)$. So the autocorrelation function (2.1) related to the noise will be

$$R(\tau) = \langle n(t+\tau)n(t)\rangle \tag{2.51}$$

the PSD of the noise $S_n$ results in

$$\frac{1}{2}S_n(f) = \int_{-\infty}^{\infty} d\tau R(\tau) e^{i2\pi f\tau} \tag{2.52}$$

Then we associate to the detector the spectral strain sensitivity $\sqrt{S_n(f)}$, with dimension $[Hz]^{-1/2}$. This means that in order to measure a Gravitational Wave, IFO must have a strain sensitivity at least $h \sim 10^{-21}\sqrt{Hz}$. Modern intreferometers shows a sensitivity if the order $h \sim 10^{-23}\sqrt{Hz}$ and a band of frequency $[10 - 10kHz]$. The most important noise sources are: seismic noise, gravity gradient noise, thermal noise and quantum noise. Let's start with quantum noise, due to the quantum nature of light, which is characterized by two contributions: Shot Noise and Radiation Pressure.

#### Shot Noise

This kind of noise originates from the fact that the laser light comes in discrete quanta, the photons [2]. It is easy to show that the fluctuation in the number of photons is $\Delta N_\gamma = \sqrt{N_\gamma}$ follows a Poisson Distribution. Consequently the fluctuation in power (P) is given by

$$(\Delta P)_{shot} = \left(\frac{\hbar\omega_L}{T}P\right)^{\frac{1}{2}} \tag{2.53}$$

T is the time we are considering for counting the number of photons N. The power variation in the photodetector due to a Gravitational Wave is [2]

$$(\Delta P)_{GW} = \frac{P_0}{2}|\sin 2\varphi_0|(\Delta\varphi) = \frac{P_0}{2}|\sin 2\varphi_0|\frac{4\pi L}{\lambda_l}h_0 \tag{2.54}$$

So the signal to noise ratio results in

$$\frac{S}{N} = \frac{(\Delta P)_{GW}}{(\Delta P)_{shot}} = \left(\frac{P_0 T}{2\hbar\omega_L}\right)^{\frac{1}{2}} \frac{4\pi L}{\lambda_L} h_0 \tag{2.55}$$

So supposing there is a periodic GW signal arriving at time T, the signal to noise ratio can be written in terms of the Strain Sensitivity $S_n(f)$ [2]

$$S_n^{\frac{1}{2}}(f)|_{shot} = \frac{\lambda_l}{4\pi L}\left(\frac{2\omega_L}{P_0}\right)^{\frac{1}{2}} \tag{2.56}$$

Obtaining

$$\frac{S}{N} = \left[\frac{T}{S_n(f)}\right]^{\frac{1}{2}} h_0 \tag{2.57}$$

So it is simple to extend the equation including the effects of the Fabry-Perot cavity and the frequency dependency of the GW

$$S_n^{\frac{1}{2}}(f)|_{shot} = \frac{1}{8FL}\left(\frac{4\pi\hbar\lambda_L c}{\eta P_{bs}}\right)^{\frac{1}{2}} \sqrt{1 + \left(\frac{f}{f_p}\right)^2} \tag{2.58}$$

Where the new terms are: $\eta$ for the efficiency of the photodiode for extracting the electrons, $P_{bs}$ the power on the beam splitter after the recycling, and f is the frequency of the GW.

## Radiation Pressure

We can easily assert that a beam of photons hitting a mirror exert a pressure over it, and this is not constant since the photons arrive following a specific distribution [2]. Is it easy to show that this force grows as $\sqrt{P_{bs}}$ while the shot noise behaves like $\frac{1}{\sqrt{P_{bs}}}$, so we need to find a balance between those two behaviours. Following a procedure similar to the one used in the shot noise, we arrive at the following expression for the strain sensitivity due to the radiation pressure

$$S_n(f)^{\frac{1}{2}}|_{rad} = \frac{16\sqrt{2}F}{ML(2\pi h)^2}\sqrt{\frac{\hbar}{2\pi}\frac{P_{bs}}{\lambda_L c}}\frac{1}{\sqrt{1 + \left(\frac{f}{f_p}\right)^2}} \tag{2.59}$$

Where M is the mass of the mirror. We can now define the Standard Quantum Limit.

### Standard Quantum Limit

We can start defining the optical readout noise as

$$S_n(f)|_{opt} = S_n(f)|_{shot} + S_n(f)|_{rad} \tag{2.60}$$

So performing the maths using the previous expression we get

$$S_n(f)^{\frac{1}{2}}|_{opt} = \frac{1}{L\pi f_0}\sqrt{\frac{\hbar}{M}\left[\left(1+\frac{f^2}{f_p^2}\right)+\left(\frac{f_0^4}{f^4}\frac{1}{1+(f^2/f_p^2)}\right)\right]} \tag{2.61}$$

With $f_0 = \frac{4F}{\pi}\sqrt{\frac{P_0}{\pi\lambda_L cM}}$. So, the optimal value for $f_0$ is the one where the radiation pressure and the shot noise terms contribute equally, the envelope of those values is called standard quantum limit [2].

$$S^{\frac{1}{2}}_{SQL}(f) = \frac{1}{2\pi fL}\sqrt{\frac{8\hbar}{M}} \tag{2.62}$$

### 2.2.8 Other Noise sources

Let us conclude this excursus about IFO considering the other noise sources which contribute to the Strain of the instrument. The other three noise sources are Thermal Noise, Seismic Noise and Newtonian. Thermal noise is generally gained by any source of dissipation, whether it is internal or external. In particular the mirror suspensions need a specific treatment in order to deal with this noise source. For example we need to use low-loss materials like fused silica, or monolithic mirrors and suspensions. The seismic noise is quite relevant, since the ground vibrations have effects that deeply issue the detecting of GW. In order to drastically reduce this noise we consider cascade-pendula, a passive strategy very efficient to prevent this noise. This kind of noise is quite relevant al low frequencies ($\sim 10 - 30$Hz), as we see from image 2.6 which describes the noise budget of Advanced Virgo Interferometer. Also at these frequencies the Newtonian noise relevant. This noise source is due to the stochastic variation of the local gravitational field due to the seismic variation or infrasound. More generally to the variation of the mass density of the ground. This noise cannot be shielded. We can use a strategy to reduce this noise component: an active strategy where we modelize the effects of the noise on the strain and subtract that from the GW signal, or an active strategy which involves going underground where surface waves don't matter and atmospheric variation are reduced.

## 2.3 State of the Art

Right now in the Gravitational Waves research is active an IFOs network compounded by three interferometers leading the research: Livingstone in Louisiana and Hanford in southeastern Washington State, U.S.A., for the LIGO collaboration, and

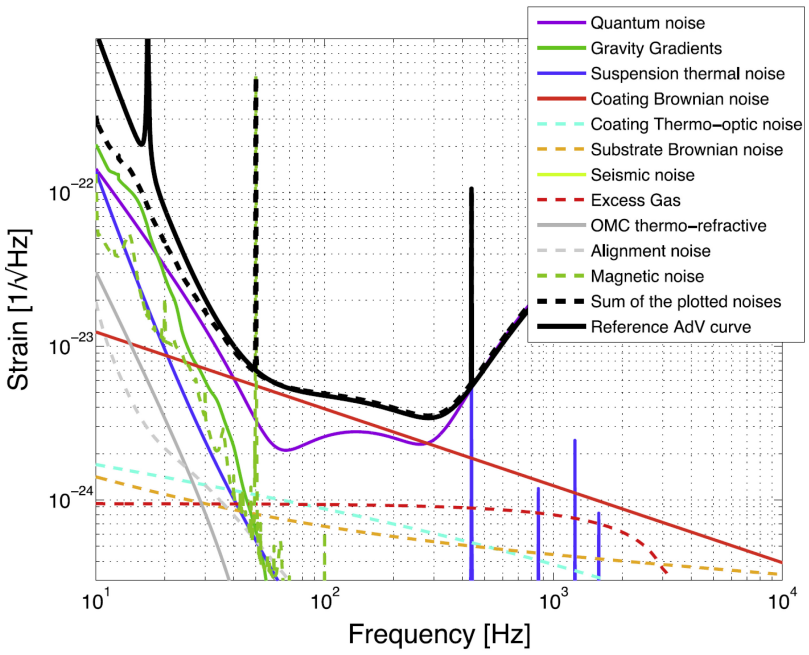


**Figure 2.6:** Advanced Virgo Noise Budged - the noise (dashed black lines) computed as the sum of all the known noise contributions, is compared to a reference AdV sensitivity (solid black line). The contributions from all the single noise sources are also shown. Figure taken from [6]

Virgo in Cascina, Italy.

At the present day, we have completed the O3 acquisition data campaign. Previously, O1 and O2 have been faced. The O1 data acquisition lasted from September 12, 2015 to January 19, 2016 for a total of 130 days [18]. Within the first 16 days the first GW signal has been detected [19], giving birth to the Gravitational Physics research. For the first time the use of cWB, the algorithm used in this project, has been deployed and it contributed to the discovery of the first Gravitational Wave signal. O2 search covered a period from November 30, 2016 to August 25, 2017 [20]. Advanced Virgo joined this observing run in August 1, 2017. The first Binary Neutron Star (BNS) have been detected [21] during O2 data campaign. The analysis of O1 and O2 data produced 11 confident detections, 10 binary Black Hole mergers and one binary Neutron Star merger. The O3 campaign has been split in two different periods: O3a, from April 1st 2019 to October 1st 2019, and O3b, from November 1st 2019 to March 27th 2020 for a total of 146 days. The scientific discoveries of this last campaign are collected in the database GWTC-3 [7]. The catalogues report the observations obtained until the end of the O3b campaign. There are 35 compact binary coalescence candidates. Based upon estimates for the component masses, our O3b candidates are consistent with gravitational-wave signals from binary black holes or neutron star–black hole binaries, and we identify none from binary neutron stars. The range of inferred component masses is similar to that found with previous catalogs, but the O3b candidates include the first confident observations of neutron star–black hole binaries. Including the 35 candidates

from O3b in addition to those from GWTC-2.1, GWTC-3 contains 90 candidates found by the analysis across the first three observing runs. These observations of compact binary coalescences present an unprecedented view of the properties of black holes and neutron stars. GWTC-3 contains candidate GWs from CBCs: merging binaries consisting of black holes (BHs) and neutron stars (NSs). Among these discoveries, there are some which are particularly interesting. The first one is the GW190412 [22]; in this event we have First GW signal observed due to coalescences of two BHs with asymmetric masses of $30^{+4.6}_{-5.3}$ $M_\odot$ , and $8.3^{+1.6}_{-0.9}$ $M_\odot$ . This event is relevant due to its asymmetry, in fact asymmetric systems are predicted to emit gravitational waves with stronger contributions from higher multipoles. Another noticeable event is the GW190525 [23] which is a compact binary coalescence observed by LIGO Livingstone only. The peculiarity is the fact that both of the masses are less than 3 $M_\odot$ . The total mass is significantly larger than those of known binary BNS system ($5\sigma$ from mean of Galactic BNS). Finally we report the case of GW190521 [24] which is interesting since from this BBHs system the remnant BH results to be $142^{+28}_{-16}$ $M_\odot$ , which can be considered an intermediate mass black hole (IMBH).

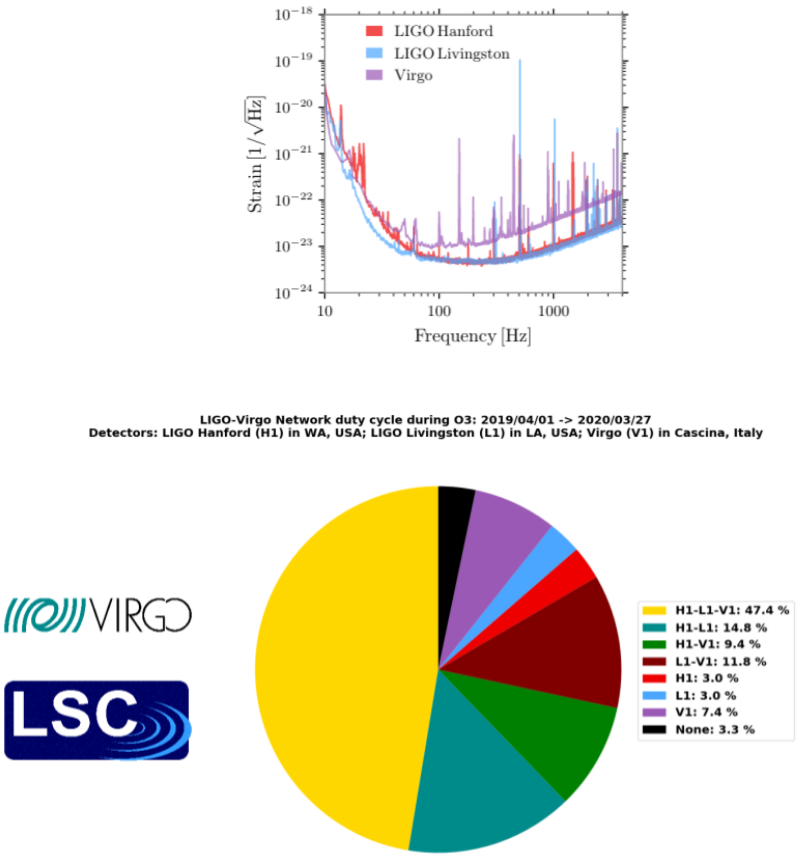


**Figure 2.7:** Strain sensitivity for LHV network [7] (top). The sensitivity is 133 Mpc for Livingstone, 115 Mpc for Hanford and 51 Mpc for Virgo. LIGO-Virgo duty cicle (bottom): the percentage of time that the global detector network formed by Advanced Virgo (labelled as V1) and the two Advanced LIGOs (at Livingston, labelled as L1, and at Hanford, labelled as H1) spent in observation mode during O3: this quantity is referred to as the network duty cycle. [8]

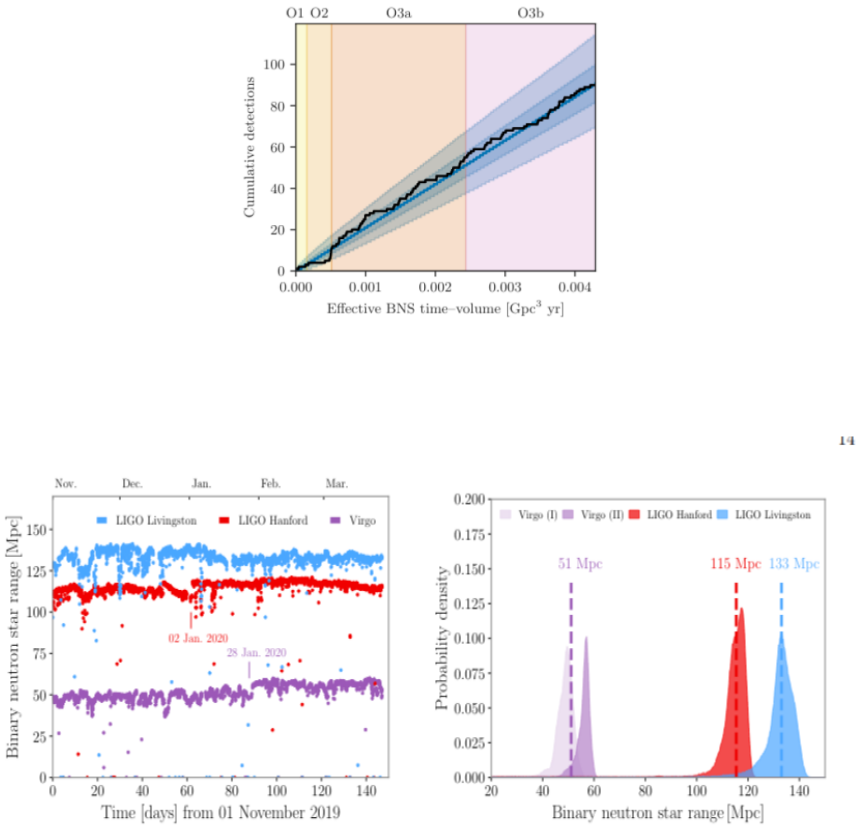


**Figure 2.8:** (Top) The number of CBC detection candidates. The colored bands indicate the different observing runs. The final data sets for O1, O2, O3a and O3b consist of 49.4 days, 124.4 days, 149.8 days (177.2 days) and 125.5 days (142.0 days) with at least two detectors (one detector) observing, respectively. The cumulative number of probable candidates is indicated by the solid black line, while the blue line, dark blue band and light blue band are the median, 50% confidence interval and 90% confidence interval for a Poisson distribution fit to the number of candidates at the end of O3b [7]. (bottom left) The range evolution during O3b. Each data point corresponds to the median value of the range over a one-hour time segment. (bottom right) Distributions of the range and the median values for the entire duration of O3b. [7]

# 3

# coherent WaveBurst: an unmodeled pipeline

First of all we need to underline that in the Gravitational Wave search field we are not looking for events built-up in a laboratory environment, rather we are looking for cosmological-astrophysical phenomena that are very low in happening rate. This means that it is necessary to perform a campaign of simulations to estimate the detection efficiency of the algorithm given a known GW signal.

## 3.1 cWB: a brief introduction

Coherent WaveBurst (cWB) is an analysis pipeline used in searches for generic transient signals with a network of gravitational waves detectors. cWB is not thought to search for a specific astrophysical waveform model, instead it looks for any generic possible signals, exploiting the excess of power in the time frequency representation of the detected signal. It aims to detect and reconstruct events which are possible candidates for Gravitational Waves; the algorithm is based on coherent analysis in multiple detector data and a constrained likelihood approach [25]. We can identify three phases in the cWB algorithm: the pre-production, the production and the post-production. The pre-production phase is needed in order to create the workspace for the analysis. Work directories are created, custom codes and analysis configuration are set up. The production is the run-phase, after this stage a list of triggers are created. In particular each detector's data stream is decomposed in the time

frequency representation then, once the data are whitened, the pipeline proceeds with pixels selection and collection of them in clusters. For each cluster the likelihood function is computed. The likelihood is maximized over a grid of sky positions covering the range of possible directions to the Gravitational Wave source. The default output of cWB is a list of triggers that are Gravitational Waves candidates. For each trigger cWB estimates duration, bandwidth, central frequency and parameters of the signal. Then the post-production is the analysis of the triggers, where we apply vetoes, cuts, custom codes and so on.

## 3.2 Likelihood analysis

We can identify two different categories for the Gravitational Waves analysis, coherent and coincident methods. In coincidence methods, first, a search for GW signals is carried out for individual detectors and a list of candidate events is generated. Then a subset of events is selected by requiring temporal coincidence of events between the detectors. In a coherent method, one, first, combines the detector responses and then analyzes the combined data to generate a single list of events [26] [27]. In a coherent method the detector's network responses are then combined into a functional: the likelihood. So maximizing the likelihood with a sky loop over all the possible sky positions we can reconstruct the waveform, the sky position and the polarization of the burst signal. Let's go into more detail: Gravitational Waves can be represented by a symmetric tensor of second rank $h_{i,j}(t)$ as we have seen in previous chapters. We can now introduce the network response $\xi(t)$ defined as

$$\xi(t) = \frac{1}{2} T_{i,j} h_{i,j}(t) \tag{3.1}$$

Where $T_{i,j}$ is the detector tensor, for references see quote in [26]. In the wave frame the detector response is

$$\xi(t) = F_+ h_+(t) + F_x h_x(t) \tag{3.2}$$

Where $F_+$ and $F_x$ are the antenna pattern (see [26] [28] to obtain the explicit expression for the antenna pattern). Usually we express the detector response in terms of the complex waveform u

$$\xi = \tilde{A} u + A \tilde{u} \tag{3.3}$$

A and $\tilde{A}$ are the complex antenna pattern $A = \frac{1}{2}(F_+ + iF_x)$ and $\tilde{A} = \frac{1}{2}(F_+ - iF_x)$. It is also useful to remember that the network response is invariant under rotation [26].

We can now consider a likelihood analysis of gravitational wave data, which corresponds to setting up a decision problem which maximizes the associated likelihood. The simplest way to solve a decision problem is to define a decision rule through two complementary mutually excluding hypotheses as $H_0$, known as null hypotheses, and $H_1$, the alternative hypothesis. The decision rule is set up by two kinds of possible choices: $H_1$ is selected when the signal is present, while $H_0$ is selected when

just noise occurs. Each possibility will have a probability associated with it: the false alarm and the false dismissal probability, respectively $Q_0$ and $Q_1$. Let us consider an observable that is a finite data segment from a noisy time series such as $x = \{x[1], x[2], ..., x[N]\}$. Clearly this time series is defined as $x[i] = \mathcal{F}h[i] + n[i]$, where $h[i]$ identify the signal while $n[i]$ is related to the noise and $\mathcal{F}$ is the network antenna pattern matrix [29]. Under $H_0$ and $H_1$, x is a realization of a stochastic process described by the joint probability density $p(\vec{x}|H_0)$ and $p(\vec{x}|H_1)$ [26]. The decision rule which fits best for the gravitational wave detection is the Neyman-Pearson criterion. This criterion assumes that the optimal decision rule has the minimum $Q_1$ value for fixed $Q_0$. So the rule accepts $H_1$ when the likelihood ratio $\Lambda(x)$ is greater than a threshold value fixed by a specific $Q_0$. The likelihood ratio is defined as

$$\Lambda(x) = \frac{p(x|H_1)}{p(x|H_0)} \tag{3.4}$$

We can assert that in the Gravitational Wave framework $H_0$ is the hypothesis corresponding to the absence of a Gravitational Wave signal, while $H_1$ is related to the presence of a signal. Let us suppose a Gaussian white noise with zero mean. The corresponding joint probability are then:

$$p(x|H_0) = \Pi_{i=1}^{N} \frac{1}{\sqrt{2\pi}\sigma} \exp\Big( - \frac{x_i^2}{2\sigma^2} \Big)$$
$$p(x|H_1) = \Pi_{i=1}^{N} \frac{1}{\sqrt{2\pi}\sigma} \exp\Big( - \frac{(x_i - \xi_i)^2}{2\sigma^2} \Big)$$

Clearly $\sigma$ is the standard deviation of the noise [26]. What we are interest in are the logarithm of the likelihood ratio, so

$$\mathcal{L} = \ln\Big(\Lambda(x)\Big) = \sum_{i=1}^{N} \frac{1}{\sigma^2} \Big( x[i]\xi[i] - \frac{1}{2}\xi^2[i] \Big) \tag{3.5}$$

Now it is easy to extend this function to a network of detectors. Let index the time series of the $k^{th}$ detector such as $x_k = \{x_k[1], x_k[2], ...\}$. Clearly the detector response to the gravitational wave results $\xi_k[i] = \tilde{A}_k u[i] + A_k \tilde{u}[i]$ Assuming that the noise sources in different detectors are independent [26] we obtain

$$\mathcal{L} = \sum_{k=1}^{K} \sum_{i=1}^{N} \frac{1}{\sigma_k^2} \Big( x_k[i]\xi_k[i] - \frac{1}{2}\xi_k^2[i] \Big) \tag{3.6}$$

K is the number of detectors in the network.

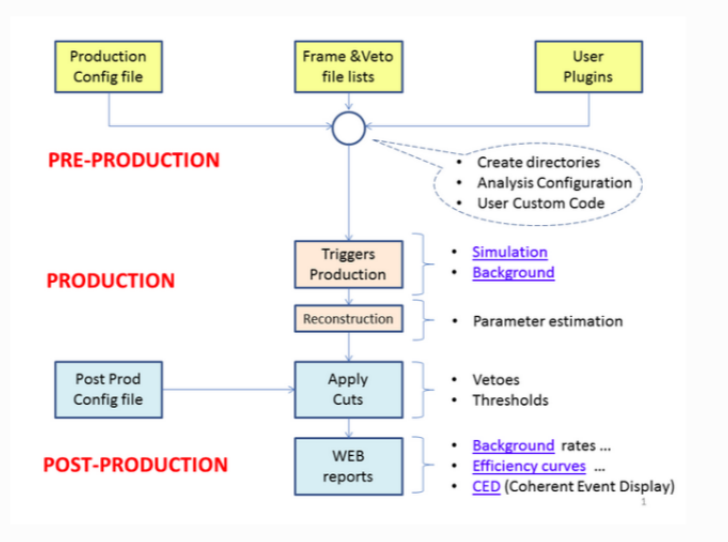


**Figure 3.1:** Flowchart of cWB pipeline. In pre-production we create working directories and configuration files. In production multi stage analysis is performed and in post-production there is the collection of results and creation of figure of merits. For references see [9]

## 3.3 cWB, THE PIPELINE

The implementation of the likelihood method requires a lot of memory and a huge computation load. So the analysis is split into jobs and those data segments are analyzed in parallel. The pipeline's workflow includes a first part in which the pre-production and production stage, obtains a preliminary selection of trigger events based on the likelihood evaluation. The second one instead, which is related to the post-production phase, has a more flexible structure, supported by Plugins (or custom code), which allows us to discharge an analysis of the trigger obtained in the previous phase. The cWB pipeline exploits the ROOT framework developed by CERN.

### 3.3.1 cWB, THE PIPELINE: PRE-PRODUCTION AND PRODUCTION PHASE

The pipeline provides triggers, i.e. Gravitational Waves signal candidates, from the data stream. This goal is achieved in the pre-production and production phase. The most interesting part is the production phase, since the pre-production is just a custom setting of the framework, such as defining the working folders, applying custom codes and so on. Let's focus on the production phase: the data that the cWB pipeline analyzes are conditioned in order to optimize the procedure. We have three main stages in the production phase:

- Data conditioning and wavelet transformation.

- Multiresolution analysis and pixel clustering process.

- Likelihood maximization and triggers selection.

Starting from the first point, the data are represented in the Time-Frequency (TF) plane. The main idea is to perform a Discrete Wavelet Transform, specifically projecting the data in a local orthonormal basis of wavelet function [30]. The TF representation is obtained by the Wilson-Daubechies-Meyer (WDM) TF transformation [29] [30]. This method is more efficient in computing time and gives us a better representation of the signal in the TF plane. Firstly, in order to remove some predictable noise from the data, Linear Prediction Error (LPE) filters are applied. The LPE filters suppress the stationary noisy lines recognized by controls on the Gravitational Waves Channels. This filter is applied in each level of Time-Frequency decomposition. So the time series cleaned by this filter can be obtained performing the inverse transformation. Then the Regression procedure [31] consists in recognizing the noisy lines through the data collected by auxiliary channels. Now we obtain the whitening: considering quasi-stationary Gaussian Noise, the power spectral density of WDM is computed. For each layer cWB computes several values of RMS considering the TF map at its finest resolution, then the TF data samples are scaled by the noise RMS and whitened. The values are given by eq (3.7) [29]

$$w_k[i,j] = \frac{x_k[i,j]}{\sqrt{\sigma_k^2[i,j]}} \tag{3.7}$$

Where k is the index of the detector while $[i,j]$ are the coordinates in the TF plane. The whitening consists in normalizing the energy of the collected data.

After the data are elaborated by the WDM transform, we can proceed with the multi-resolution and selection of the pixel: the algorithm selects the most energetic pixels which describe the signal. Each detector data stream is separately converted in the TF plane where they are represented by pixels with a given time-frequency width. Any level of each detector is analyzed by the pipeline which selects the most energetic pixel called black pixel. The remaining pixels are called white pixels. The procedure is obtained considering all the possible detection delays, which take care of the time a Gravitational Wave signal can hit the IFOs network's components from various positions in the sky. The black pixels that survive this procedure determine the cluster. A cluster is structured by a core black-pixels formed and a halo provided by the white pixels around the black ones. The clustering procedure is optimized considering also the time frequency position of a pixel near a black-pixel which normally will be rejected due to low energy. Also the maximum time frequency distance is taken into account in order to consider pixels belonging to the same cluster.

Finally we must proceed with the likelihood maximization. We must consider in the first place that the likelihood maximization must be performed over a network of K detectors [26]. So we can now introduce the following vectors:

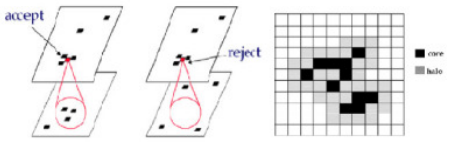


**Figure 3.2:** Clustering process. On the left pixel acceptance for multi-layer analysis. On the right pictorial representation of a cluster. We see on the far left picture that the pixel is accepted due to the superposition within a threshold (the red circle) with the pixel belonging to another layer. Insert in the central picture the pixel is rejected. For references see [10]

$$F_+ = \{F_{1,+}, F_{2,+}, ..., F_{K,+}\} \tag{3.8}$$

$$F_x = \{F_{1,x}, F_{2,x}, ..., F_{K,x}\} \tag{3.9}$$

$$x[i,j] = \{x_1[i,j], x_2[i,j], ..., x_K[i,j]\} \tag{3.10}$$

$$A = \{A_1, A_2, ..., A_K\} \tag{3.11}$$

Where $F_+$ and $F_x$ are defined in section (2) and A in equation (4.3). Also is it useful to define the following normalized vectors

$$f_+ = \{\frac{F_{1,+}}{\sigma_1[i,j]}, \frac{F_{2,+}}{\sigma_2[i,j]}, ..., \frac{F_{K,+}}{\sigma_K}\} \tag{3.12}$$

$$f_x = \{\frac{F_{1,x}}{\sigma_1[i,j]}, \frac{F_{2,x}}{\sigma_2[i,j]}, ..., \frac{F_{K,x}}{\sigma_K}\} \tag{3.13}$$

$$w[i,j] = \{\frac{x_1[i,j]}{\sigma_1[i,j]}, \frac{x_2[i,j]}{\sigma_2[i,j]}, ..., \frac{x_K[i,j]}{\sigma_K[i,j]}\} \tag{3.14}$$

$$\tag{3.15}$$

Then we can introduce the Dominant Polarization Frame (DPF), defined as the the frame where the vectors $f_x$ and $f_x$ are orthogonal, so $(f_+ \cdot f_x) = 0$, and where $\frac{|f_x|}{|f_x|} < 1$ [26]. This will have an impact when, later on, we will introduce the constraints. We can now proceed by maximizing the likelihood functional. The likelihood functional can be written as $\mathcal{L} = \mathcal{L}_+ + \mathcal{L}_x$, where

$$\mathcal{L}_+ = \sum_{i,j=1}^{N} \left[ (w \cdot f_+) h_+ - \frac{|f_+|^2 h_+^2}{2} \right] \tag{3.16}$$

$$\mathcal{L}_x = \sum_{i,j=1}^{N} \left[ (w \cdot f_x) h_x - \frac{|f_x|^2 h_x^2}{2} \right] \tag{3.17}$$

$$\tag{3.18}$$

Now using the fact that in the DPF the vectors $f_+$ and $f_x$ are orthogonal we obtain the following eqautions:

$$(w \cdot f_+) = |f_+|^2 h_+ \tag{3.19}$$

$$(w \cdot f_x) = |f_x|^2 h_+ \tag{3.20}$$

Note, the norms $|f_+|^2$ and $|f_x|^2$ characterize the network sensitivity to the $h_+$ and h polarizations respectively. Now we can obtain the solutions of the maximization by inserting those equation (3.19) and (3.20) in the functional $\mathcal{L}$ and maximizing over the source coordinates $(\theta, \varphi)$, in this way we obtain the maximum likelihood statistics [27]. In general the likelihood functional is calculated, as a sum over the data samples selected for the analysis. The number of terms in the sum depends on the selected TF area in the wavelet domain.

Maximizing this $\mathcal{L}$ among the coordinates $(\theta, \varphi)$ will results in the statistics:

$$\mathcal{L}_m(i,j) = \max_{(\theta,\varphi)} \{\mathcal{L}(i,j,\theta,\varphi)\} \tag{3.21}$$

At this point we can introduce the coherent statistics. In order to do so, is it useful to express the maximum likelihood statistics $\mathcal{L}_m(i,j)$ as

$$\mathcal{L}_m = \sum_{i \in C} w[i] P[i] w^T[i] \tag{3.22}$$

Where C is the set of pixels inside a triggered cluster, and P is the projection build up from the vectors $\vec{e}_+ = \frac{f_+}{|f_+|}$ and $\vec{e}_x = \frac{f_x}{|f_x|}$. Since expression (3.22) results in a quadratic form, we can distinguish two parts: coherent energy ($E_c$) and incoherent energy ($E_i$):

$$E_i = \sum_{i \in C} \sum_{n} w_n[i] P_{n,n}[i] w_n[i] \tag{3.23}$$

$$E_c = \sum_{i \in C} \sum_{n \neq m} w_n[i] P_{n,m}[i] w_m[i] \tag{3.24}$$

Also the null space of P identifies the residual detection noise, which is referred to as null stream [32] [29]. The energy related to this null stream is $E_n$, namely energy of the null stream. From those quantities we can finally define some estimator to evaluate the coherence of the reconstructed trigger. The most important one is the network correlation coefficient $c_c$

$$c_c = \frac{E_c}{|E_c| + E_n} \tag{3.25}$$

which provides a powerful event consistency test to distinguish genuine GW events ($c_c \sim 1$) from spurious events ($c_c << 1$) produced by the detectors. Also we can define the burst detection statistics $\rho_c$

$$\rho_c = \left( \frac{c_c E_c K}{K - 1} \right)^{\frac{1}{2}} \tag{3.26}$$

This is an estimator of the network coherent Signal to Noise Ratio for correlated Gravitational Waves signals recorded by different detectors.

### 3.3.2 Polarization and Network constraints.

The detector noise adds a random vector to the Gravitational Wave responses and randomizes the polarization patterns for weak Gravitational Wave signals [29]. One fundamental parameter which describes the Gravitational Wave pattern is the alignment factor $\alpha$:

$$\alpha = \frac{f_x}{f_+} \tag{3.27}$$

This factor tells us how the $f_x$ polarization is detected by the network, clearly with $\alpha = 0$ we have a perfectly coaligned network, which means that just the $f_+$ polarization can be detected. For the LIGO network, $\alpha << 1$. For this reason we need to introduce polarization and network constraints. Main purpose of these regulators is to eliminate unlikely solutions of the likelihood functional and, therefore, reduce the false alarm rates due to the instrumental and environmental artifacts in the data [29]. The most important constraints we need are the $\gamma$ constraint and the $\delta$ constraint. The $\gamma$ regulator makes a prediction of the reconstructed response. This condition suppress sky locations with the low network sensitivity, where it is unlikely to observe a GW event [9]. The purpose of the $\delta$ regulator is to enhance the constraint for 2 detector sub-networks,

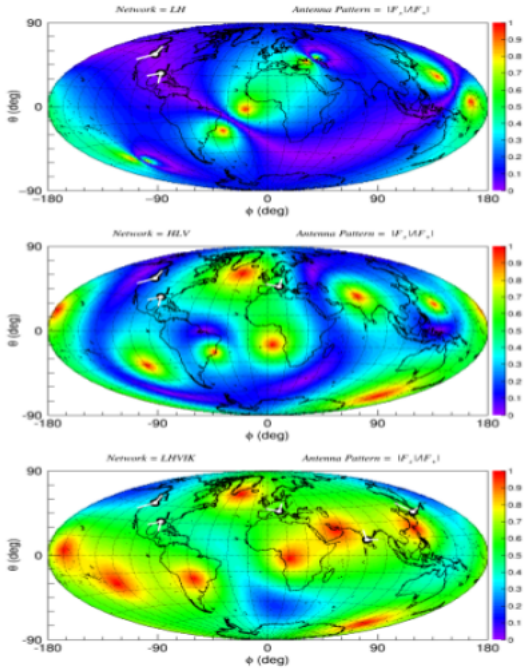


**Figure 3.3:** The distribution of $\alpha$ over the sky for Livingston-Hanford network (top), Livingston-Hanford-Virgo (middle) and Livingston-Hanford-Virgo-Kagra (bottom). The detector site locations and the orientations of the arms are shown on the map. The LIGO-India location is just an example: there is no official site yet.

when other detectors either are not present or are the spectators. Examples of such networks are the LH network and LHV, when the event is produced at low V sensitivity [9]. In the O3b data [16] just the LH network have been analyzed and the IFOs have been forced to be coaligned by the use of constraints. In this thesis we also study the LHV configuration.

### 3.3.3 cWB, THE PIPELINE: POST-PRODUCTION PHASE

In the pre-production and production stage a lot of effort is given in reducing the effect of noise in the signal. Thus the background analysis and the likelihood method are indeed effective, in fact Gaussian noise is well filtered and the signal can be effectively obtained. In case of real signals also non Gaussian transient noise (glitches) are present, and the algorithms need to discriminate also between real signal and glitches. Also, the presence of glitches reduces the effective capability of the algorithm in reconstructing the signal. In order to discharge data periods which are affected by instrumental or environmental noise and discard glitches, the application of vetoes are needed in order to select the period of the data strain provided by the detectors accountable for data analysis. An important selection of the data is performed using the Data Quality associated to the data stream: the vetoes. The Data quality (CAT) is a collection of time periods that are used to evaluate the conditions

of the detector for scientific purposes. There are categories of vetoes numbered from 1 to 5 [33]. Category 1 is the most severe when the detector is locked. Vetoes identified as Category 1 include times where the detector is not in its nominal state/configuration, missing data or has poor calibration. Category 2 contains times of well-understood contamination that are excluded from the data before being processed by individual searches. Category 3 vetoes are statistically significant, but the coupling mechanism is less well understood compared to category 2 vetoes. Categories 1 and 2 vetoes are applied before triggers (times analysis methods identify as significant) are produced while Category 3 vetoes are applied after. Only Categories 1–3 are actively used for data analysis purposes, although their specific usage can vary. Vetoes typically have a duration of a second to a few seconds [9]. Once the CATs are applied, to the triggers that survive this selection another post production tool is used: the cuts. In particular they are applied in parameters such as length of the signal, frequency, $c_c$, $\rho$ value and so on.

## 3.4 Background Analysis

Now we can focus on the procedure used to estimate background statistics. This stage is fundamental in order to define the false alarm rate. The background analysis consists in performing the analysis on a series of data instances obtained with the time shift method. The shift is performed considering times much larger than the one required for a gravitational signal to travel through the space between each detector of the detector network, which are about of ten milliseconds. cWB algorithm is implemented to apply two kinds of temporal shifts. The LAGS and the Super-LAGS.

The LAGS consists of a time shift of the background time series that are split in segments. Each segment refers to a specific period of a detector. Those time series segmentation can be represented by a vector

$$v_{\text{shifts}} = (0, j_2 T_s, ..., j_k T_s, ..., j_N T_s) \tag{3.28}$$

$T_s$ is the value of the minimum temporal shift available, in general the order of magnitude of this shift is $T_s \sim 2s$. The $j_i$ with $i \in \mathcal{N}$ are the lags numbers. Each segment shows a limited number of shifts due to his length, which is limited. The super-LAGS instead involve segments from different periods, exchanging their order for the data stream collected by the detector's network. Then it is applied to the LAG shift. One important quantity associated with this procedure is the live time, which corresponds to the total analyzed time determined by the coincidence periods between all instruments in the network. Once the data instances are divided using this time shift, the pipeline is applied to each job obtained. The result is a list of un-physical triggers that determine the background statistic [27].

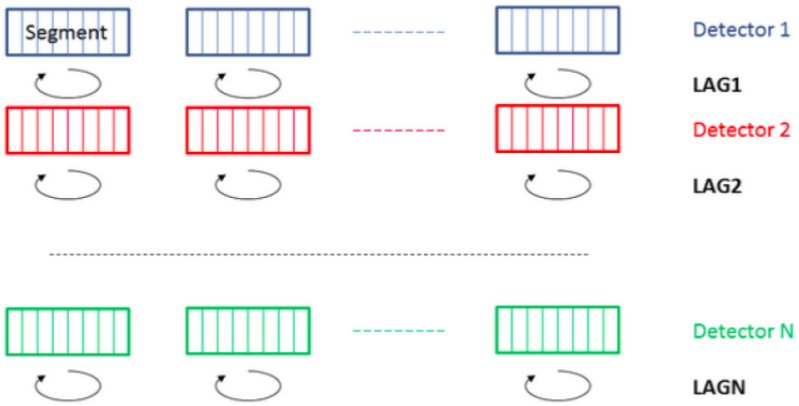


**Figure 3.4:** LAGS: circular time shifts are performed within the detector data. For references see [9]

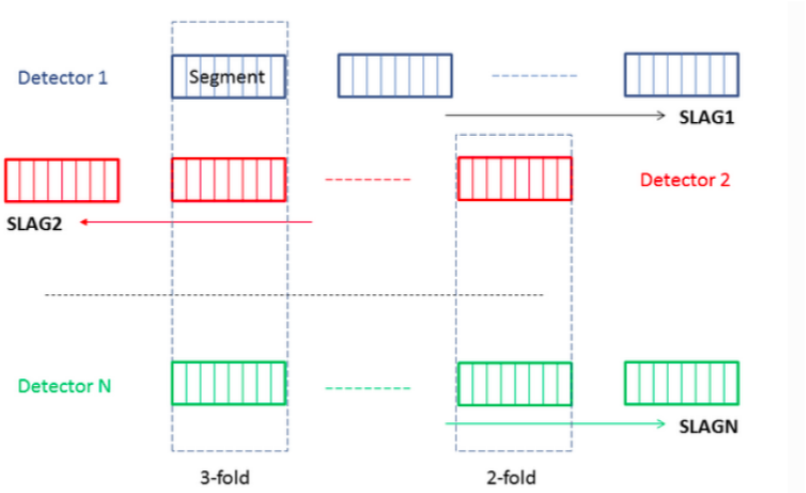


**Figure 3.5:** super-LAGS: time shifts are performed within different segments. For references see [9]

## 3.5 Waveform Models and Simulated Signals

In this thesis we are aiming to study detection efficiency and reconstruction capability of search for long duration transients via cWB algorithm, using the data from O3b campaign. Also O4 will be simulated considering a scaled background. The signals used cover a huge variety of morphologies related to a specific astrophysical process. We will consider the Accretion Disk Instabilities [34], the Binary Neutron Star [35], the GRB plateau [36], the core-collapse Supernovae [15] and the magnetar formed by neutron stars merging [? ].

The Accretion Disks are supposed to play a fundamental role in a lot of astrophysical objects [37] such as Active Galactic Nuclei, close binary system and protoplanetary systems. In general Accretion Disks are the source of Gravitational Waves if there are some instabilities that generate some variation of the mass quadrupole [12]. The parameters referring to these waveforms are reported in the following table.

| Wave type | Mass(Sun) | Duration (s) | Frequency (Hz) |
|---|---|---|---|
| AdiA | 5 | 39 | 135-166 |
| AdiB | 10 | 9.4 | 110-209 |

The other Morphology is provided by the Binary Neutron Star Merging through the NCSACAM_F and the NCSACAM_B wave templates. These waves are interesting because they are related to a merging process in an extreme state of matter like neutron stars. Since this is one of the most violent event in the universe and there is associated over the Gravitational Wave also a full band electromagnetic emission, this process is a perfect tool to study supranuclear dense material and strong gravity regions. The parameters of the process are reported as follow

| Wave type | Mass A (Sun) | Mass B (Sun) | Duration (s) | e | Frequency (Hz) |
|---|---|---|---|---|---|
| NCSACAM_F | 3 | 3 | 15.6561 | 0.6 | 10-200 |
| NCSACAM_B | 1.4 | 1.4 | 181.4691 | 0.4 | 10-275 |

These waveforms are interesting because of their eccentricity. This parameter is peculiar since the emission of Gravitational Waves from a binary system will drastically reduce the eccentricity while approaching the merging stage [2]. The eccentricity could be present just in case of external perturbations, otherwise long before the system approaches the coalescence phase the orbit will be circular.

Another astrophysical process considered for these studies is the Gravitational Wave associated with the birth of a magnetar or a neutron star from a GRB process, the CM09short [13]. The instabilities which are present inside the NS or the Magnetar will lead to a deformation of the astrophysical object cigar-like shape. Consequently an emission of Gravitational Waves is

supposed to happen. The parameters of this waveform are reported in the following table

| Wave type | Mass (Sun) | Duration (s) | Frequency (Hz) |
|---|---|---|---|
| CMo9short | 1.4 | 470 | 251-79 |

Cosmological Gamma Ray Bursts and Core Collapse Supernovae (CC-SNe) are the most extreme transients in the sky. In particular the CC-SNe are generally factories of black holes and Neutron Stars. A relativistic inner engine of such kind gives a unique outlook on potentially powerful emissions in gravitational waves [15]. The most energetic events probably derive from central engines harboring rapidly rotating black holes, wherein accretion of fall-back matter down to the Inner Most Stable Circular Orbit (ISCO) offers a window to broadband extended gravitational-wave emission (BEGW). The Gravitational Wave template used for this injection is the ISCOchirpA

| Wave type | Mass (Sun) | Duration (s) | Frequency (Hz) |
|---|---|---|---|
| ISCOchirpA | 5 | 238 | 1049-2018 |

Finally we consider the magnetar morphology. We know that binary neutron star (NS) mergers are among the most promising sources of gravitational waves (GWs). Depending on the total initial mass of the system and the NS equation of state (EOS), the post-merger phase can be characterized by a prompt collapse to a black hole or by the formation of a supramassive NS, or even a stable NS. In the latter cases of post-merger NS (PMNS) formation, magnetic field amplification during the merger will produce a magnetar and induce a mass quadrupole moment in the newly formed NS. If the timescale for orthogonalization of the magnetic symmetry axis with the spin axis is smaller than the spindown time, the NS will radiate its spin down energy primarily via GWs. [11]. The template used for this waveform is the magXnetarD

| Wave type | epsilon | Duration (s) | Frequency (Hz) |
|---|---|---|---|
| magXnetarD | 0.005 | 400 | 1589-1900 |

As we see those Gravitational waves injected span a wide range of time, frequency and different morphologies. This will allow us to estimate the reconstructing capabilities of cWB pipeline.

The main parameters that cWB should be able to reconstruct are the source sky location and the main properties of the Gravitational Wave emitted. The most important estimates performed by cWB are then: $h_{rss}$, SNR, central frequency and source coordinates: those are the parameter reconstruction provided by the cWB analysis. In particular for the wave reconstruction we know that a Gravitational Wave is completely reconstructed when the time evolution of both polarization $h_+(t)$ and $h_x(t)$ are known. This is complicated because it requires the inverse solution of the likelihood equation. What cWB performs is the reconstruction of the signal at detectors. A usual measure of the Gravitational wave amplitude is the soot-

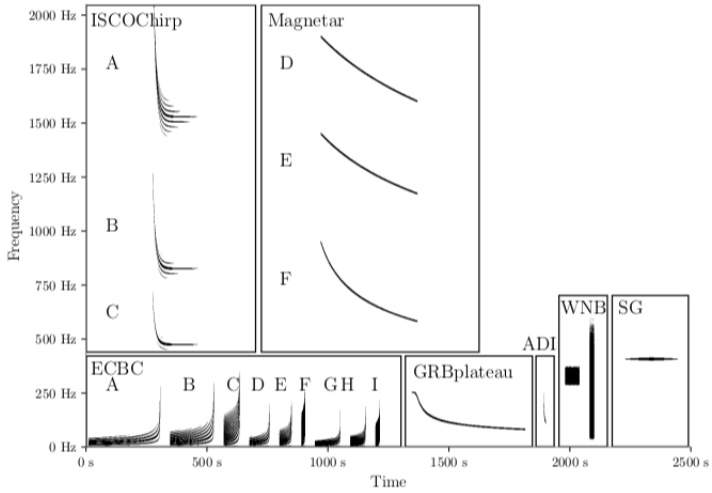


CM

**Figure 3.6:** Time-frequency spectrogram of the reference waveforms used in this search. We show examples of astrophysical waveforms such as postmerger magnetars (Magnetar) [11], black hole accretion disk instabilities (ADI) [12], newly formed magnetar powering a gamma-ray burst plateau (GRB plateau) [13], eccentric inspiral-merger-ringdown compact binary coalescence waveforms (ECBC) [14], broadband chirps from innermost stable circular orbit waves around rotating black holes (ISCO chirp) [15], and "ad hoc" waveforms,Ecband-limited white noise burst (WNB) and sine-Gaussian bursts (SG). The ISCO chirp waveforms have been shifted up in frequency by 50 Hz for readability. Durations range from 6 (ADI-B) to 470 s (GRB plateau). For reference see [16]

sum-square strain amplitude at the Earth $h_{rss}$:

$$h_{rss} = \sqrt{\int_{-\infty}^{\infty} (h_+^2(t) + h_x^2(t))dt} \tag{3.29}$$

To estimate the $h_{rss}$ at 50% detection efficiency we add simulated waveforms coherently to the detector's data, uniformly distributed in time and over sky locations. We define the detection efficiency as the number of candidate events that survive the thresholds used to discriminate the signals from the noise with respect to the total number of injected events. It is also required that the reconstructed signals fulfill the requirements to have a false alarm rate (ifar) lower than a chosen value [16]. The ifar is obtained by the statistical analysis of the background: once the pipeline have been applied to the various segments shifted as described in section 3.4, we obtain a list of unphysical signals: the glitches, so we can associate an alarm rate which tells us how many noise generated signal happen over a significant amount of time. The chosen value of ifar is 1/50 years.

Those signals have been chosen in order to have the widest example of morphologies in the TF plane that a Gravitational wave can show. Once the background is then statistically developed, we can proceed to the injection of the signals. The signals are produced using a built-in generator for creating simulated Burst-like signals or signals generated from coalescing binaries [38].

The Gravitational waves signal considered will cover a wide morphology space. As said above, this is useful since we can test the capability of cWB in reconstructing the signals considering different durations, frequency range, masses of the components and so on. For each waveform are injected around $\sim$ 5000 signals. For the injected waveform of AdiA and CM09short in the O3b configuration the number of injected signals is one order of magnitude more. Each signal is injected at 8 different distances, these cover a $h_{rss}$ from range from $2.5\text{x}10^{-22}1/\sqrt{\text{Hz}}$ to $6.7\text{x}10^{-21}1/\sqrt{\text{Hz}}$ . Also the injections are following an uniform distribution in sky position. The whole simulation, so the totality of waveforms regained from the pipeline for a specific Gravitational wave signal, will produce an efficiency plot and a set of graphs which includes the distribution of injected position and the reconstructed position or the histogram of injected signal and the regained one. As an example we report some graphs from the AdiA.

From Figure 3.9 we see that even if the signals are injected from uniformly distributed sky positions, the signals are forced to be reconstructed in accessible sky positions from the IFOs network, in particular the reconstructions are concentrated to the more accessible portions of the sky. In figure 3.10 instead we see that all the reconstructed signals show detection statistics $\rho > 10$, allowing us to get nearly half of the injected signals.

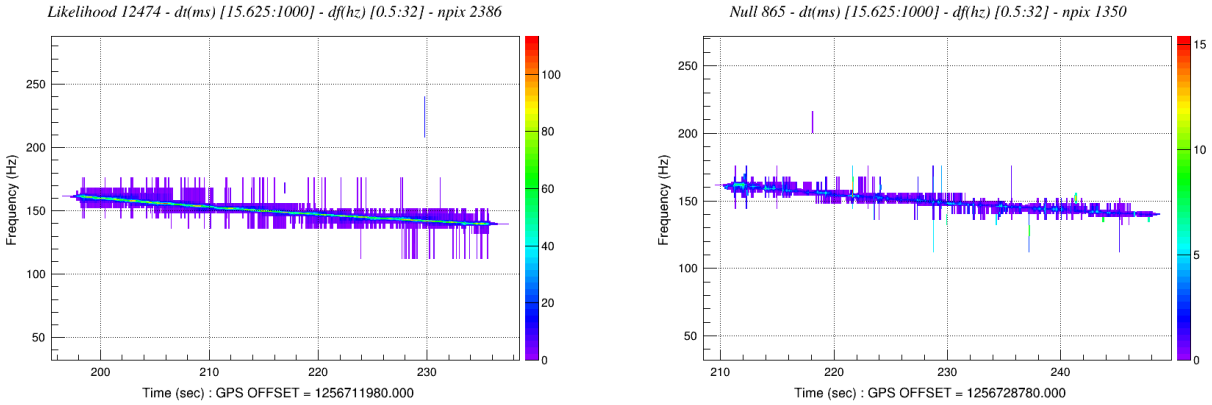


**Figure 3.7:** Example of single injection reconstruction of AdiA waveform. Likelihood obtained by cWB (left), Null (right)

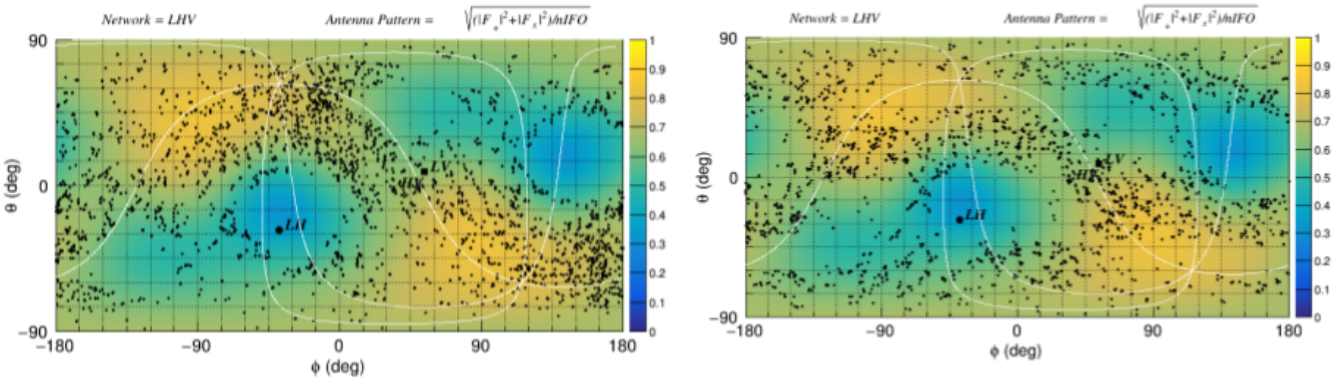


**Figure 3.8:** Injected (left) and reconstructed (right) signals position in the sky, using AdiA waveform in LHV configuration

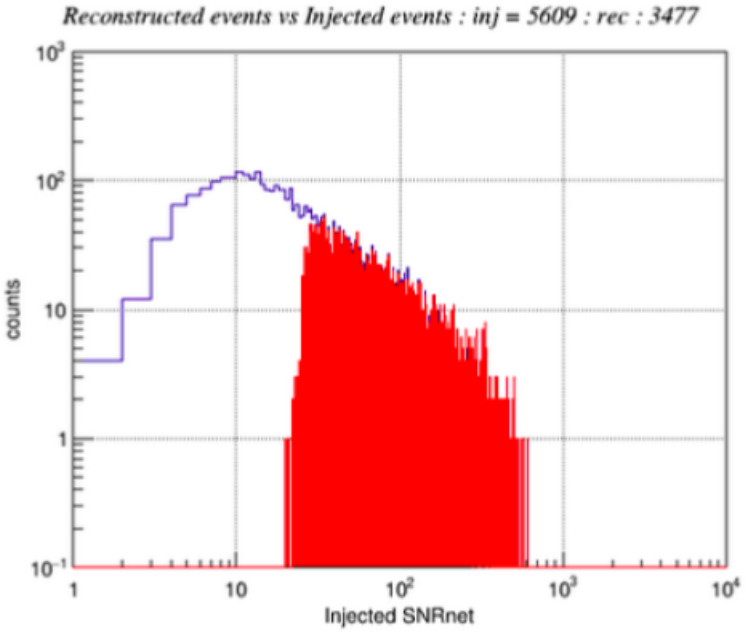


**Figure 3.9:** Number of injected (blue) and reconstructed (red) signals, using AdiA waveform in LHV configuration

# 4

# Detection efficiency and signal reconstruction of unmodeled long duration GW signal search.

The principal aim of this thesis is to estimate detection efficiency and reconstruction capability of the cwb pipeline for long duration GW signal search, considering both O3b , which correspond to the data taking performed by LIGO-Virgo collaboration from November 1st 2019 to March 27th 2020. The data can be accessed through the GWOSC database [39], and simulated O4 campaign of data analysis, foreseen to start in 2023. Firstly we characterize the background, studying expectation of its ranking statistic distribution and morphology features, e.g. frequency. Then we proceed by obtaining the efficiency of cWB through the simulation, with the method described in the previous chapter. Finally what will be studied is the statistical properties of the population of the injected signals, considering both O3b, O4, and O4 with a less strong constraints in the $\gamma$ parameter, which allows us to study the angular reconstruction of the source and see how the efficiency can vary within this parameter set.

## 4.1 Configuration for Long Duration Signal Search

Firstly we need to configure the cWB algorithm for this specific search; we start from the specific setting used in the O3 analysis for the LH network and report in [16]. We highlight that an important parameter has been modified in this analysis: the threshold that fixes the minimum coherent energy needed to clusterized the pixels has been lowered: the SubRho value, which is a lower-threshold for the clustering process. Every pixel with a $\rho >$ SubRho will be considered accountable for producing a cluster. Clusters with a value of the coherent energy below the threshold are discarded. This is done since in the Long Duration research the energy of an injected signal is spread in a much larger Time-Frequency volume with respect to other searches, causing the tendency to lower the energy of the reconstructed clusters. Lowering the SubRho value allows us to have a wider number of clusters which are candidates for the coherency analysis. The chosen value is SubRho $= 3.5$, which is lower than the one used in the O3b with LH configuration analysis that was SubRho $= 5$.

The data used are the one coming from the O3b campaign, from November 1st 2019 to March 27th 2022, for a total of 150 days [40]. The data strains are then divided in segments each of 1200s duration. We limited the analysis in a frequency range of 24 and 2048 Hz. In order to estimate the background expectations on the ranking statistic the cWB pipeline has been set introducing a non physical time shift delay of 2 sec, and then performing 600 time shifts for each time segment analyzed.

Then we have to set the production parameters.

- bpp: tells us the fraction of most energetic pixels selected from the TF map to construct events.
- $\rho$: defines that clusters are selected in the production stage if rho is bigger than this parameter.
- $c_c$: that clusters are selected in the production stage if rho is bigger than this parameter
- TGap and FGap: related to the maximum gaps between two different TF pixels at the same decomposition level that can be considered for the clusterization.
- $\gamma$: regulator that forces the reconstruction

In particular the $\gamma$ regulator is interesting. By modifying this parameter we can then reconstruct the source position of the signal in a more angular accurate way. Once these parameters are fixed, for a complete description see [9], we can proceed to evaluate background expectations. In table 4.1 we report the values of the parameters used in this analysis.

Once the triggers obtained from the background are produced, we can exert the vetoes and the cuts. The vetoes used apply the data quality in the post production phase, as said in section 3.3.3 [33]. The cuts are fundamental post production features: they are a set of requirements on the morphologies and features of the trigger to discriminate between signal and noise. The standard set of conditions, similar to the one applied in O3 analysis, is the the cut_1 and correspond to

cut_1

- mean frequency cuts: $>$ 24Hz and $<$ 2048Hz

| production parameters | |
|---|---|
| bpp | 0.001 |
| $\rho$ | 5.0 |
| $c_c$ | 0.5 |
| TGap | 2.0 |
| FGap | 32.0 |
| $\gamma$ | -1.0 |

**Table 4.1:** Values of parameters chosen for the analysis.

- $c_c$ cuts: $> 0.6$
- duration: $> 1.5$s

Where frequency and duration must be intended as central frequencies of the event computed from the reconstructed waveform and energy weighted bandwidth estimated in time/freq domain for all resolutions bandwidth.

## 4.2 O3b data taking, LH network interferomenters

Before proceeding with the O3b - LHV configuration, we have performed a reanalysis with LH configuration. This is due in order to verify the correctness of the parameters used in the production phase and the cuts in post-production.

An important parameter is the observation time analyzed, which correspond to the total amount of time simulates using the lags, we have for LH

| Observation Time Analyzed (LH) | 149.6y |
|---|---|

We report the result of the background characterization. We can start from these two graphs (Figure 4.1) that represent the $\rho$ ranking statistics reporting coherent energy values as function of the frequency. The bigger the $\rho$ is, the deeper the background is affected by glitches events. We want in fact to have this parameter as low as possible since it identifies the effective correlated SNR that a signal must have in order to overcome the noise and be detectable in a reasonable statistical confidence.

**Figure 4.1:** Background characterization, rho values vs frequency [Hz]. LH configuration. cut_1 threshold (left), cut_2 threshold (right)

It is interesting now analyze the background. In fact we know that by construction, the triggers obtained by cWB are all un-physical signals. In order to show that, we can study the morphology of these. Let's consider the following example: in

the LH background characterization there is a selected event with $\rho = 31.9$ and frequency $\sim 30$Hz, see figure 4.2. If we now study the morphology of this event, it immediately results in his glitch nature.

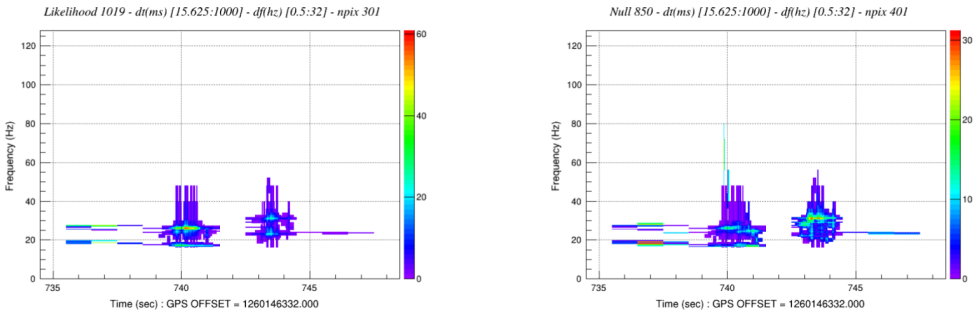


**Figure 4.2:** Example of glitches morphology obtained from background analysis of LH. Likelihood (left), Null (right)

It is clear that this likelihood is not related to any of the considered morphology of the signal tested in this work. This is due to the noise source affecting the LIGO network at 32Hz [41]. The presence of highly noisy events in the low frequency band will force us to define another cut with respect to the cut_1 defined above. So using a cut in 40Hz we can easily eliminate those glitches that deeply affect the background. So we define the cut_2:

- frequency cuts: $>$ 40Hz and $<$ 2048Hz
- netCC cuts: $> 0.6$
- duration: $>$ 1.5s

As we see for LH network the cut_2 is less affected by loud events related to glitches, this means that the same $\rho$ value obtained for a trigger has different significance statistics from cut_1 to cut_2. Another important statistical evaluation is the number of events as a function of $\rho$. This graph, Figure 4.3, describes the population of events as a function of coherent energy. As we see the great majority of glitches events show a coherent energy $\rho < 10$.

Then the inverse false alarm rate, Figure 4.3. This is a noticeable value since it guarantees a statistical confidence in our false alarm detection.

It is interesting to notice that in the right graph, which corresponds to the cut_2, we see that a false alarm with $\rho \sim 10$ is detected every 100 years, while for the cut_1 the same ifar is obtained for $\rho \sim 20$. This means that reducing the background noise in the range $20 - 40$Hz affects positively the detection efficiency as we will see in the next paragraphs.

## 4.3 O3b data taking, LHV network interferomenters

For the LHV network the parameters are similar. The main difference is due to the presence of Virgo strain sensibility curve, which is higher than Ligo as mentioned in section 3.3.8. The total observation time simulated for LHV is

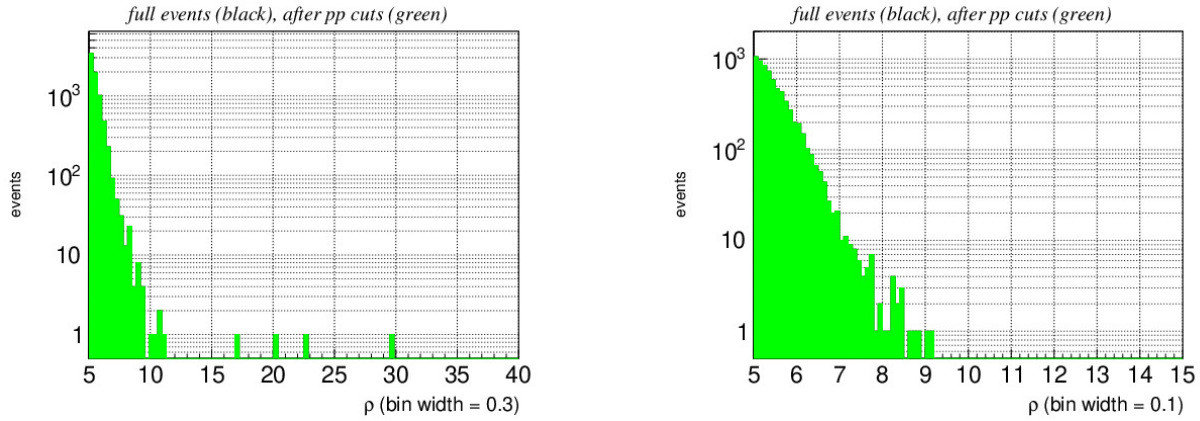


**Figure 4.3:** Background characterization: number of background events associated to a certain value of ρ. cut_1 threshold (left), cut_2 threshold (right)

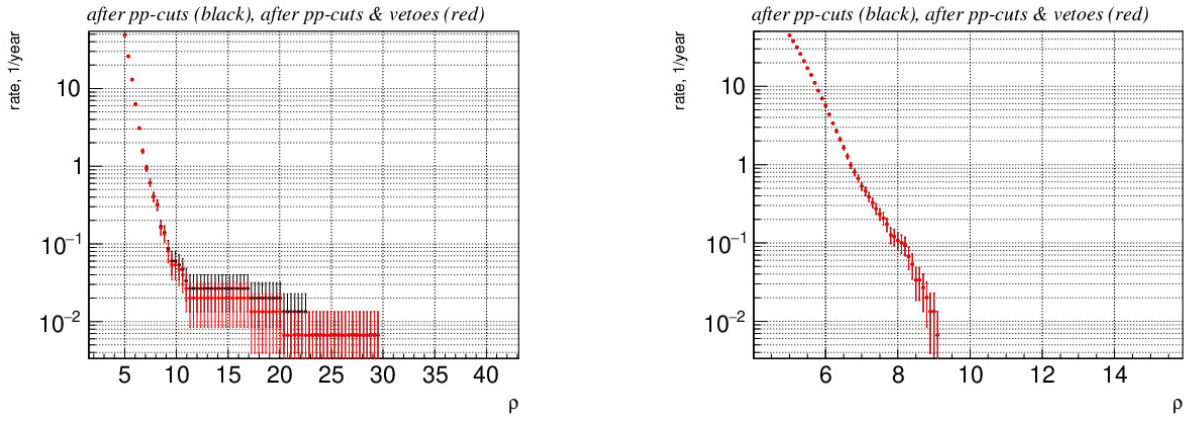


**Figure 4.4:** Background estimation: Inverse False alarm rate as function of the rho. LH configuration. cut_1 threshold (left), cut_2 threshold (right)

| Observation Time Analyzed (LHV) | 105.4y |
|---|---|

As we see in the LHV configuration there is still a prominent presence of noise in the lower frequency, up to 40Hz and even above, Figure 4.5 and 4.6. But with respect to the LH configuration here the glitches do not pass the value of $\rho = 15$, and in the cut_2 we have glitches under $\rho = 10$.

## 4.4 O3b data taking, LH and LHV network Efficiency

As we said from the background analysis the fundamental parameter is the false alarm rate. Once this parameter has been estimated, we can proceed in the injection of the Gravitational Waveforms. As mentioned above, the waveforms selected meet

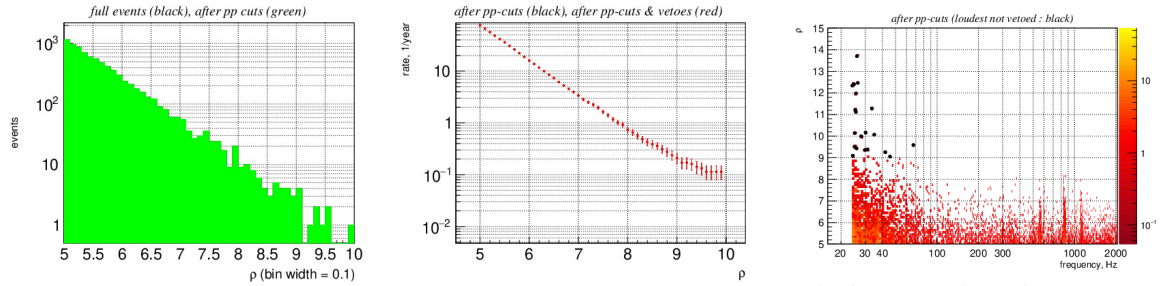


**Figure 4.5:** Background estimation: LHV network, cut_1 threshold. Number of Events and ρ (left). ifar and ρ (center), ρ and frequency (right).

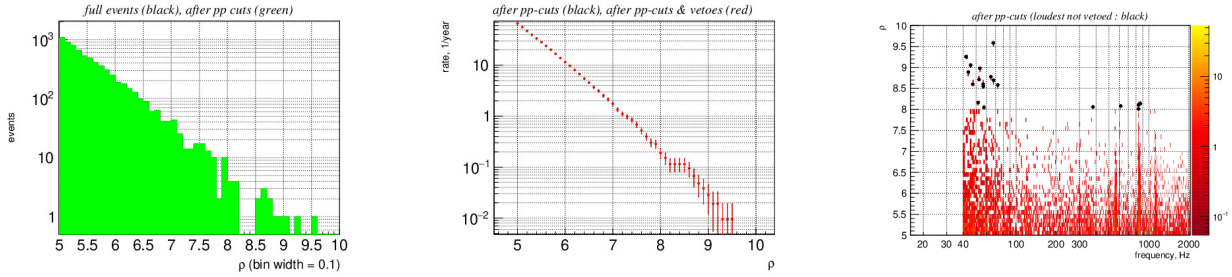


**Figure 4.6:** Background estimation: LHV network, cut_2 threshold. Number of Events and ρ (left). ifar and ρ (center), ρ and frequency (right).

our need to test different morphologies. For the detection efficiency we choose the AdiA, CM09short and NCSACAM_F waveforms, which cover a wide spectrum of morphology, duration of the signal and frequency range. The strain factors used for LH and LHV cover a range from $1.56\text{x}10^{-22}$ to $1.72\text{x}10^{-20}(1/\sqrt{\text{Hz}})$. for each injection in this range the strain factor is scaled by a factor of 1.6 in order to simulate 8 different distances of the source sky position and to obtain the efficiency curve. For each of those factors the efficiency has been evaluated. We define the efficiency as the $h_{rss}$ (3.30) associated to the percentage of correctly reconstructed injected signals. In particular we consider the $h_{rss}(50\%)$ detection efficiency, which means the value of $h_{rss}$ at which 50% of the injected signals are reconstructed and recognized as GW signals. In order to do so, during the post production phase various merging options, vetoes and cuts are applied. In particular for correctness of efficiency calculation, for each injected signal we forced the pipeline to select between the various triggers the most energetic one, assuming it to be the whole reconstructed signal. This is due to the fact that the signal's energy is spread over a huge Time-Frequency volume, so the pipeline is not capable of reconstructing the signal as a whole, rather it will be divided in segments really close to each other. This of course means a loss in information in how the pipeline reconstructs the signal, but allows us to have a consistent parameter which describes the efficiency. The efficiency has been estimated for both sets of possible selection cuts as those applied to the background. The ifar value selected is T_ifar $= 50$. With the value T_ifar $= 50$ we select the events with a value of ρ superior to the one corresponding to have a false alarm caused by a glitch event with the same ρ every fifty years. The efficiency values obtained for $h_{rss}(50\%)$ in LH network configuration is reported in table 4.2. Those analyses have been performed in order to guarantee the consistency of the configuration of the pipeline used in this

| Waveform (LH) | $h_{rss}(50\%)$ with cut_1 | $h_{rss}(50\%)$ with cut_2 |
|---|---|---|
| AdiA | $3.50x10^{-22}$ | $2.81x10^{-22}$ |
| CM09short | $7.06x10^{-22}$ | $6.17x10^{-22}$ |
| NCSACAM_F | $1.20x10^{-21}$ | $1.20x10^{-21}$ |

**Table 4.2:** $h_{rss}(50\%)$ detection efficiency for O3b - LH configuration

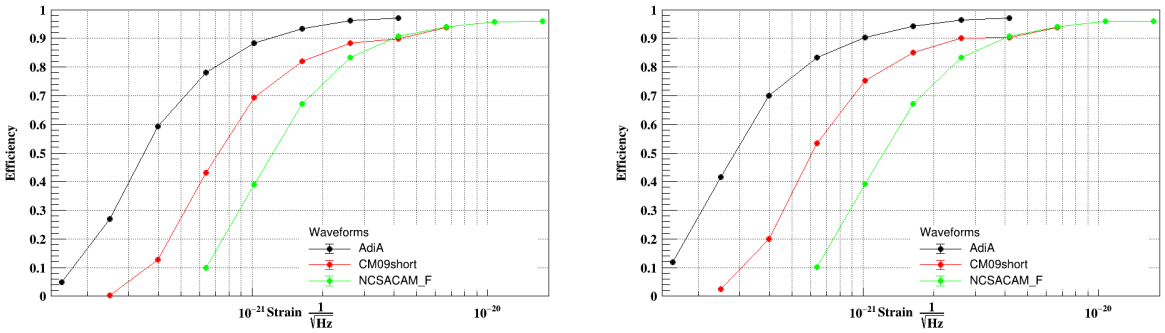


**Figure 4.7:** $h_{rss}$ detection efficiency for AdiA (blue), CM09short (red), NCSACAM_F (green). Left cut_1, right cut_2. LH network, O3b configuration. The points identify the different distances at which the signals have been injected.

work with respect to the one used in the O3b analysis [16].

The LHV network present a completely similar procedure, so the efficiency values are reported in Table 4.3

| Waveform (LHV) | $h_{rss}(50\%)$ with cut_1 | $h_{rss}(50\%)$ with cut_2 |
|---|---|---|
| AdiA | $3.07x10^{-22}$ | $2.81x10^{-22}$ |
| CM09short | $6.46x10^{-22}$ | $6.02x10^{-22}$ |
| NCSACAM_F | $1.16x10^{-21}$ | $1.16x10^{-21}$ |

**Table 4.3:** $h_{rss}(50\%)$ detection efficiency for O3b data - LHV configuration

As we see, considering the LHV network does not dramatically change the values for the efficiency in the injected waveform. The introduction of Virgo will allow us a better reconstruction of the signal origin: as we see in Figure 4.8 in the LHV configuration there is a wider portion of the sky accessible for detecting the Gravitational Wave.

## 4.5 Efficiency Analysis - O4 and $\gamma$ constraint

At this point we can study the efficiency of our pipeline in the O4 strain sensitivity, also considering a softer constraint in the $\gamma$, which should improve the reconstruction of the signal source localization. The strain sensitivity curve has been obtained

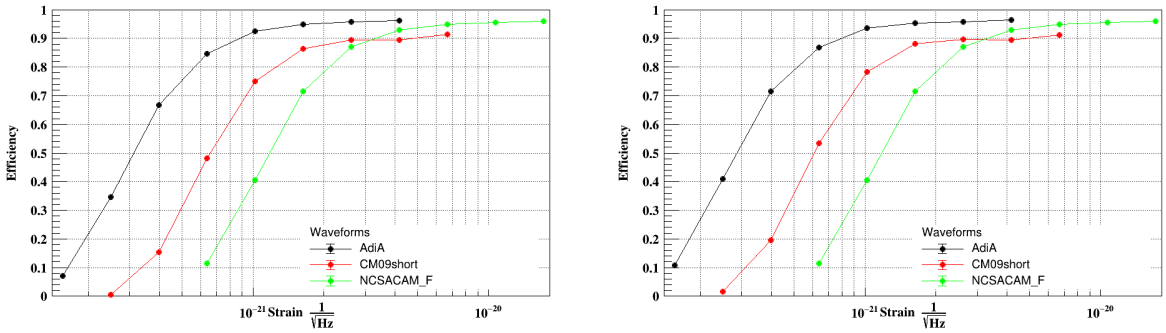


**Figure 4.8:** $h_{rss}$ detection efficiency curves for AdiA (blue), CM09short (red), NCSACAM_F (green). Left cut_1, right cut_2. LHV network, O3b configuration. The points identify different distances at which the signal have been injected.

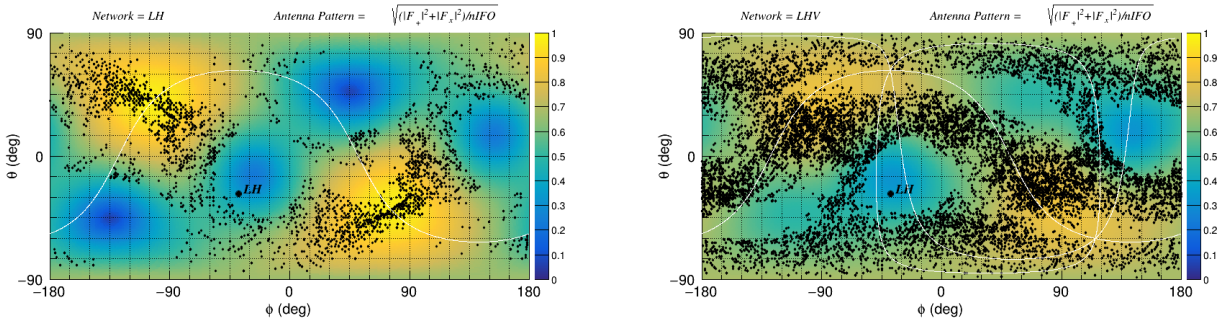


**Figure 4.9:** Reconstructed position in the sky for LH configuration (left) and LHV (right).

by scaling the strain sensitivity curve of O3b by a factor, specific for each IFO, that will simulate the attended strain sensitivity. The scaling factors simulate a strain 190Mparsec for Livingstone-Hanford and 120Mparsec for Virgo. For future work see [42]. For this analysis we have decided not to use a simulated Gaussian background with that strain since in this kind of research the biggest problem is to handle the glitches. So we choose to use the strain provided by the background data scaled by different factors for each detector. The strain factors used for the injection are selected in such a way that guarantee the same behaviour of the efficiency as studied for the O3b case. The range of injections have been performed from $6.1\text{x}10^{-23}1/\sqrt{\text{Hz}}$ to $6.7\text{x}10^{-21}1/\sqrt{\text{Hz}}$. As for O3b, we have considered 8 distances for the injections.

Another feature of this analysis is considering a different value for the $\gamma$ constraint. We said that this parameter forces the reconstruction of the injected signal to consider a single one polarisation. Now we will relax this parameter and see if there will be a difference in the efficiency and sky position reconstruction performed by cWB. As above we proceed by the background characterization and then to the detection efficiency. The $\gamma$ value is shifted from $-1.0$ to $-0.5$. The total amount of time simulated of O4 and O4 - $\gamma$ configuration is the same as the one of O3b in LHV configuration [29].

We see how applying the scaling factors we get a different strain for the O4 configuration with respect to the O3b configuration.

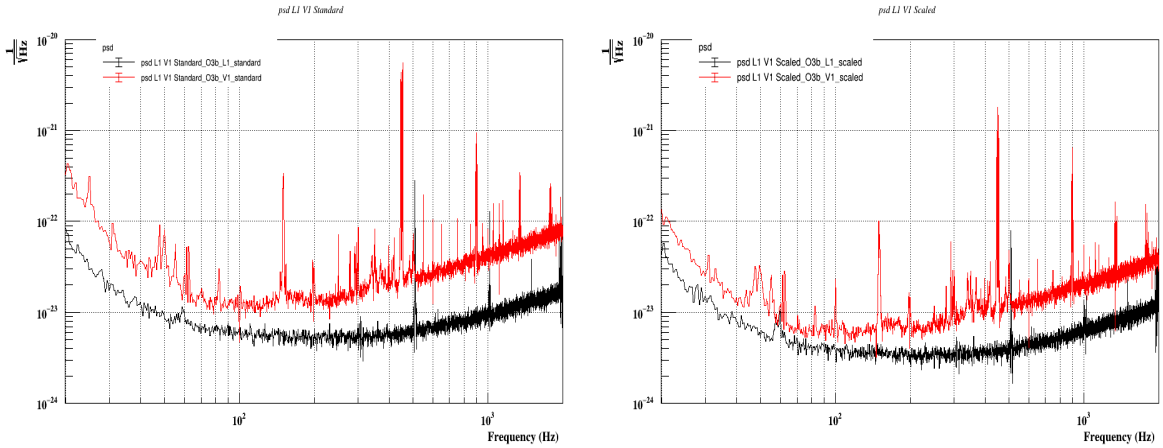


**Figure 4.10:** Comparison between O3b and O4 Strain Sensitivity. PSD for L and V in the O3b configuration (left). PSD for L and V in O4 configuration.

### 4.5.1 O4 and O4 - γ background analysis

We can now proceed in analyse the background considering both O4 and O4 - γ configurations for LHV with cut_1 and cut_2. The results are reported in Figures 4.11 - 4.14.

As we see usually the O4-γ constraint shows a moderate less noisy behaviour, especially in the cut_2, as the ifar graph shows in Figure 4.14. Both the configuration, O4 and O4-γ exhibit a significant reduction of the inverse false alarm rate passing from cut_1 to cut_2: at least one order of magnitude. The curve in Figure 4.15 represents the complete distribution of events rate as function of ρ considering the whole tail. Notice that here the rate is in [Hz]. This curves manifest a peculiar behaviour for the O4 - γ configuration, which should be interesting to go into detail.

### 4.5.2 O4 and O4 - γ Efficiency Analysis

As done for the O3b configuration, also the evaluation of the efficiency for both O4 and o4-γ have been performed. As we see from tables 4.4 and 4.5 the O4 configuration shows a slightly better performative efficiency with respect to O4 - γ. It is noticeable that in the O4 - γ configuration the $h_{rss}(50\%)$ related to the cut_1 is worse than the one evaluated in _2. This may be due to the different background statistics which affects the reconstruction of the injected waveform. We have the biggest variation in AdiA O4 - γ configuration passing from cut_1 to cut_2.

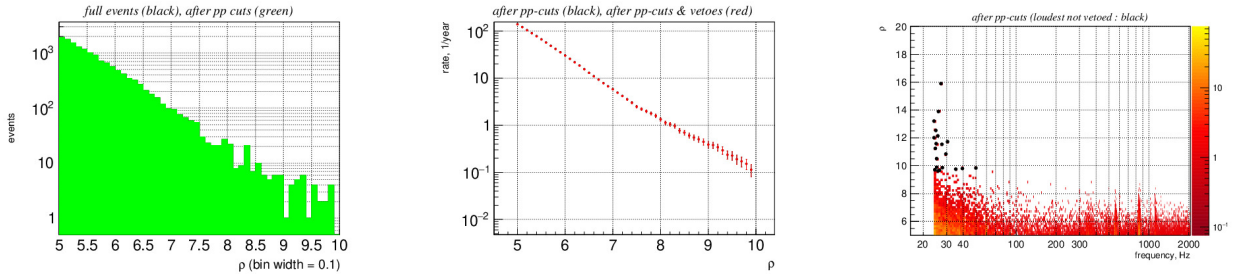


**Figure 4.11:** Number of Events as function of ρ (left), ifar: rate of events distribution as function of ρ (center), ρ vs frequency (right).LHV network with O4 strain sensitivity with cut_1.

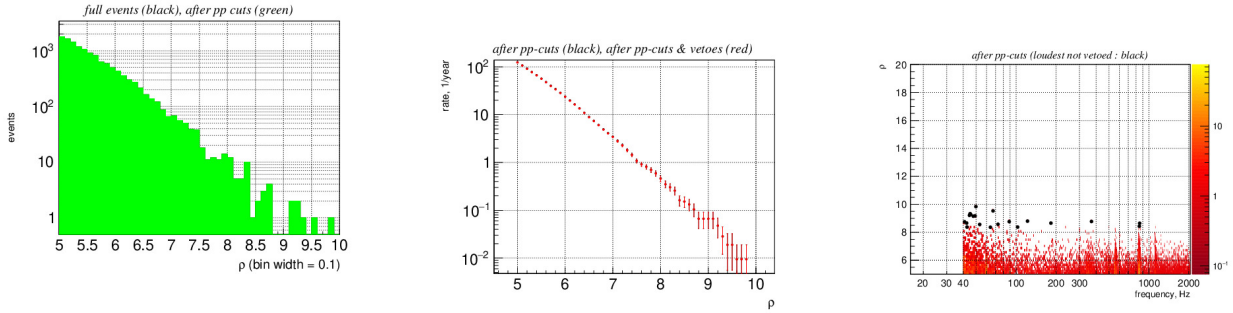


**Figure 4.12:** Number of Events as function of ρ (left), ifar: rate of events distribution as function of ρ (center), ρ vs frequency (right). LHV network with O4 strain sensitivity with cut_2.

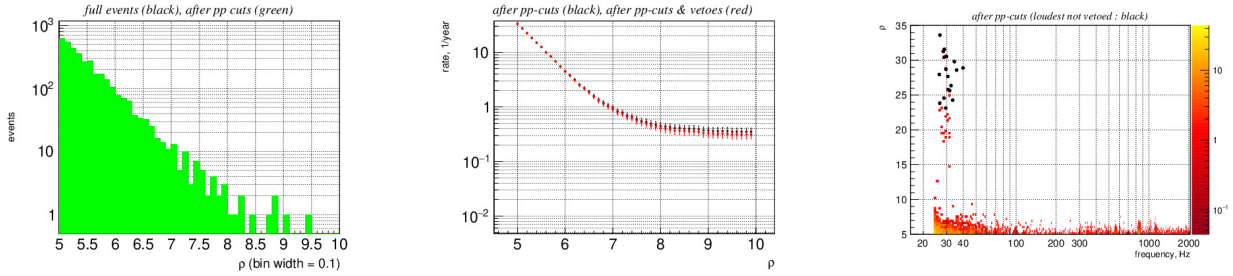


**Figure 4.13:** Number of Events as function of ρ (left), ifar: rate of events distribution as function of ρ (center), ρ vs frequency (right). LHV network with O4 strain sensitivity and γ constraint with cut_1.

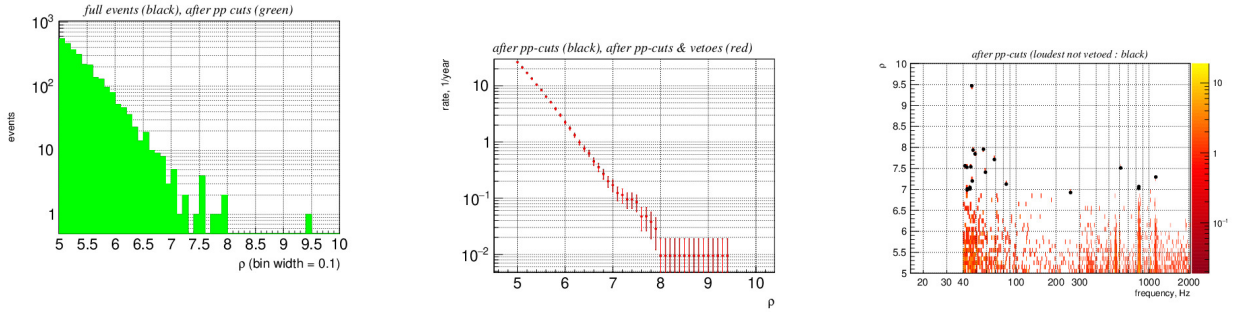


**Figure 4.14:** Number of Events as function of ρ (left), ifar: rate of events distribution as function of ρ (center), ρ vs frequency (right). LHV network with O4 strain sensitivity and γ constraint with cut_2.

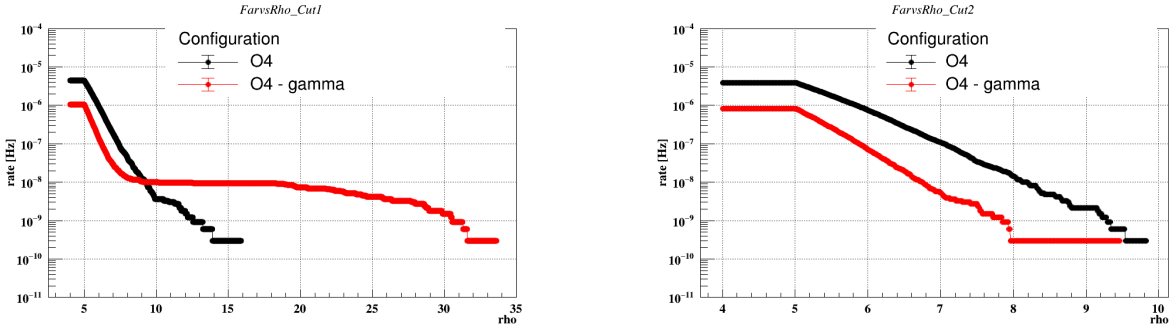


**Figure 4.15:** ifar distribution, in red O4 - $\gamma$ configuration, in blue O4 configuration, cut_1 (left). ifar distribution, in red O4 - $\gamma$ configuration, in blue O4 configuration (right), cut_2.

| Waveform (LHV - O4) | $h_{rss}(50\%)$ cut_1 | $h_{rss}(50\%)$ cut_2 |
|---|---|---|
| AdiA | $1.97x10^{-22}$ | $1.00x10^{-22}$ |
| CM09short | $4.13x10^{-22}$ | $3.83x10^{-22}$ |
| NCSACAM_F | $7.27x10^{-22}$ | $7.27x10^{-22}$ |
| NCSACAM_B | / | $4.84x10^{-22}$ |
| ISCOchirpA | / | $9.80x10^{-22}$ |
| magXnetarD | / | $2.10x10^{-21}$ |

**Table 4.4:** $h_{rss}(50\%)$ detection efficiency for O4 configuration

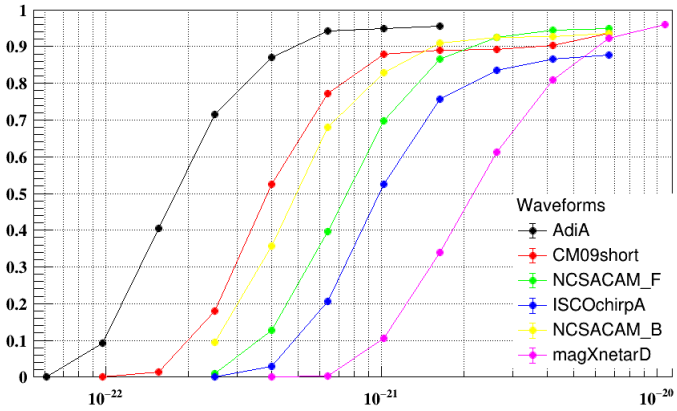


**Figure 4.16:** $h_{rss}$ detection efficiency for O4 configuration with cut_2. On y axis is reported the efficiency, on x axis the strain values $[1/\sqrt{Hz}]$. Adia (black), CM09short (red), NCSACAM_F (green), ISCOchirpA (blue), NCSACAM_B (yellow) and magXnetarD (purple) waevorms injected. The points represent the different distances at which the signals have been injected.

| Waveform (LHV - O4-$\gamma$) | $h_{rss}(50\%)$ cut_1 | $h_{rss}(50\%)$ cut_2 |
|---|---|---|
| AdiA | $4.11\text{x}10^{-22}$ | $1.81\text{x}10^{-22}$ |
| CM09short | $6.06\text{x}10^{-22}$ | $3.93\text{x}10^{-22}$ |
| NCSACAM_F | $7.63\text{x}10^{-22}$ | $7.24\text{x}10^{-22}$ |

**Table 4.5:** $h_{rss}(50\%)$ detection efficiency for O4 - $\gamma$ configuration

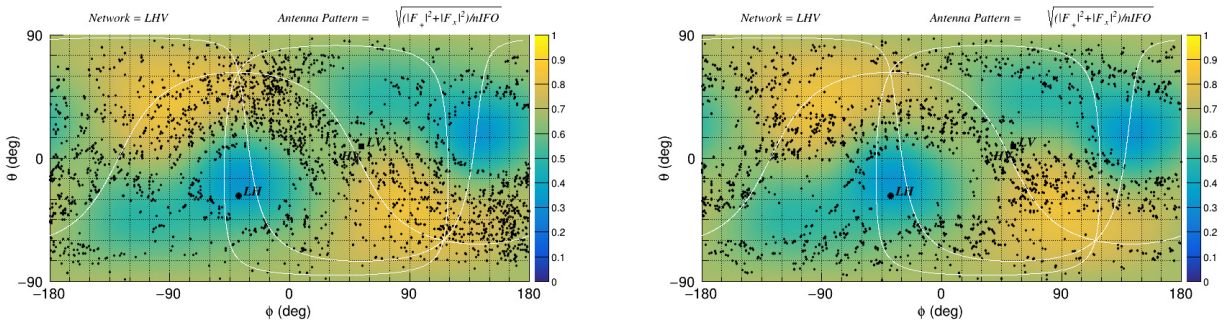


**Figure 4.17:** Reconstructed positions of injected signals. O4 - $\gamma$ configuration (left) O4 configuration (right), cut_2.

### 4.5.3 Angular distribution, O4 and O4 - $\gamma$

What now is a matter of interest is to study the angular distribution of reconstructed events both for O4 and O4-$\gamma$ configuration.

We know that the position in the sky is defined by the two angles $\theta$ and $\varphi$, respectively the right ascension and the declination, so to estimate how the sky position is reconstructed, we plot the difference between the injected angles and the rebuilt angles of the triggers. So we plot in Figure 4.18 and 4.19 the percentage of events with a reconstructed and injected angles, respectively phi and theta, that diverges less than a fixed value, as a function of it. This is done for both $\theta$ and $\varphi$ and configurations. For this analysis we considered just the cut_2 since it is the most performative.

In order to have a better visualization of the difference in reconstructing by the different configurations, a Gaussian plot around the peak has been performed. The interval considered is $(-10, 10)$ degree. In the Tables 4.6 and 4.7 are reported the results of this fit for the considered configurations in cut_2.

As we see in the O4-$\gamma$ configuration, considering image 4.20, there is a better reconstruction of the source position, as the width of the angle difference curves suggests. These tables are useful to have an idea of how well softening the constraints helps us in obtaining a better sky-position in the reconstruction phase by the pipeline.

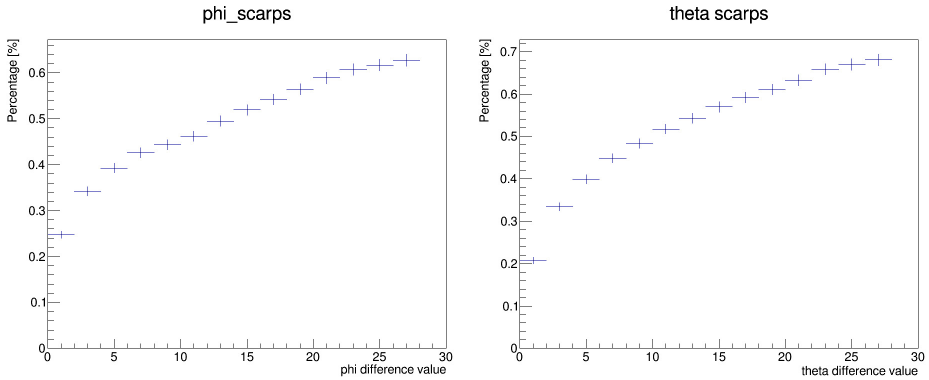


**Figure 4.18:** Cumulative frequency of the difference in $\varphi$ angle (left). Cumulative frequency of the difference in $\theta$ angle. AdiA Waveform with cut_2, O4 - $\gamma$ configuration

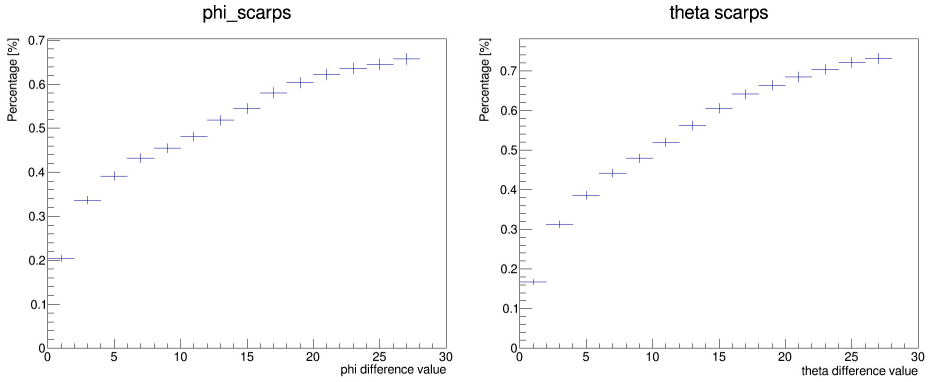


**Figure 4.19:** Difference between the injected angular $\varphi$ and the rebuilt one (left). Difference between the injected angle $\theta$ and the rebuilt one (right). AdiA Waveform with cut_2, O4 configuration

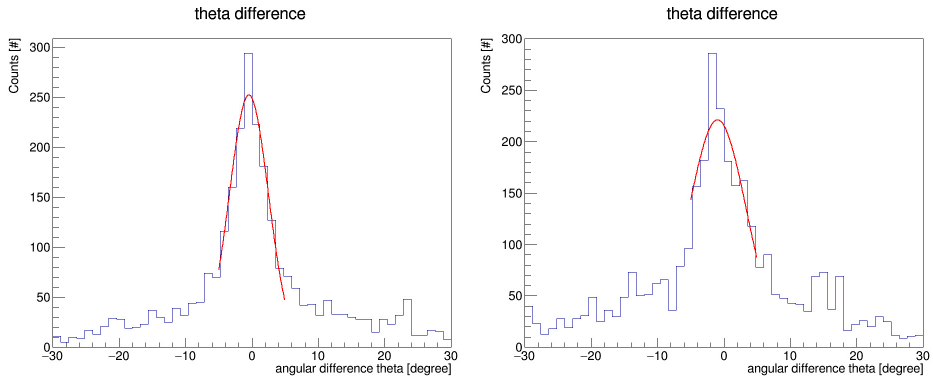


**Figure 4.20:** $\theta$ angle differences between injected and reconstructed distribution for O4 - $\gamma$ configuration (left). $\theta$ angle differences between injected and reconstructed distribution for O4 configuration (right). AdiA Waveform

| Gaussian Fit $\varphi$ angle - O4 - cut_2 | | | |
|---|---|---|---|
| Fit values | AdiA | CM09short | NCSCACAM_F |
| Mean | $3.4x10^{-1}$ | $1.4x10^{-1}$ | $3.2x10^{-1}$ |
| $\sigma$ | 3.4 | 3.3 | 3.2 |
| Gaussian Fit $\theta$ angle - O4 - bin2_cut | | | |
| Fit Values | AdiA | CM09short | NCSCACAM_F |
| Mean | $-2.7x10^{-1}$ | $1.4x10^{-1}$ | $3.2x10^{-1}$ |
| $\sigma$ | 3.4 | 3.3 | 4.4 |

**Table 4.6:** difference between injected and reconstructed angle Gaussian Fit for O4 configuration

| Gaussian Fit $\varphi$ angle. - O4 $\gamma$ - cut_2 | | | |
|---|---|---|---|
| Fit values | AdiA | CM09short | NCSCACAM_F |
| Mean | $-3.7x10^{-1}$ | $-1.4x10^{-1}$ | $-1.5x10^{-1}$ |
| $\sigma$ | 3.3 | 2.4 | 2.6 |
| Gaussian Fit $\theta$ angle- O4 $\gamma$ - cut_2 | | | |
| Fit Values | AdiA | CM09short | NCSCACAM_F |
| Mean | $-3.7x10^{-10}$ | $1.3x10^{-1}$ | $2.1x10^{-1}$ |
| $\sigma$ | 4.4 | 3.2 | 3.2 |

**Table 4.7:** Difference between injected and reconstructed angle Gaussian Fit for O4 - $\gamma$ configuration

### 4.5.4 Analysis of the reconstruction process

One of the most critical points of the pipeline is the capability in reconstructing correctly the injected signals. Given the background and applying the cuts in order to select the highest valuable trigger candidates, we obtain the efficiency of the pipeline.

As mentioned above,the Long Duration injected signals will be clusterized in several pieces due to the wide volume in T-F the energy of the injected signal is spread in. Even if we low the threshold for creating the cluster this behaviour is still happening. So far we have studied the cases of O3b, O4 and O4-$\gamma$ configuration. The injected signals are not entirely reconstructed, rather they are broken in several segments, each one with a specific duration, $\rho$ etc. In the previous analysis we have considered just the most energetic segment of the injected signal in the post production phase for computing the $h_{rss}(50\%)$ detecting efficiency. Now we want to analyse the capability of the algorithm in reconstructing the signal by studying the statistical properties of the triggers for the morphologies considered so far. We can now introduce the concept of multiplicity. Given a reconstructed signal divided in N segments, we define the multiplicity "M" as the number N of segments for each signal. Each of those segments have a set of parameters such as length, $\rho$, time of injection and so on. In order to study the multiplicity and the properties of each segment we have developed specific codes to analyze these triggers.

A particular effort has been made in order to guarantee an efficient run-time analysis: to have the algorithm time of the

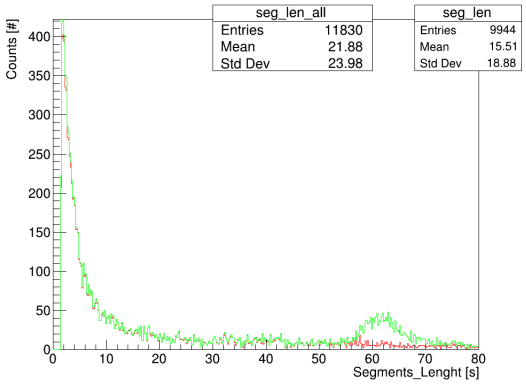


**Figure 4.21:** Lengths population: in green the distribution of lengths of segments with cut_2. In red the population with the cut also for $\rho < 100$.

order of O(n) the code has been implemented taking care of few but fundamental things. Firstly the data of the trigger have been sorted by time. This has been done since the segments have the same injection time. So sorting by time the list of triggers we can directly analyze the segments and regain the injected signal. This has the cost in complexity of algorithm, but the time saving due to this feature is well pay-back. Once the data have been sorted by time, our aim is to correctly rebuild the signal, unifying the segments by their injection time. This for each injection factor (i.d. the energy). Then finally we have a data pack for each injection which tells us the multiplicity of the reconstructed signal, the energy and duration of each segment and provides us a useful structure for data analysis. Our main interest is to characterise the multiplicity of each morphology. So we are interested in two results: the multiplicity distribution with respect to the energy and the distribution of the energy of the segments. For this analysis we have considered all the data sets, O3b, O4 and O4-$\gamma$. The chosen waveforms for this analysis are the AdiA, the CM09short and the NCSACAM_F. This choice has been made since, as mentioned above, those signals cover a huge spectrum of the Time-Frequency plane and show quite different morphologies. In fact, while the NCSACAM_F is really "short" in time (around $\sim$ 16s) for the type of analysis we are performing, the CM09short requires a huge amount of time ($\sim$ 470s), which results in widespread of energy in the Time-Frequency plane, causing clusterization.

Each data set had required the cuts defined above: cut_1 and cut_2, in particular for the O4 and for the O4-$\gamma$ we also put a cut in energies considering $\rho < 100$. This is due to the presence of a peak in population of segments with length around $55 - 70$s, as we see in figure 4.19.

In the tables 4.8, 4.9, 4.10 we report the statistics of multiplicity analysis

For Total Events we consider the triggers obtained by the pipeline in reconstructing the signals. The value "M" is the value of multiplicity as defined above. We see that the waveform which presents the most interesting statistical case is the

| Multiplicity Analysis - O3b - cut_2 | | | |
|---|---|---|---|
| Number of Events | AdiA | CM09short | NCSCACAM_F |
| Total Events | 29684 | 26539 | 28709 |
| with $M = 1$ | 27250 | 10211 | 28706 |
| with $M > 1$ | 2434 | 16328 | 3 |

**Table 4.8:** Multiplicity analysis for O3b configuration.

| Multiplicity Analysis - O4 - cut_2 | | | |
|---|---|---|---|
| Number of Events | AdiA | CM09short | NCSCACAM_F |
| Total Events | 3627 | 4463 | 3475 |
| with $M = 1$ | 3249 | 1886 | 3474 |
| with $M > 1$ | 378 | 2577 | 1 |

**Table 4.9:** Multiplicity analysis for O4 configuration

| Multiplicity Analysis - $\gamma$ - cut_2 | | | |
|---|---|---|---|
| Number of Events | AdiA | CM09short | NCSCACAM_F |
| Total Events | 3857 | 3064 | 3540 |
| with $M = 1$ | 3058 | 813 | 3540 |
| with $M > 1$ | 799 | 2251 | 0 |

**Table 4.10:** Multiplicity Analysis for O4 - $\gamma$ configuration

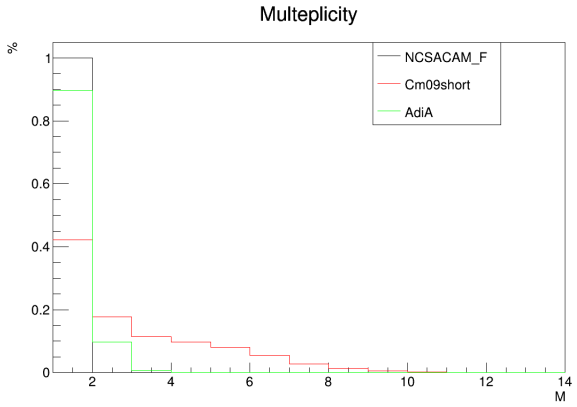


**Figure 4.22:** Percentage of events with respect to the Multiplicity. AdiA (green), CM09shot (red) and NCSACAM_F (black) waveforms with cut_1.

CM09short, while the NCSACAM_F barely shows multiplicity. This result is also reported in Figure 4.22. Here we can clearly see that the morphology mostly affected by the segmentation process is the CM09short, reasonably since its duration is reflected in a huge Time-Frequency volume.

We studied more deeply the interesting case of the morphology related to the CM09short in O3b, O4 and O4 - $\gamma$ configurations, considering different cuts for each configuration. The main idea is to evaluate, even in a phenomenological way, if given the O4 strain then we payback in more segmentation of the signal, obtaining an analogous efficiency for O3b and O4. Firstly we report the CM09short results for O3b.

In Figure 4.23, we report the following results. In the first graph the reconstructed signals have been binned in samples of $\rho = 2$. For each bin we calculate the average of multiplicity of all the data within the interval. The result is shown in the top left figure of image 4.23, where it is reported the average multiplicity values vs the $\rho_{max}$, where $\rho_{max}$ is the maximum value of $\rho$ among the segments of the reconstructed signal. For the second graph instead we compute the Energy Ratio (ER) defined as

$$ER = \frac{\rho_{max}}{\sum_{i \in C} \rho_i} x100 \tag{4.1}$$

$\rho_i$ is the value of $\rho$ associated to the $i^{th}$ segment of the trigger. C is the set of segments of the reconstructed signal. Clearly ER must be considered as a percentage. So once the ER is calculated for each segment in the considered bin interval, we perform an average over these values. The result is shown in the top right graph of Figure 4.23, where the ER vs the $\rho_{max}$ is described. In the bottom graph of image 4.23 the data have been binned with respect to M and considering only the reconstructed signals with $M > 1$, in each interval we computed the ER average, obtaining ER vs Multiplicity.

Referring to image 4.23, we see there is no clear relation between the energy of and the multiplicity. In particular from the first graph we see that the segmentation process happening in the pipeline is random, there is no correlation between

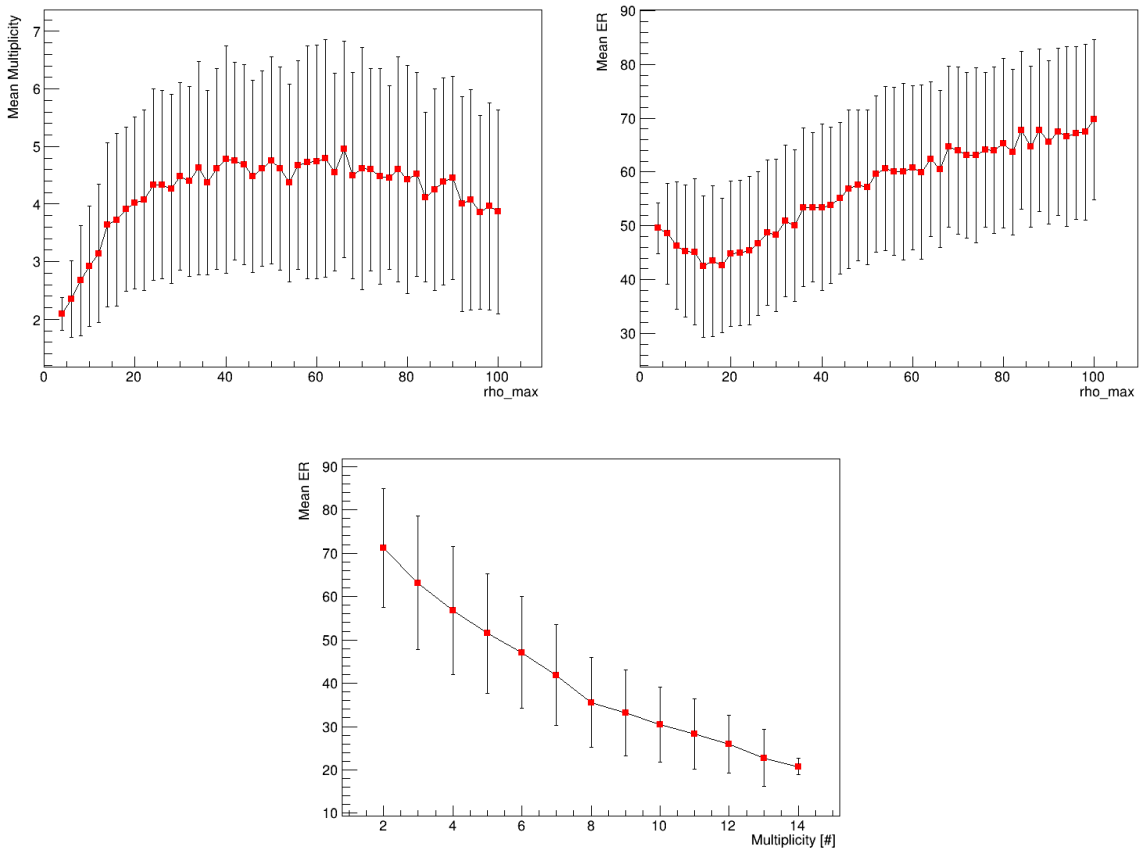


**Figure 4.23:** Mean M vs $\rho_{max}$ (top left), Mean ER vs $\rho_{max}$ (top right), Mean ER vs $\rho_{max}$ (bottom). Multiplicity Analysis of CM09short waveform in O3b configuration cut_2.

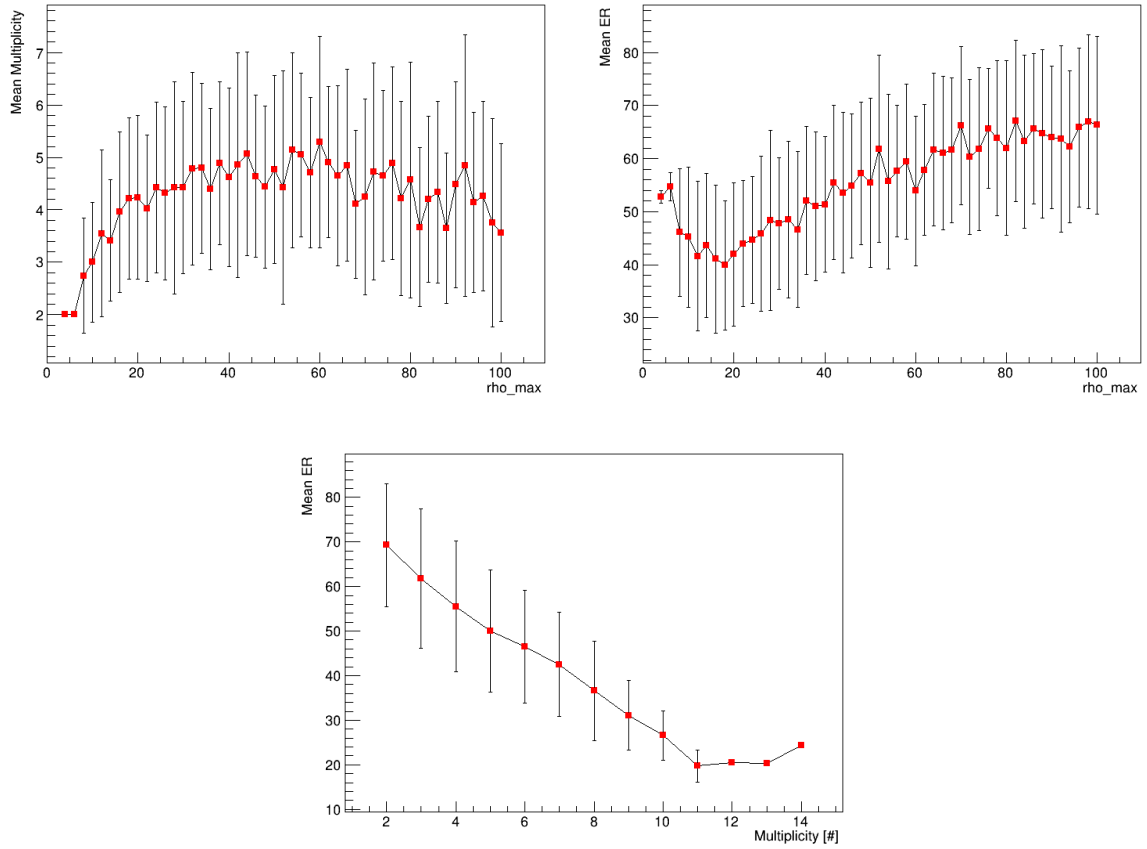


**Figure 4.24:** Mean M vs $\rho_{max}$ ( top left), Mean ER vs $\rho_{max}$ (bottom), Mean ER vs $\rho_{max}$ (top right). Multiplicity Analysis of CM09short waveform in O4 configuration cut_2

the maximum value of energy (i.e. the most energetic segment) and the value of multiplicity. The second graph shows the distribution mean ER among the maximum $\rho$. We see that there is no clear way in how the pipeline divides the injected signal. What barely emerges is a slight increase of the mean ER vs the max $\rho$, but with such errors it is not correct to assert a clear increase of the percentage. An increasing ER related to an increasing total energy may mean that the bigger the $\rho$ of the injected signal is, the better it will be regained. Finally in the last graph we see how the mean ER distributes among the multiplicities. In this case there is a clear correlation in multiplicity increasing and mean ER decreasing. Now we report the same graphs but for the O4 and O4-$\gamma$ configuration, see figures 4.24 and 4.25.

As we see the behaviour for the others configuration is quite similar.

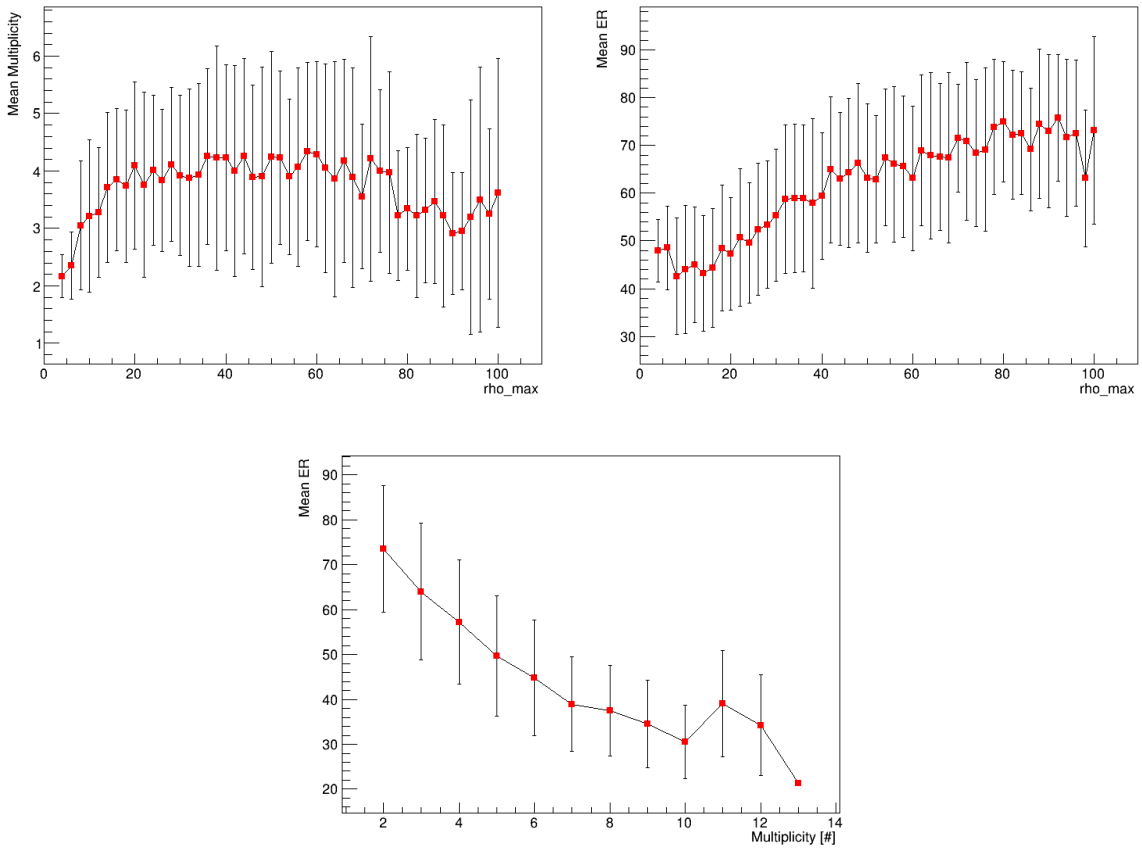


**Figure 4.25:** Mean M vs $\rho_{max}$ ( top left), Mean ER vs $\rho_{max}$ (bottom), Mean ER vs $\rho_{max}$ (top right). Multiplicity Analysis of CM09short waveform in O4 - $\gamma$ configuration cut_2

# 5

# Data analysis, Machine Learning training and test

In order to better distinguish the noise from the signals we can rely on a plenty of powerful tools: one is the Machine Learning (ML) techniques. Exploiting the capability of the ML algorithm to distinguish signals from noise, we can apply this tool to improve our detecting capability through cWB, by enhancing the discrimination between signal and noise. In recent years the use of deep learning and machine learning algorithm for astrophysics and Gravitational Wave physics have been deeply used [43], [44], [45]. In this work we will approach the XGBoost algorithm, namely eXtreme Gradient Boost: a decision tree based ensemble learning algorithm developed by [46] for the cWB searches .

## 5.1 XGBoost: a brief introduction

The ML technique is implemented through the algorithm XGBoost [46]: a decision tree based ensemble learning algorithm. In this context this tool will provide an automated method of the signal-noise classification of cWb triggers and optimize the pipeline sensitivity. The ML algorithm does not affect the trigger selection and reconstruction phase: in fact it is provided from the cWB reconstructed triggers the generic statistical data which will be used for the construction of the Machine Learning Model. In general, a Machine Learning produces a continuous ranking criteria for the reconstructed events, in XGBoost is generated an ensemble of decision trees. This method relies on the construction of subsequent learners (trees) starting from

| XGBoost hyperparameter | value |
|---|---|
| objective | binary:logistic |
| tree_method | hist |
| grow_policy | lossguide |
| n_estimators | 20,000 |
| max_depth | 7,9,11,13 |
| learning_rate | 0.1, 0.03 |
| min_child_weight | 5.0,10.0 |
| colsample_bytree | 0.6, 0.8, 1.0 |
| subsample | 0.4, 0.6, 0.8 |
| gamma | 2.0, 5.0, 10.0 |

**Table 5.1:** List of hyperparameters and some possible values

the base learners (base trees) [46]. In each tree construction continuous scores are evaluated by taking the weighted average of the output obtained from each decision tree in the ensemble. The final output $P_{XGB}$ is acquired by taking the sigmoid of the combined scores: in our context a resulting value $\sim 0$ means that the result is noise, instead $\sim 1$ means signal. The Machine learning model is constructed by selecting several summary statistic parameters estimated by cWB as input features for the Machine Learning algorithm. The parameters used in this work are:

- Correlation across the detectors and signal strength ($\eta_{l_0}$, $c_c$, $\eta_F$)
- Quality of likelihood fit ($\frac{E_c}{\mathcal{L}}$, $\chi^2$)

In this project we used a simplified version of the parameters' set, with respect to the one published in the [46], which includes also Time-Frequency evolution of the event and estimators for the number of cycles in the reconstructed waveform. For a complete description of them we refer to appendix A of [46].

The various properties of the learning process are controlled by the so-called hyperparameters. Those values are fundamental in order to prevent overfitting, also they need to be tuned for each application. In table 5.1 there is a list of these hyperparameters.

Basically what XGBoost provides us is a new ranking statistics attained by the learning process through the triggers provided by cWB. The ranking statistics $\rho_r$ obtained is

$$\rho_r = \sqrt{\frac{E_c}{1 + \chi^2 \max(1, \chi^2) - 1}} W_{XGB} \tag{5.1}$$

Where $E_c$ is the coherent Energy as defined in equation (3.25), while $\chi^2$ is the correction factor, close to one for genuine GW events, reduces for non-Gaussian noise contribution. Finally $W_{XGB}$ is the XGBoost penalty factor, which is obtained

| XGBoost hyperparameter | value |
|---|---|
| max_depth | 6 |
| learning_rate | 0.03 |
| min_child_weight | 5.0 |
| colsample_bytree | 1.0 |
| subsample | 0.6 |
| gamma | 2.0 |

**Table 5.2:** Hyperparameters used for XGBoost training

applying correction to the XGBoost output $P_{XGB}$ and then a monochromatic transformation such as $W_{XGB} = W_{XGB}(P_{XGN})$ [46].

## 5.2 XGBoost configuration for long duration GW signal search

The aim of this section is to train the XGBoost algorithm with several Gravitational Waveforms with different morphology and to evaluate the detection efficiency of cWB once the ML algorithm has been applied to the data. We will consider the strain foreseen for O4 within the LHV configuration. Firstly we have performed a tuning of the XGBoost algorithm. We have considered as values of the hyperparameters those in table 5.2, which are the same as the one used for the Short analysis [46].

Once those parameters have been set, the first step is to train the algorithm for the waveforms considered. In order to do so we have split the data needed for the analysis. For this work we have decided to divide the data in 50% for training and 50% for testing. Both the data of the background and of the waveform have been split. For the training we have used two kinds of cuts: cut_2 and cut_4. The vetoes and conditions are the same as the one used in the previous chapter. The cut_2 is the same as the one defined previously, while the cut_4 is:

cut_4

- frequency cuts: $>$ 40Hz and $<$ 2048Hz
- netCC cuts: $>$ 0.6
- duration: $>$ 0.5s

This has been done in order to have a wider idea of how well XGboost is capable of distinguishing the noise from the signals and to understand how the length cut is affecting its proficiency. The length cuts implemented in cut_2 and cut_4

| Taining values | | | |
|---|---|---|---|
| values | no_cut | bin2_cut | bin4_cut |
| Best score | 0.396113 | 0.83655 | 0.643468 |
| Number of leaves in the best tree | 24 | 9 | 10 |
| Total number of leaves in the trained model | 1613 | 9283 | 2095 |

**Table 5.3:** Training values obtained for XGBoost with 3 waves test phase with bin2_cut and bin4_cut

will allow us to see also shorter signals. Moreover this will increase the parameters' space of the reconstructed signals. Releasing the minimum threshold required for the reconstructed triggers, as expected, it increases also the rate of expected background triggers; then we can test if XGBboost is still capable in distinguish the signals from the noise considering Long Duration signals. To see if the training of the algorithm has been performed correctly we can consider the ROC curve and the number of leaves of the tree that have been produced in the training phase.

## 5.3 XGBoost - Efficiency

The aim of this section is to test the XGBoost capability in recognizing injected signals. Starting from a test phase where we inject three waveforms and we evaluate the detecting efficiency, then we train the algorithm with six different waveforms and we evaluate the detection efficiency at $h_{rss}(50\%)$ for those signals. Moreover we evaluate the detection efficiency for two signal morphologies, not used in the training test. This check allows us to prove that the algorithm fully preserves its agnostic approach with respect to the signal morphology. We start from the test phase. Firstly we report the background, as said above, we split the data: one half for training and the other half for testing. For the preliminary test phase we have chosen three waveforms, AdiA, CM09short and NCSACAM_F. So we train the algorithm with the background and these waveforms. In table 5.3 we report the output values of the training for all the training models

For completeness we report in Figure 5.1 the ROC obtained by training XGBoost with the three waveforms.

Once the training has been performed, we apply the model to the remaining fraction of background in order to characterize the background statistic and obtain the ifar. Since the fraction of data used for the XGBoost training is the 50%, this means that the test is performed over the remaining 50% of data, which results in 52.8y of background analysis. This is because we considered the data from the previous section analysis. The background characterization is reported in graphs 5.2 and 5.3.

Once the training phase and background analysis have been performed we can proceed in evaluating the detection efficiency. What we do now is to apply the model obtained by XGBoost in the training phase to the remaining fraction of trig-

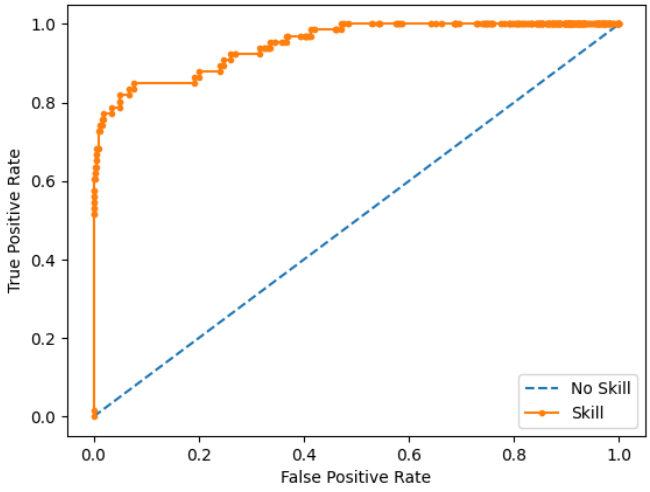


**Figure 5.1:** Example ROC curve obtained for 3 waves test phase with bin4_cut model.

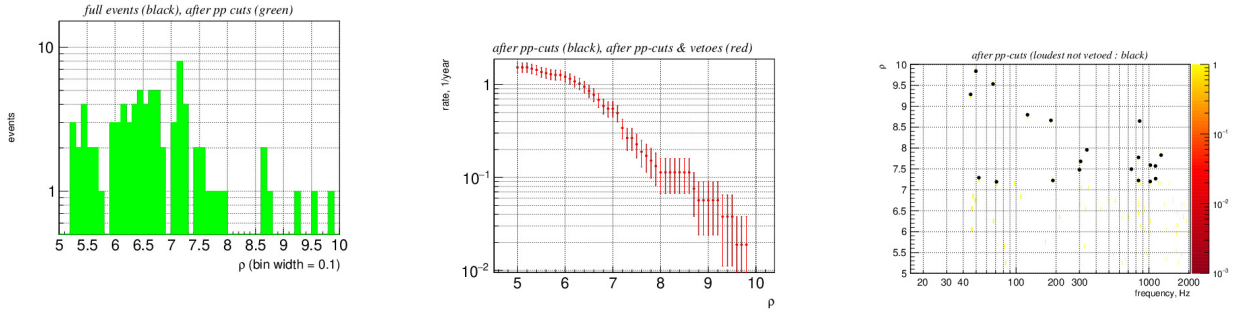


**Figure 5.2:** LHV network with O4 strain sensitivity and cut_2. Number of Events with respect to ρ (left), event rate distribution as function of ρ (center), ρ vs frequency (right)

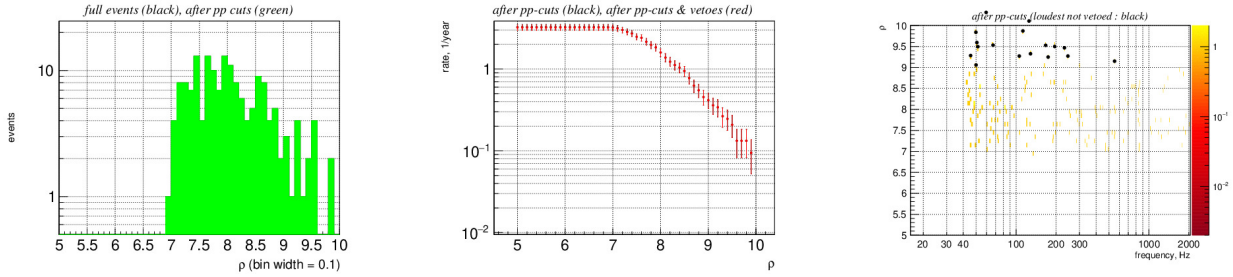


**Figure 5.3:** LHV network with O4 strain sensitivity and cut_4. Number of Events with respect to ρ (left), event rate distribution as function of ρ (center), ρ vs frequency (right)

| Efficiencies | | |
|---|---|---|
| Waveform | bin2_cut | bin4_cut |
| AdiA | $1.77\text{x}10^{-22}$ | $1.88\text{x}10^{-22}$ |
| CM09short | $3.88\text{x}10^{-22}$ | $3.96\text{x}10^{-22}$ |
| NCSACAM_F | $7.31\text{x}10-22$ | $3.47\text{x}10^{-22}$ |

**Table 5.4:** $h_{rss}(50\%)$ detection efficiency obtained for 3 waves test phase with cut_2 and cut_4 in O4 configuration, LHV

gers for each waveform, then we apply the ifar selection from the background. In table 5.4 we report the $h_{rss}(50\%)$ detection efficiency of XGBoost in reconstructing the waveforms by the model associated with the cut_2 and the cut_4.

The AdiA and CM09short waveform efficiencies are consistent between cut_2 and cut_4. Training the algorithm with triggers of those waveforms including a wider span of lengths does not change the efficiency. As we see, the most interesting case is the NCSACAM_F waveform. Here the cut_4, which allows the algorithm to access a much wider number of triggers due to the difference in length, provides an increased efficiency, as expected. In fact we are considering a wider parameters' space: by studying the population of lengths for this waveform, we see that (figure 5.4) applying the cut_4 instead of the cut_2 will save hundreds of triggers, causing a better training of the algorithm and consequently a better efficiency.

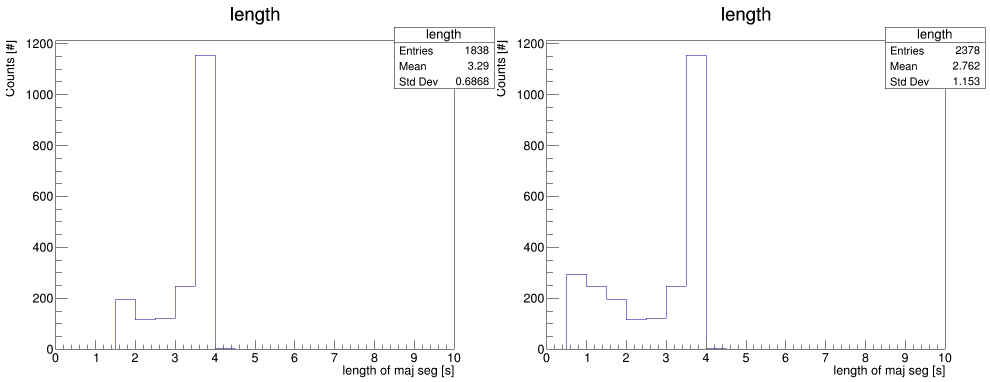


**Figure 5.4:** Lengths distribution for NCSACAM_F with different cuts. Length distribution for cut_2 (left), Length distribution for cut_4 (right)

At this point we can move to the XGBoost efficiency test for unknown waveforms. As always, we report the background analysis. The total observation time analyzed is the same as for the three waves test. The background statistic is for cut_2 and cut_4, Figure 5.5 and 5.6.

Finally we apply the XGBoost algorithm considering six different waveforms for the training, then we apply the model obtained to two waveforms which did not were used for the training. These are AdiB, and the msmagnetar [47], which is not included in the morphologies considered for the training. The fraction of triggers considered for the test of these two

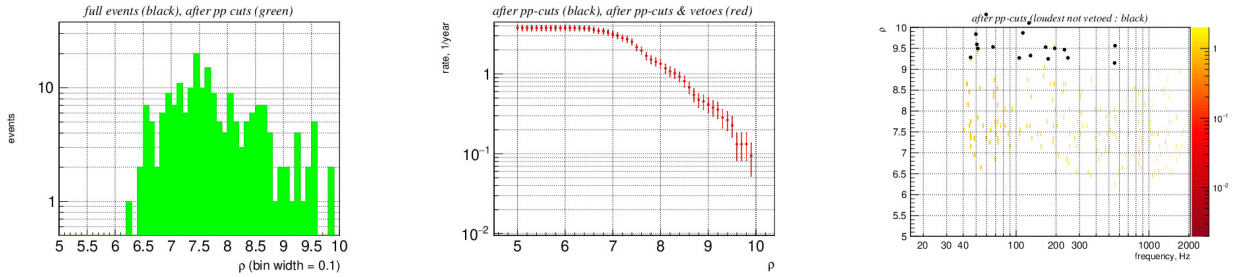


**Figure 5.5:** LHV network with O4 strain sensitivity, cut_2 applied. Number of Events with respect to ρ (left), event rate distribution as function of ρ (center), ρ vs frequency (right)

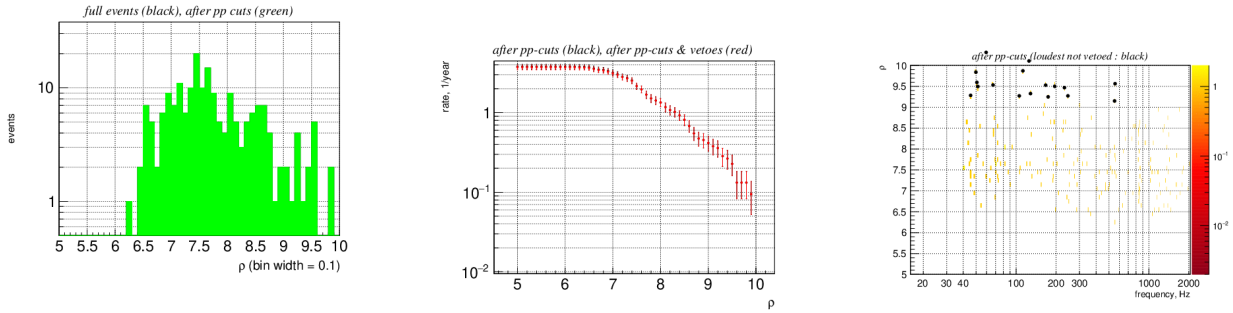


**Figure 5.6:** LHV network with O4 strain sensitivity and cut_4. Number of Events with respect to ρ (left), event rate distribution as function of ρ (center), ρ vs frequency (right)

waveforms is 90%. For the training we have considered AdiA, CM09short, NCSACAM_F, NCSACAM_B, ISCOchirpA and magXnetarD. The fraction of triggers considered for training with these waveforms is 50%.

For safety check in table 5.5 we report both the efficiencies of the training waveforms and the untrained ones. As we see from the table the detection efficiencies obtained are consistent with the one achieved for the test phase with three waveforms. Also if we consider the efficiencies gained from the previous chapter the results are consistent. In particular what is noticeable is that AdiB efficiency is consistent with the result obtained for the standard analysis. This outcome shows us that the algorithm is capable in recognizing the injection even if it is not trained for this specific waveform.

| Taining values | | |
|---|---|---|
| values | bin2_cut | bin4_cut |
| Best score | 0.871295 | 0.687881 |
| Number of leaves in the best tree | 9 | 9 |
| Total number of leaves in the trained model | 9421 | 4826 |

**Table 5.5:** Training values of XGboost obtained for 6 waves test phase with cut_2 and cut_4

| Efficiencies | | |
|---|---|---|
| Waveform | bin2_cut | bin4_cut |
| AdiA | $1.78\text{x}10^{-22}$ | $1.88\text{x}10^{-22}$ |
| CM09short | $3.89\text{x}10^{-22}$ | $3.96\text{x}10^{-22}$ |
| NCSACAM_F | $7.31\text{x}10^{-22}$ | $3.47\text{x}10^{-22}$ |
| NCSACAM_B | $4.66\text{x}10^{-22}$ | $3.96\text{x}10^{-22}$ |
| ISCOchirpA | $9.71\text{x}10^{-22}$ | $4.82\text{x}10^{-22}$ |
| magXnetarD | $2.08\text{x}10^{-21}$ | $2.27\text{x}10^{-21}$ |
| AdiB | $1.52\text{x}10^{-22}$ | $1.54\text{x}10^{-22}$ |
| msmagnetar | $8.46\text{x}10^{-22}$ | $8.74\text{x}10^{-22}$ |

**Table 5.6:** $h_{rss}(50\%)$ detection efficiency values obtained for the whole set of waves, training with 6 waves and test with 2 waves. Used both cut_2 and cut_4 in O4 configuration

# 6

# Conclusions

In this work we tested possible cWB algorithm configurations for next data taking of LHV, O4 is foreseen to start by the beginning of the next year, through a reanalysis and simulations campaign of public data of last data taking O3b, occurred from November 2019 to March 2020. In particular we focused on the detection efficiency obtainable from the LHV configuration considering the O3b data and simulating data with sensitivity similar to the one expected for the next O4 data acquisition. The simulation campaign with sensitivity expected for the O4 has been performed using different configurations of the analysis, to test the capability of the pipeline in reconstructing the position of the injected signals and how it affects the efficiency. The results show a better efficiency as expected: the detection efficiency is increased due to the improving of expected sensitivity for the O4 simulated strain with respect to the O3b data taking. Instead there is a loss of efficiency if we consider relaxing the $\gamma$ constraint, and the gain we obtain in reconstructing the position does not justify this kind of choice. A work on the algorithm taking care of this feature must be performed in order to guarantee an acceptable reconstructed position and detection efficiency. Then we carried out an analysis of how our pipeline reconstructs the injected signals breaking them in several different segments. This is particularly important since our study showed how the length and the morphology of injection is affecting the reconstruction capability of the pipeline. We observed that signals lasting more than tens of seconds are usually reconstructed in different segmented triggers. This means that in order to achieve a correct analysis of them we need to study a method in the post-production phase for reconstruction. Also, this attitude of the pipeline urges to be deeply studied and analysed, since it severely affects the capability of the algorithm in recognizing correctly the injected signal as just

one signal, instead as a plenty of segments. Then we studied how the Machine Learning techniques applied to this specific problem could help us in recognizing gravitational waves from noise through cWB. In particular the study of two unknown waveforms performed by XGBoost is encouraging, since the detection efficiency provided by cWB after the training of the ML algorithm is consistent to the one obtained by the standard cWB efficiency analysis. In particular, getting a wider space of parameters for XGBoost increased noticeably the capability of the algorithm in recognizing the signal from noise. Also, the introduction of parameters in the ML learning process, such as the multiplicity as defined previously, could be effective in improving the performance of the algorithm. In order to do so, a study of the background with the respect of the multiplicity parameter should be taken. In particular a characterization of the glitches distribution in time must be performed considering various cases. For instance: the segmentation of one glitch event with a wide time duration as the example of Figure 4.2, or the case of two different glitches close in time considered as a unique event.

# References


[1] A. Królak and M. Patil, "The first detection of gravitational waves," *Universe*, vol. 3, no. 3, 2017. [Online]. Available: https://www.mdpi.com/2218-1997/3/3/59

[2] M. Maggiore, *Gravitational Waves: Volume 1:Theory and experiments*. OUP Oxford, 2007.

[3] M.N., Kahn and K., Zakaullah, *Adventures in Experimental Physicsn*, 2005.

[4] D. R. Paschotta. Optical resonators. [Online]. Available: https://www.rp-photonics.com/optical_resonators.html

[5] I. Nardecchia, "Detecting gravitational waves with advanced virgo," *Galaxies*, vol. 10, no. 1, 2022. [Online]. Available: https://www.mdpi.com/2075-4434/10/1/28

[6] Acernese, F. and Adams, T. et al., "Status of advanced virgo," *EPJ Web Conf.*, vol. 182, p. 02003, 2018. [Online]. Available: https://doi.org/10.1051/epjconf/201818202003

[7] The LIGO Scientific Collaboration and The Virgo Collaboration and The KAGRA Collaboration et al., "Gwtc-3: Compact binary coalescences observed by ligo and virgo during the second part of the third observing run," 2021. [Online]. Available: https://arxiv.org/abs/2111.03606

[8] V. Collaboration. Virgo status. [Online]. Available: https://www.virgo-gw.eu/status.html

[9] Ligo scientific community. How to use. [Online]. Available: https://gwburst.gitlab.io/documentation/latest/html//running.html#user-parameters-c

[10] S. Vinciguerra, "Gravitational wave searches for transient signals: classication of candidates consistent with binary black hole mergers," Ph.D. dissertation, 2013.

[11] Simone Dall'Osso and Bruno Giacomazzo and Rosalba Perna and Luigi Stella, "GRAVITATIONAL WAVES FROM MASSIVE MAGNETARS FORMED IN BINARY NEUTRON STAR MERGERS," *The Astrophysical Journal*, vol. 798, no. 1, p. 25, dec 2014. [Online]. Available: https://doi.org/10.1088/0004-637x/798/1/25

[12] M. Toscani, G. Lodato et al, "Gravitational wave emission from unstable accretion discs in tidal disruption events," *Monthly Notices of the Royal Astronomical Society*, 2019.

[13] A. Corsi and P. Mészáros, "GAMMA-RAY BURST AFTERGLOW PLATEAUS AND GRAVITATIONAL WAVES: MULTI-MESSENGER SIGNATURE OF a MILLISECOND MAGNETAR?" *The Astrophysical Journal*, vol. 702, no. 2, pp. 1171–1178, aug 2009. [Online]. Available: https://doi.org/10.1088/0004-637x/702/2/1171

[14] E. A. Huerta, C. J. Moore, P. Kumar, D. George, A. J. K. Chua, R. Haas, E. Wessel, D. Johnson, D. Glennon, A. Rebei, A. M. Holgado, J. R. Gair, and H. P. Pfeiffer, "Eccentric, nonspinning, inspiral, gaussian-process merger approximant for the detection and characterization of eccentric binary black hole mergers," *Phys. Rev. D*, vol. 97, p. 024031, Jan 2018. [Online]. Available: https://link.aps.org/doi/10.1103/PhysRevD.97.024031

[15] M. H. P. M. van Putten, "DIRECTED SEARCHES FOR BROADBAND EXTENDED GRAVITATIONAL WAVE EMISSION IN NEARBY ENERGETIC CORE-COLLAPSE SUPERNOVAE," *The Astrophysical Journal*, vol. 819, no. 2, p. 169, mar 2016. [Online]. Available: https://doi.org/10.3847%2F0004-637x%2F819%2F2%2F169

[16] R. Abbott, T.D. Abbott et al., "All-sky search for long-duration gravitational-wave bursts in the third advanced LIGO and advanced virgo run," *Physical Review D*, vol. 104, no. 10, nov 2021. [Online]. Available: https://doi.org/10.1103%2Fphysrevd.104.102001

[17] S. M. Carroll, *Spacetime and Geometry: An Introduction to General Relativity*. Addison-Wesley, 1st edition, 2003.

[18] B.P. Abbott and R. Abbott et al., "All-sky search for short gravitational-wave bursts in the first advanced ligo run," *Phys. Rev. D*, vol. 95, p. 042003, Feb 2017. [Online]. Available: https://link.aps.org/doi/10.1103/PhysRevD.95.042003

[19] B.P., Abbott and R., Abbott et al., "Observation of gravitational waves from a binary black hole merger," *Phys. Rev. Lett.*, vol. 116, p. 061102, Feb 2016. [Online]. Available: https://link.aps.org/doi/10.1103/PhysRevLett.116.061102

[20] R.Abbott and T.D.Abbott et al, "Open data from the first and second observing runs of advanced ligo and advanced virgo," *SoftwareX*, vol. 13, p. 100658, 2021. [Online]. Available: https://www.sciencedirect.com/science/article/pii/S2352711021000030

[21] B.P. Abbott and R. Abbott et al., "Gw170817: Observation of gravitational waves from a binary neutron star inspiral," *Phys. Rev. Lett.*, vol. 119, p. 161101, Oct 2017. [Online]. Available: https://link.aps.org/doi/10.1103/PhysRevLett.119.161101

[22] R. Abbott, and T.D. Abbott et al., "Gw190412: Observation of a binary-black-hole coalescence with asymmetric masses," *Phys. Rev. D*, vol. 102, p. 043015, Aug 2020. [Online]. Available: https://link.aps.org/doi/10.1103/PhysRevD.102.043015

[23] B. P. Abbott and R. Abbott et al., "GW190425: Observation of a compact binary coalescence with total mass $\sim$ 3.4 msub$\odot$/sub," *The Astrophysical Journal Letters*, vol. 892, no. 1, p. L3, mar 2020. [Online]. Available: https://doi.org/10.3847/2041-8213/ab75f5

[24] R. Abbott, R. and T.D. Abbott et al., "Gw190521: A binary black hole merger with a total mass of 150 $M_{\odot}$," *Phys. Rev. Lett.*, vol. 125, p. 101102, Sep 2020. [Online]. Available: https://link.aps.org/doi/10.1103/PhysRevLett.125.101102

[25] F. Salemi, E. Milotti et al., "Wider look at the gravitational-wave transients from GWTC-1 using an unmodeled reconstruction method," *Physical Review D*, vol. 100, no. 4, aug 2019. [Online]. Available: https://doi.org/10.1103%2Fphysrevd.100.042003

[26] S. Klimenko, S. Mohanty et al, "Constraint likelihood analysis for a network of gravitational wave detectors," *Physical Review D*, vol. 72, no. 12, dec 2005. [Online]. Available: https://doi.org/10.1103%2Fphysrevd.72.122002

[27] S. Klimenko, I. Yakushin et al, "A coherent method for detection of gravitational wave bursts," *Classical and Quantum Gravity*, vol. 25, no. 11, p. 114029, may 2008. [Online]. Available: https://doi.org/10.1088/0264-9381/25/11/114029

[28] S. Klimenko, G. Vedovato et al, "Localization of gravitational wave sources with networks of advanced detectors," *Physical Review D*, vol. 83, no. 10, may 2011. [Online]. Available: https://doi.org/10.1103%2Fphysrevd.83.102001

[29] S. Klimenko, G. Vedovato et al., "Method for detection and reconstruction of gravitational wave transients with networks of advanced detectors," *Phys. Rev. D*, vol. 93, p. 042004, Feb 2016. [Online]. Available: https://link.aps.org/doi/10.1103/PhysRevD.93.042004

[30] V. Necula, S. Klimenko et al, "Transient analysis with fast wilson-daubechies time-frequency transform," *Journal of Physics: Conference Series*, vol. 363, p. 012032, jun 2012. [Online]. Available: https://doi.org/10.1088/1742-6596/363/1/012032

[31] V. Tiwari, M. Drago et al, "Regression of environmental noise in LIGO data," *Classical and Quantum Gravity*, vol. 32, no. 16, p. 165014, jul 2015. [Online]. Available: https://doi.org/10.1088%2F0264-9381%2F32%2F16%2F165014

[32] S. Klimenko and I. Yakushin et al, "A coherent method for detection of gravitational wave bursts," *Classical and Quantum Gravity*, vol. 25, no. 11, p. 114029, may 2008. [Online]. Available: https://doi.org/10.1088/0264-9381/25/11/114029

[33] Caudill, S. and Shivaraj, K. et al., "Gravitational-wave searches in the era of advanced ligo and virgo," *Modern Physics Letters A*, vol. 36, p. 5, 2021.

[34] L. Santamaria, C.D. Ott et al. (February 14, 2011) Gravitational wave emission from accretion disk instabilities – analytic models. [Online]. Available: https://dcc.ligo.org/LIGO-T1100093-v2/public

[35] T. Dietrich, T. Hinderer et al, "Interpreting binary neutron star mergers: describing the binary neutron star dynamics, modelling gravitational waveforms, and analyzing detections," *General Relativity and Gravitation*, vol. 53, no. 3, mar 2021. [Online]. Available: https://doi.org/10.1007%2Fs10714-020-02751-6

[36] D. LAI and S. L. SHAPIRO, "Gravitational radiation from rapidly rotating nascent neutron stars," *Astrophysical Journal*, 1995.

[37] S. Mineshige, "Accretion disk instabilities," *Astrophysics and Space Science*, 1993.

[38] Ligo scientific community. Mdc engine. [Online]. Available: https://gwburst.gitlab.io/documentation/latest/html//mdc.html?highlight=injection#mdc-overview

[39] L.-V. scientific community. Gwosc. [Online]. Available: https://www.gw-openscience.org/

[40] Ligo-Virgo Scientific Community, "Virgo detector characterization and data quality during the 03 run," 2022. [Online]. Available: https://arxiv.org/abs/2205.01555

[41] B. P. Abbott and R. Abbott et al., "A guide to LIGO–virgo detector noise and extraction of transient gravitational-wave signals," *Classical and Quantum Gravity*, vol. 37, no. 5, p. 055002, feb 2020. [Online]. Available: https://doi.org/10.1088/1361-6382/ab685e

[42] B. P. Abbott, and R. Abbott et al., "Prospects for observing and localizing gravitational-wave transients with advanced ligo, advanced virgo and kagra," *Living Rev Relativ*, vol. 23, no. 3, Sep 2020.

[43] E. Cuoco, J. Powell et al, "Enhancing gravitational-wave science with machine learning," *Machine Learning: Science and Technology*, vol. 2, no. 1, p. 011002, dec 2020. [Online]. Available: https://doi.org/10.1088/2632-2153/abb93a

[44] D. George, E.A. Huerta, "Deep learning for real-time gravitational wave detection and parameter estimation: Results with advanced ligo data," *Physics Letters B*, vol. 778, pp. 64–70, 2018. [Online]. Available: https://www.sciencedirect.com/science/article/pii/S0370269317310390

[45] A. Iess, E. Cuoco et al, "Core-collapse supernova gravitational-wave search and deep learning classification," *Machine Learning: Science and Technology*, vol. 1, no. 2, p. 025014, jun 2020. [Online]. Available: https://doi.org/10.1088/2632-2153/ab7d31

[46] T. Mishra, B. O'Brien et al, "Optimization of model independent gravitational wave search for binary black hole mergers using machine learning," *Physical Review D*, vol. 104, no. 2, jul 2021. [Online]. Available: https://doi.org/10.1103%2Fphysrevd.104.023014

[47] A. Mytidis, M. Coughlin, and B. Whiting, "CONSTRAINING THE r-MODE SATURATION AMPLITUDE FROM a HYPOTHETICAL DETECTION OF r-MODE GRAVITATIONAL WAVES FROM a NEWBORN NEUTRON STAR: SENSITIVITY STUDY," *The Astrophysical Journal*, vol. 810, no. 1, p. 27, aug 2015. [Online]. Available: https://doi.org/10.1088%2F0004-637x%2F810%2F1%2F27

# Acknowledgments

A G.